Alma Mater Studiorum - Università di Bologna

School of Science
Department of Physics and Astronomy
Master Degree Programme in Astrophysics and Cosmology

The Effects of Rotation-Induced Mixing on the Properties of Secondary-Clump Stars

Graduation Thesis

Presented by:
Lorenzo Martinelli

Supervisor:
Chiar.mo Prof. Andrea Miglio
Co-supervisors:
Dr. Patrick Eggenberger
Dr. Gaël Buldgen

Academic year 2022-2023
Graduation date 27/10/2023

Abstract

Uncertainties on the nature and efficiency of internal mixing processes in stars are becoming the dominant limitation to inferring accurate stellar ages. One particularly relevant uncertainty is that of the efficiency of additional mixing at the boundary of convective cores in the core hydrogen-burning phase. This project investigates a novel method of constraining such mixing processes, in particular those induced by rotation, by studying their imprint on the observed luminosity distribution and core-properties of low- to intermediate-mass core helium burning stars. Through the computation of single-age synthetic stellar populations using models that incorporate rotation-induced mixing, we have uncovered the appearance of extended red clumps within single-age clusters. The properties of these red clumps possess the potential to provide valuable insights into the efficiency of rotation-induced mixing processes, the origins of the observed extended red clumps and turn-offs, and to enhance the accuracy of age determinations. An initial assessment comparing the results with observations appears to support the plausibility of this scenario to some extent.

Contents

Chapter 1

Introduction

A comprehensive understanding of how stars evolve and interact with their surrounding medium is vital for various fields in astrophysics. Accurate estimation of stellar parameters such as ages, masses, radii, and metallicities within stellar populations is essential for research in areas like galactic structure and formation history, stellar system dynamics and kinematics, and the characterization of parent stars in planetary systems, among others. Achieving this understanding hinges on having reliable evolutionary models for the constituent stars of these populations. In stars with convective cores, the extent and efficiency of near-core mixing processes play a critical role in determining the core mass and the main-sequence lifetime. However, these mixing processes remain poorly understood, leading to significant uncertainties in stellar structure and evolution models. Our focus in this study is on stars with masses ranging from 1.7 to 3 solar masses. These stars bridge the gap between Low-Mass Stars (LMS) and Intermediate-Mass Stars (IMS) and, when in the core He burning phase, they are commonly referred to as secondary clump stars (2RCS), as we will elaborate on shortly. The properties of this transition phase are influenced by various factors, with the efficiency of internal mixing processes being a key consideration. Rotation in stars can induce large-scale displacements, such as meridional circulation, and lead to instabilities like shear instability, all of which can affect the transport of chemical elements within the star. However, the extent to which rotation-induced mixing influences these processes remains uncertain.

This work aims to address this issue by investigating the impact of rotation-induced mixing on secondary clump stars, both as individual stars and within single-age stellar populations. Utilizing models of rotating stars, and combining them in single-age synthetic stellar populations we aim to make predictions that can be compared with observations. This will help to constrain the efficiency of these mixing processes, refine our understanding of stellar rotation, and ultimately improve the accuracy of age, mass, radius, and metallicity determinations for stars.

We will begin by establishing the fundamental principles of stellar modeling, while for

comprehensive insights into the observational aspects of stars, we refer readers to other sources like Böhm-Vitense 1989.

In Chapter 2, we provide a brief overview of the core concepts in standard stellar evolution. This serves as a foundational context for the subsequent chapters.

Chapter 3 delves into a comprehensive exploration of the fundamental concepts of rotation in stars and the various approaches employed in modeling this phenomenon.

Chapter 4 takes an in-depth look at the properties of a limited grid of rotating models derived from the Geneva stellar evolution code. These models serve as a reference for the higher-resolution grid of MESA models introduced in Chapter 5. These MESA models incorporate rotation-induced mixing of chemicals and are calibrated based on the reference models to investigate secondary clump stars within synthetic stellar populations.

Within Chapter 5, we conduct a preliminary comparison with observations of field stars and stars within stellar clusters, emphasizing that this comparison is not meant to be exhaustive but rather serves as an initial assessment.

Chapter 2

Stellar Evolution of Low- and Intermediate-Mass Stars

The determination of stellar classical parameters (such as age, mass and radius) is possible through the comparison of observational constraints such as luminosity, effective temperature, surface abundances and oscillation properties with predictions from stellar models. These models depend on micro and macro-physics inputs ingredients and can be constrained thanks to spectroscopic, astrometric, photometric, interferometric, and asteroseismic observations. Given the primary focus of this study on how rotation influences stellar structure and evolution, a significant portion of our work is dedicated to elucidating these effects. Therefore, we assume a basic understanding of non-rotating stellar evolution and will provide a concise overview of key concepts as a foundation for our subsequent discussions. For more comprehensive explanations, we recommend referring to other sources, such as Salaris and Cassisi 2006.

2.1   Fundamental Equations of Stellar Structure Without Rotation

Stellar hydrostatic[1] models are based on four fundamental equations that express the complete set of equilibrium conditions which must be fulfilled throughout the stellar structure. These conditions can be presented in both Eulerian coordinates, with independent vari-

---

[1]Assuming that models are in hydrostatic equilibrium is justified when when evolution is slow with respect to the dynamical timescale.

ables (r, t), and Lagrangian coordinates[2], with independent variables[3] (M_r, t):

1. **Equation of hydrostatic equilibrium**:

$$\frac{dP}{dr} = -\frac{GM_r}{r^2}\rho \quad \text{or} \quad \frac{dP}{dM_r} = -\frac{GM_r}{4\pi r^4}. \tag{2.1}$$

2. **Mass continuity equation**:

$$\frac{dM_r}{dr} = 4\pi r^2 \rho \quad \text{or} \quad \frac{dr}{dM_r} = \frac{1}{4\pi r^2 \rho}. \tag{2.2}$$

3. **Equation of energy transport**:

- *Radiative transport*:

$$\frac{dT}{dr} = -\frac{3\kappa\rho}{4acT^3}\frac{L_r}{4\pi r^2} \quad \text{or} \quad \frac{dT}{dM_r} = -\frac{GM_r T}{4\pi r^4 P}\nabla_{rad}. \tag{2.3}$$

- *Convective transport (valid only where convection is an efficient transport mechanism)*:

$$\frac{dT}{dr} = \frac{\Gamma_2 - 1}{\Gamma_2}\frac{T}{P}\frac{dP}{dr} \quad \text{or} \quad \frac{dT}{dM_r} = -\frac{GM_r T}{4\pi r^4 P}\nabla_{ad}. \tag{2.4}$$

In the interiors, convection is present if $\nabla_{rad} > \nabla_{ad}$, otherwise the transport is radiative.

4. **Equation of energy conservation**:

$$\frac{dL_r}{dr} = 4\pi r^2 \rho(\epsilon_{nuc} + \epsilon_{grav} - \epsilon_\nu) \quad \text{or} \quad \frac{dL_r}{dM_r} = (\epsilon_{nuc} + \epsilon_{grav} - \epsilon_\nu), \tag{2.5}$$

where P is the pressure, ρ is the density, T is the temperature, L_r is the luminosity at radial coordinate r, Γ_2 is an adiabatic coefficient[4], ϵ_{nuc}, ϵ_{grav}, ϵ_ν terms are the energy generation rates respectively from nuclear reactions, gravitational contraction/expansion,

---

[2]The obvious coordinate to use in a Eulerian coordinate system is the radius of a spherical shell, $r \in [0, R]$. However, in stellar evolution, the coordinate r is not always convenient as an independent variable. Except for particular cases of heavy mass loss, the stellar mass remains almost constant, while the stellar radius may rapidly change. It is thus more appropriate (and simpler) to choose the mass M_r or the mass fraction (M_r/M_{tot}) as an independent variable.

[3]Here we write the variable $M = M(r)$ as M_r to explicitly show that they are interchangeable as independent variables, $r = r(M)$.

[4]Adiabatic coefficients describe the response of the system to an adiabatic change, they essentially describe the relations between the various differentials along an adiabat. Γ_2 is defined by $\frac{\Gamma_2 - 1}{\Gamma_2} = (\frac{\partial \ln T}{\partial \ln P})_{ad} = \nabla_{ad}$

neutrino production. G, a, and c are three physical constants (gravitational constant, radiation constant, and light speed) and:

$$\nabla_{ad} = (\frac{\partial \ln T}{\partial \ln P})_{ad} = \frac{\Gamma_2 - 1}{\Gamma_2} \quad \text{and} \quad \nabla_{rad} = \frac{3}{16\pi a c T^4} \frac{\kappa L_r P}{M_r T^4}. \tag{2.6}$$

The radiative gradient ∇_{rad} is defined as the thermal gradient which would be necessary to carry the sum of the radiative and convective fluxes by radiation only. We refer to Salaris and Cassisi 2006 for an extensive explanation of how these equations are obtained. In order to solve these equations, the following physical aspects are essential:

- Nuclear reaction rates to evaluate ϵ_{nuc} and ϵ_ν.

- The equation of state to determine ρ given T, P, and chemical composition.

- Opacities (κ) for calculating ∇_{rad}.

- A convection treatment for computing the convective flux and the temperature gradient where convection is ineffient.

- The rate of change of chemical species due to nuclear reactions. When atomic diffusion and radiative levitation are integrated into the stellar model, equations describing the change in chemical composition due to diffusion are necessary. So if X_i is the abundance in mass of the element labeled with i, for each element we have an equation:

$$\frac{dX_i}{dt} = (\frac{dX_i}{dt})_{nuc} + (\frac{dX_i}{dt})_{diff}. \tag{2.7}$$

In other words, the differential equations (2.1)-(2.2)-(2.3)/(2.4)-(2.5) are formulated in terms of the dependent variables (M_r, P, L_r, T, X_i). Hence we must be able to express the right-hand sides of the equations in terms of these variables. To do so requires expressions for ρ, ϵ_{grav}, ϵ_ν, Γ_2, κ, ϵ, $(dX_i/dt)_{nuc}$ and $(dX_i/dt)_{diff}$, as functions of P, T and chemical composition. These expressions are obtained from thermodynamics, atomic physics and nuclear physics. The differential equations (2.1)-(2.2)-(2.3)-(2.4)-(2.5) must be supplemented by suitable boundary conditions. We have four conditions with three free parameters R, L and M. Let us suppose that we integrate the four equations starting from the surface. When the center is reached, i.e., at $r = 0$, one should normally also have $L_r = 0$ and $M_r = 0$. This is not automatically the case for an arbitrary choice of R, L and M at the surface. This means that for a given M the other two surface parameters have to be adjusted until the integration leads simultaneously to $r = 0$, $L_r = 0$ and $M_r = 0$ when the center is reached. The two additional conditions at the center reduce the number of free parameters at the surface from three to one. Usually, one chooses the stellar mass M. Finally we need an initial model. This can be obtained from more or less

detailed studies of the early phases of stellar evolution, starting from the contraction of the original interstellar cloud. A simple alternative is to neglect the early history of the star, and assume that it is initially chemically homogeneous, and in thermal equilibrium, so that ϵ_{grav} can be neglected. Fortunately it turns out that the later evolution of the star is quite insensitive to the assumed initial conditions.

As the equations of stellar evolution have in general no analytical solutions, one solves them numerically, especially given that opacities and nuclear reaction rates are given as data tables. Many properties found by the numerical models can be derived analytically in a simplified and approximate way. Often, the analytical developments were made after the numerical models. The knowledge of the analytical relations is enlightening for the physical understanding of the astrophysical processes.

2.2 Evolutionary Phases

During its evolution, a star goes through several stages where its internal structure transforms. These changes can be tracked using the *Hertzsprung-Russell diagram* (HRD), see Fig.2.1, which showcases variations in surface luminosity (L) and effective temperature (T_{eff}) over time. Most of the evolutionary phases originally take their names from the features in the *color-magnitude diagrams* (CMDs) of star clusters that they populate, however they terminology is extended to the corresponding features in the *evolutionary tracks* of single stars. In the forthcoming paragraphs, we will offer a brief overview of the sequential evolutionary phases experienced by stars within the mass range of 1.7 M$_\odot$ to 3 M$_\odot$. This overview serves to introduce terminology and contextualize the subsequent content. For a more comprehensive and detailed exploration of all evolutionary stages, interested readers are directed to Salaris and Cassisi 2006.

2.2.1 Main Sequence

After the initial contraction phase of the original interstellar cloud, which, as previously indicated, has minimal impact on the subsequent stellar evolution, stars spend the majority of their lifespan on the *Main Sequence* (MS, Fig. 2.1) phase. During this MS phase, hydrogen burning serves as the primary source of nuclear energy, crucial for sustaining the star's stability. In stars where the *CNO cycle* takes precedence as the primary hydrogen-burning process, the core typically transitions to a convective state. This phenomenon arises due to the strong temperature dependency of CNO nuclear reactions, resulting in the generation of a substantial amount of energy within a narrow central region. Radiation alone proves inadequate for efficiently transporting this considerable energy in such a confined space. It's noteworthy that convective cores can also be encountered in certain

earlier phases (e.g., deuterium burning and out-of-equilibrium ^{3}He burning) as well as later burning stages (e.g., helium burning). Conversely, in stars where the pp-chain is the dominant nuclear burning process, a radiative core develops. The parameter that profoundly affects the efficiency of nuclear burning is temperature, and this is closely tied to the initial mass of the star. The transition point between the two hydrogen-burning channels occurs within the LMS range. Notably, stars with masses approximately in the range of 1.2 to 1.3 $M_\odot$ initiate the development of convective cores fueled by CNO-burning, with the size of these cores increasing with stellar mass. However, stars with masses exceeding the 1.2 to 1.3 $M_\odot$ range maintain a radiative region above the mixed core, where the pp-chain dominates.

2.2.2   Sub Giant Branch

Once hydrogen in the core is depleted, nuclear reactions in the centre stop. Consequently, the star departs from the MS phase and proceeds with its evolutionary course along the *Sub Giant Branch* (SGB), as illustrated in Fig. 2.1. At this point both the central luminosity and the temperature gradient drop to zero. The core, mainly made of helium, contracts and becomes hotter and denser. As a result, the layers immediately above the core increase their temperature too and ignite hydrogen nuclear reactions in a thick shell surrounding the core. The burning shell becomes thinner and thinner, converting hydrogen by the CNO-cycle channel into helium, which is deposited on the core. In the meantime, the envelope reacts to the contraction expanding and cooling down but maintaining an almost constant luminosity, following the *Stefan-Boltzmann law* for black bodies:

$$L = 4\pi\sigma R^2 T_{eff}^4. \tag{2.8}$$

The outer convection zone gradually extends deeper into the star's interior, and this phenomenon occurs as the star's effective temperature (T_{eff}) has considerably decreased. It reaches a crucial phase at the base of the *red giant branch* (see Section 2.2.3), transporting the byproducts of nuclear reactions to the stellar surface, a process often referred to as the *first dredge-up*. Depending on the initial mass, stars can develop an isothermal core in a non electron-degenerate regime. For such stars the hydrostatic equilibrium persists, supported by the density gradient only, until the mass of the helium core (which is in constant growth) exceeds the *Schönberg-Chandrasekhar limit* (Schönberg and Chandrasekhar 1942):

$$M_{SC} = 0.37 \cdot M \left(\frac{\mu_{env}}{\mu_{core}}\right)^2, \tag{2.9}$$

where μ_{env} and μ_{core} are respectively the *mean molecular weight* (average mass of the particles in a gas divided by the atomic mass unit) of the envelope and the core. A core mass larger than M_{SC}, starts to contract on a *Kelvin-Helmholtz timescale*, unless

the electron gas in core starts to become degenerate, in which case the contraction is significantly slowed down. If $M > M_{SC}$, due to the very fast evolution, it is not likely to observe stars in this phase, so in the CMDs of stellar populations we observe a "gap" known as the *Hertzspung gap*.

2.2.3 Red Giant Branch

Continuing along its evolution, the star then approaches the *Hayashi limit*, an almost vertical line in the HRD where fully convective objects are in hydrostatic equilibrium. Almost the entire envelope is convective and the H-burning shell is now thin. The core is still in contraction but T_{eff} cannot decrease any longer, since no stars in hydrostatic equilibrium can exist at T_{eff} cooler than the Hayashi limit. Therefore the only possibility to expand the envelope is to increase the luminosity: the *Red Giant Branch* (RGB) begins (Fig. 2.1). In low-mass stars the electron component of the gas gradually becomes fully degenerate and creates a strong pressure able to contrast the gravity and slows down the contraction of the core:

$$P_e \propto \rho^{5/3}. \tag{2.10}$$

The total pressure is now formed of two components: the pressure of the electrons P_e (2.10) and the pressure of the nuclei of helium which are still in a perfect gas condition:

$$P = P_e + P_{nuclei} = K\rho^{5/3} + \frac{k_B \rho T}{m_u \mu}, \tag{2.11}$$

where μ is the mean molecular weight, k_B is the Boltzmann's constant and m_u is the atomic mass unit. The pressure of the perfect gas component is negligible with respect to the degenerate component, hence the central temperature does not affect the total pressure but depends only on density. Since the H-burning shell is active, new helium is produced and deposited on the surface of the core, which grows in mass and becomes hotter and denser.

The H-burning shell is also responsible for the surface luminosity. It can be shown that luminosity and core mass are connected by homology relations, $L \propto M_{HeC}^{8-10}$. During the ascent on the RGB, the H-burning shell crosses the chemical discontinuity left by the first dredge-up. The monotonic increase of luminosity is abruptly interrupted since the molecular weight μ in H-shell decreases. In fact, the *homology relation* shows that $L \approx \mu^7$. Once the H-burning shell has passed the discontinuity, the luminosity rises again. In stellar populations with low-mass stars this event generates the *RGB-bump* (RGBb). Observationally speaking, the bump produces an accumulation of stars that is easily visible as a peak in the luminosity function of of the RGB in globular and open clusters.

Stellar evolution theory predicts a fundamental dichotomy between the evolutionary behaviour of stars that do, and those that do not develop electron degenerate cores after central hydrogen exhaustion. Stars of masses lower than about 1.8 - 2.2 $M_\odot$ develop degenerate cores, and climb the red giant branch (RGB) until the core mass grows to about 0.45 $M_\odot$. Degeneracy impose to LMS grow their helium core to the mass of approximately 0.45 $M_\odot$ in order to reach temperatures necessary to ignite the helium nuclear reactions. However, the pressure is dominated by the electron-degenerate component, therefore when energy is released by He-burning nuclear reactions the gas can not expand and cool down. Since the temperature and the nuclear energy production are strongly related, a thermal runaway occurs. When the temperature becomes high enough, the perfect gas component of the total pressure (2.11) is no longer negligible and the gas is free to expand and cool down, removing the degeneracy. The entire process is called *Helium Flash* (HeF). The maximum mass of stars that follow this evolutionary scheme is usually denoted as M_{Hef}. Stars of masses slightly above M_{Hef} have a weakly degenerate core, and are able to ignite helium with a lower core mass, of about 0.33 $M_\odot$; therefore their RGB phase is significantly abbreviated. For stars of higher masses, the core mass at He ignition becomes an increasing function of stellar mass, and the evolutionary phase equivalent to the RGB is practically missing.

2.2.4   Quiescent Core He Burning Phase (QCHeB)

Once the degeneracy is removed from the core (in LMS) or helium burning in a non-degenerate core is set up (in IMS), the star is subject to a fast readjustment (decreases its L and R, with a slight increase in T_{eff}) to reach the new equilibrium configuration with the new available source of energy. During this stable core-He burning phase, also called *Quiescent Core He Burning Phase* (QCHeB), the star has a different structure and global properties with respect to the RGB phase. From the surface to the centre, the internal structure consists of a large convective envelope, a H-burning shell and a region composed primarily of helium. At the center two nuclear reactions are present simultaneously: the *triple-α reactions* and *carbon into oxygen reaction* ($^{12}C(\alpha,\gamma)^{16}O$). Given the high dependence on the temperature of helium-burning reactions, nuclear energy generation is confined inside a very compact and convective core. Due to the central convection, the helium burning core is chemically homogeneous. Therefore, since the core grows, a chemical discontinuity at the convective border develops, and becomes more and more pronounced as He-burning proceeds (the situation changes depending on the mixing prescription adopted to define the convective boundaries).

At the beginning of the helium burning phase, the triple-α reactions dominate until the mass fraction of helium in the core drops under approximately 0.2. Then, the energy

production by the $^{12}C(\alpha,\gamma)^{16}O$ reactions becomes greater than that by the triple-α reactions. The entire helium core becomes more compact, the H-burning shell increases its energy generation rate and the total luminosity rises.

Red Clump and Secondary Clump

During the red giant phase, the star spends most of its lifetime in the loop corresponding to the stable core helium-burning phase. Consequently, it is much more likely to observe a red giant star during the QCHeB phase than during its rapid evolution on the red giant branch in the hydrogen shell-burning phase. This is observed in the CMDs of stellar populations as a clump of stars in the region corresponding to this phase which is called the *Red Clump* (RC). The difference in the core mass at the beginning of the stable core He-burning phase reflects directly on the luminosity of these stars: for $M < M_{Hef}$ their luminosity is almost constant at $Log(L/L_\odot) \approx 1.5$ which gives an origin to the clump of red giant stars (or to the horizontal branch in the case of Population II stars); for masses slightly above M_{Hef} this luminosity is predicted to have a minimum value about 0.4 mag below the clump of lower mass stars; and for still higher total mass the He-burning stars shift progressively to higher luminosities (see Fig. 5.12), so that they no longer correspond to the "red clump". This "dip" in luminosity generates, in the CMDs of composite stellar populations, an extension to lower luminosities, called *Secondary Clump* (2RC), which goes down about 0.4 mag below the main clump of lower mass stars and at its blue extremity (Girardi et al. 1998 and Girardi 1999). The exact values of the stellar masses and luminosities in the 2RC depend slightly on the assumed values of Z and Y. The limiting mass M_{Hef} also depends, as discussed extensively in Section 5.2 on the efficiency of near-core mixing processes during the MS phase.

2.2.5   Asymptotic Giant Branch

As helium becomes depleted in the core, the process of He-burning ceases. Consequently, the central convective region rapidly diminishes and vanishes. Both the luminosity at the core and the temperature gradient decline to zero, causing the core to become nearly isothermal. The star approaches the Hayashi limit again, initiating a phase known as the *Asymptotic Giant Branch (AGB)*. During this phase, the core contracts again. Analogous to the hydrogen-burning in the Subgiant Branch (SGB), helium-burning ignites within a shell. The nuclear burning in the helium shell is non-convective, thus, as the helium abundance diminishes, the helium-burning shell moves outward, leaving behind the byproducts of nuclear reactions. This leads to an increase in the mass of the C/O core and brings the helium shell closer to the hydrogen-burning shell.

Throughout the AGB phase, the star's internal structure can be described as follows:

- a core primarily composed of carbon and oxygen, accompanied by degenerate electrons,

- a shell where helium-burning occurs,

- a shell for hydrogen-burning,

- a deep convective envelope.

In the CMDs of stellar populations, the formation of the helium-burning shell corresponds to what is known as the *AGB bump* (AGBb). Analogous to the RGBb, this AGBb consists in an initial decrease followed by an increase in the total luminosity. The reason for the occurrence of the AGBb is immediately evident after the cessation of Helium-core burning. Without nuclear energy production at the core, the entire stellar structure adjusts to compensate for the loss of this energy source. Beyond the boundary of the former convective core, the energy generation rate due to He-burning reactions increases in a shell. This is primarily due to the higher helium abundance in relation to the inner region (the discontinuity) and the temperature profile. Initially, due to the expansion of the layers between the two shells, both the luminosity from hydrogen-shell-burning and the total luminosity decrease, while the helium shell contributes an increasing portion to the total luminosity. Eventually, the He-burning shell surpasses the H-burning shell as the primary source of nuclear energy. Consequently, the total luminosity begins to rise anew, whereas the energy output of the H-burning shell diminishes, as it has expanded and cooled due to the ignition of a secondary burning shell.

Towards the conclusion of the AGB phase, the two shells approach each other closely and undergo periodic thermal instabilities, termed *Thermal Pulses*. During these pulses, the helium-burning shell experiences periodic thermonuclear runaways. As a result of the huge energy release, an inter-shell convective zone forms, extending toward the hydrogen/helium discontinuity, where the hydrogen-burning shell is located. During this phase, the helium-burning shell and the hydrogen-burning shell alternately switch on and off. When the hydrogen-burning shell is switched off following the reignition of the helium-burning shell, the convective envelope can move inward in terms of mass, crossing the hydrogen/helium discontinuity. In such instances, a new dredge-up event takes place, known as the *third dredge-up*[5]. During the third dredge-up, helium, products of helium burning (mainly carbon), and heavy s-elements[6] are brought up into the envelope and eventually transported to the surface, where they become observable.

---

[5]For stars more massive than 3-5 $M_\odot$ there is a *second dredge up* in the early- AGB phase that does not happen in lower mass stars.

[6]*s-elements* refer to elements formed primarily through the slow neutron-capture process (s-process) in stars, leading to their abundance in the s-process-rich materials. These elements include strontium (Sr), barium (Ba), yttrium (Y), and other heavier isotopes.

Instabilities at the base of the envelope lead to its detachment from the star, resulting in the formation of a Planetary Nebula (PN). The remnant takes the form of a compact object, primarily composed of carbon and oxygen and existing under high electron degeneracy. This compact object is referred to as a *White Dwarf* (WD).
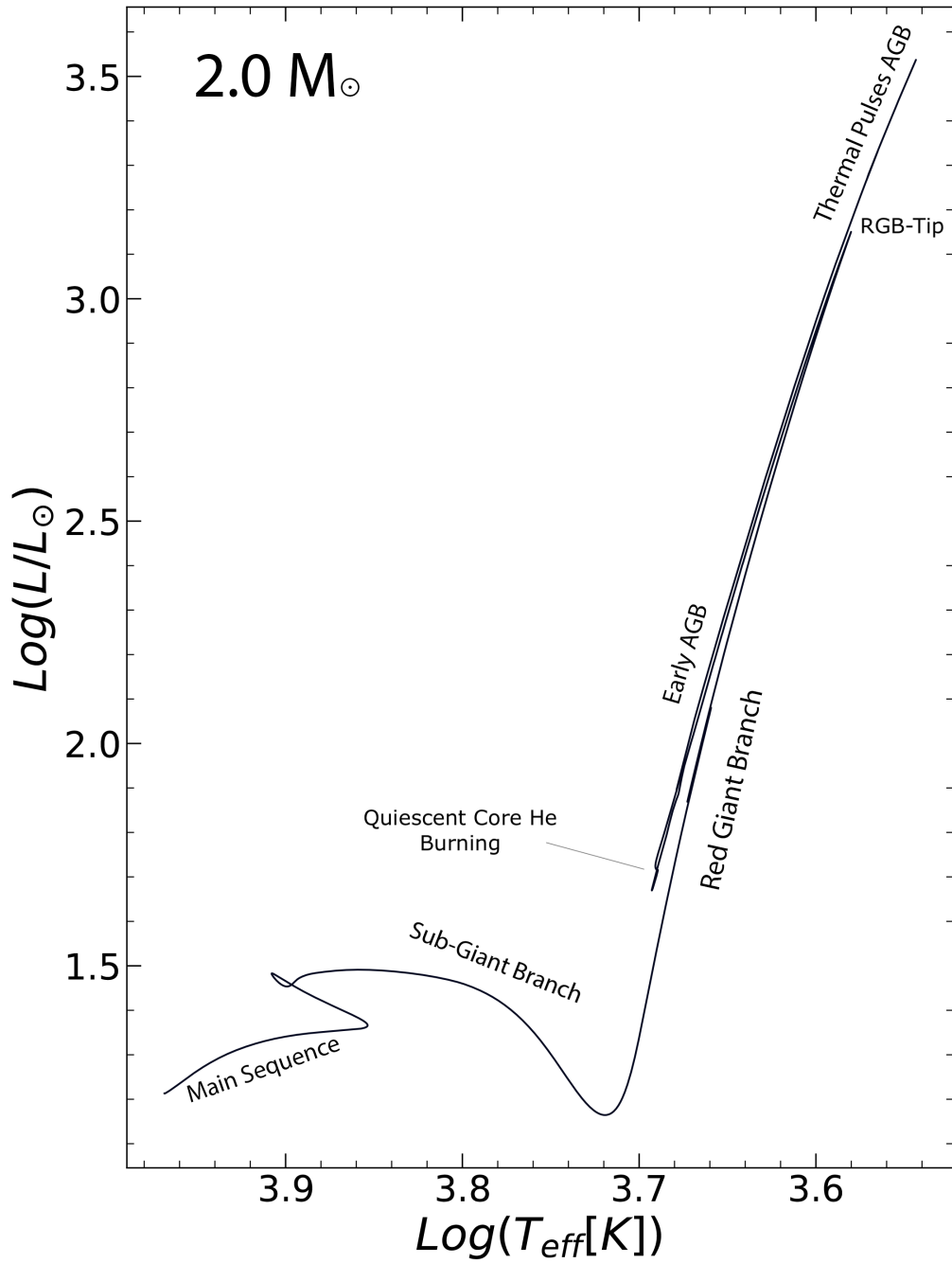
Figure 2.1: Evolutionary track of 2.0 $M_\odot$ from our grid of models described in Section 4.1 computed up to the first thermal pulse.

Chapter 3

Rotating Stars

Thanks to the numerous achievements of the standard theory of stellar evolution, rotation has mostly been seen as a secondary factor. This viewpoint has been reasonable in many cases. However, notable differences and uncertainties have arisen between the expectations of models without rotation and observations. These differences apply not only to massive stars but also to those with lower masses. The main challenge in accurately determining stellar ages has now shifted to uncertainties related to the modelling of transport processes within stars. In this context, rotation emerges as a natural driver for these transport processes or, at the very least, as a key aspect that needs thorough investigation to understand its impact on chemical mixing. Also, it is important to note that that there is clear observational evidence of the effects of rotation. This evidence originates from spectroscopic analyses, and more recently through measurements from interferometry, chemical composition studies, and from studying solar and stellar oscillations. The abundance of evidence itself emphasizes the importance of studying how rotation influences stars.

The physical effects of stellar rotation are numerous. Rotation shapes the course of stellar evolution through two distinct mechanisms:

- **Equilibrium Configuration Deformation**: there is a deformation (flattening) of the equilibrium configuration: the characteristics become dependent on the colatitude considered. This alteration impacts the stellar parameters inferred from observations and introduces an anisotropic pattern in the star's mass loss.

- **Generation of Internal Circulation and Instabilities**: Rotation drives internal circulation motions and various instabilities which transport both the chemical elements and the angular momentum. These mechanisms result in significant deviations from the standard (non-rotating) evolution.

Given these considerations, it becomes evident that the fundamental equations governing stellar structure need to be modified.

In the following sections we will give a basic physical description of stellar rotation in order to illustrate the concepts needed to understand and interpret the results of the rotating stellar models. Moreover we will discuss the different approaches in implementing rotation in stellar evolution codes and describe broadly the properties of rotating models, how they compare with observations and, in some more detail, the properties of a small grid of rotating models computed with the Geneva stellar evolution code (Eggenberger et al. 2008) also referred to as GENEC, that we will use as reference rotating models for this work.

3.1 Physical Description of Stellar Rotation

In a rotating star, the centrifugal forces lead to a reduction in effective gravity, which varies with colatitude and introduces deviations from sphericity. When rotation is present, the four equations governing stellar structure need to be modified. The original approach, introduced by Kippenhahn and Thomas 1970 and subsequently adopted in many works, involves substituting the conventional spherical Eulerian or Lagrangian coordinates with new coordinates that define equipotential surfaces. This method is applicable in cases where the effective gravity can be derived from a potential, i.e. when the problem is conservative. This holds true for scenarios like solid body rotation or constant rotation along cylinders centered on the rotation axis. Although internal rotation often evolves towards non-conservative rotation laws, rendering this method not physically consistent, it still proves valuable not only because it approximates real systems (or portions of them) reasonably well, but also because it offers insights into concepts that remain relevant even in more complex models.

3.1.1 Hydrostatic Equilibrium for Solid Body Rotation

Let's consider a fluid in rotation with a constant angular velocity denoted by Ω. This angular velocity is the same throughout the fluid. We will use primed symbols, such as $\boldsymbol{r'}$, $\boldsymbol{v'}$, $\boldsymbol{\Omega'}$, $\boldsymbol{a'}$, to denote quantities measured within the rotating reference frame. Conversely, unprimed symbols, like $\boldsymbol{r}$, $\boldsymbol{v}$, $\boldsymbol{\Omega}$, $\boldsymbol{a}$, will represent the equivalent quantities measured within the non-rotating reference frame. In the rotating reference frame we have that the equation of *apparent motion* of a fluid element of mass m, is:

$$m\boldsymbol{a'} = \boldsymbol{f} - m\boldsymbol{\Omega} \times (\boldsymbol{\Omega} \times \boldsymbol{r}) - 2m\boldsymbol{\Omega} \times \boldsymbol{v}. \tag{3.1}$$

where $\boldsymbol{f}$ indicates the forces acting on the fluid element. The second term on the right-hand side of equation (3.1) is the *centrifugal force*, while the third term represents the *Coriolis' force*. These forces are referred to as *fictitious* because they arise from the non-inertial nature of the rotating reference frame.

Assuming hydrostatic equilibrium within the rotating reference frame and neglecting the viscous components in the Navier-Stokes equations, the set of hydrodynamic equations simplifies to:

$$\frac{1}{\rho}\boldsymbol{\nabla}p = -\boldsymbol{\nabla}\Phi - \boldsymbol{\Omega} \times (\boldsymbol{\Omega} \times \boldsymbol{r}). \tag{3.2}$$

In this equation, ρ and p stand for density and pressure, respectively, while Φ represents the *gravitational potential*. The second term on the right-hand side of equation (3.2) represents the *centrifugal acceleration*, denoted as $\boldsymbol{g}_c$. When expressed in spherical coordinates (r, θ, Φ), the centrifugal acceleration takes the form:

$$\boldsymbol{g}_c = \Omega^2 r \sin\theta(\sin\theta \boldsymbol{e_r} + \cos\Phi \boldsymbol{e_\theta}). \tag{3.3}$$

This expression can be derived from the gradient of the centrifugal potential, as outlined below[1]. The centrifugal potential χ is defined as:

$$\chi(r, \theta) = -\frac{\Omega^2 r^2}{2}\sin^2\theta. \tag{3.4}$$

Moving on to the gravitational potential Φ, it is defined by the equation:

$$\boldsymbol{g}_g = -\boldsymbol{\nabla}\Phi. \tag{3.5}$$

Here, $\boldsymbol{g}_g$ represents the gravitational acceleration. We'll consider a system that is spherically symmetric, and we'll assume that rotation doesn't modify the potential Φ. This assumption, known as the *Roche approximation*, can be mathematically expressed as:

$$\Phi \approx -\frac{GM_r}{r} \quad \text{or} \quad \boldsymbol{g}_g \approx -\frac{GM_r}{r^2}\frac{\boldsymbol{r}}{r}. \tag{3.6}$$

We introduce the total potential ψ as:

$$\Psi = \Phi + \chi. \tag{3.7}$$

With this definition, we can reconfigure the equation of hydrostatic equilibrium as follows:

$$\frac{1}{\rho}\boldsymbol{\nabla}p = -\boldsymbol{\nabla}\Psi \quad \text{or} \quad \frac{1}{\rho}\boldsymbol{\nabla}p = \boldsymbol{g}_{eff}. \tag{3.8}$$

Here, $\boldsymbol{g}_{eff}$ represents the effective gravity, which combines both gravitational and centrifugal acceleration. It can be expressed as:

$$\boldsymbol{g}_{eff} = -\boldsymbol{\nabla}\Psi. \tag{3.9}$$

Equation (3.8) implies that pressure remains uniform on an equipotential surface, denoted as $p = p(\psi)$. Consequently, the equipotential lines coincide with lines of constant pressure

---

[1]It is important to note that this holds true not only for a constant $\boldsymbol{\Omega}$, but also when $\boldsymbol{\Omega}$ is constant on cylindrical surfaces.

(isobars). This characteristic designates a star as *barotropic*. Conversely, if the pressure is not uniform on equipotential surfaces, the star is said to be *baroclinic*.

If the star is indeed barotropic, an additional relation holds:

$$\nabla p = \frac{dp}{d\Psi}\nabla\Psi. \tag{3.10}$$

Substituting (3.10) into (3.8) yields:

$$\frac{1}{\rho}\frac{dp}{d\Psi} = -1. \tag{3.11}$$

Consequently, density is exclusively a function of ψ, that is, $\rho = \rho(\psi)$. Through the equation of state $p = p(\rho, T)$, it can also be deduced that $T = T(\psi)$. Hence, the quantities ρ, p, and T all remain constant on equipotential surfaces defined by $\psi = const$.

3.1.2 Stellar Surface and Gravity

The surface of the star represents an equipotential ($\psi = const.$), as any deviation from this would lead to the formation of "mountains" on the star's surface and cause material to flow from higher to lower levels. By combining equations (3.4), (3.6), and (3.7), the total potential at a given radius r and colatitude θ ($\theta = 0$ at the pole) can be formulated as follows:

$$\Psi(r,\theta) = -\frac{GM_r}{r} - \frac{1}{2}\Omega^2 r^2 \sin^2\theta. \tag{3.12}$$

Consider a star with a total mass M, and let $R(\theta)$ denote the stellar radius at colatitude θ. Given that the centrifugal force is absent at the pole, the potential at the stellar pole simplifies to $-GM/R_p$, where R_p represents the polar radius. This establishes the constant value of the equipotential at the star's surface, given by:

$$\frac{GM}{R(\theta)} + \frac{1}{2}\Omega^2 R^2(\theta)\sin^2\theta = \frac{GM}{R_p}. \tag{3.13}$$

The resultant effective gravity, arising from both the gravitational potential and the centrifugal force, is expressed in equation (3.9). Assuming $\boldsymbol{e}_r$ and $\boldsymbol{e}_\theta$ as unit vectors in the radial and latitudinal directions respectively, the effective gravity vector at the star's surface can be described as:

$$\boldsymbol{g}_{eff} = \left[-\frac{GM}{R^2(\theta)} + \Omega^2 R(\theta)\sin^2\theta\right]\boldsymbol{e}_r + \left[\Omega^2 R(\theta)\sin\theta\cos\theta\right]\boldsymbol{e}_\theta. \tag{3.14}$$

The gravity vector is not aligned with the radius vector. The magnitude $g_{eff} = \|\boldsymbol{g}_{eff}\|$ of the effective gravity is:

$$g_{eff} = \left[\left(-\frac{GM}{R^2(\theta)} + \Omega^2 R(\theta)\sin^2\theta\right) + \Omega^4 R^2(\theta)\sin^2\theta\cos^2\theta\right]^{\frac{1}{2}}. \tag{3.15}$$
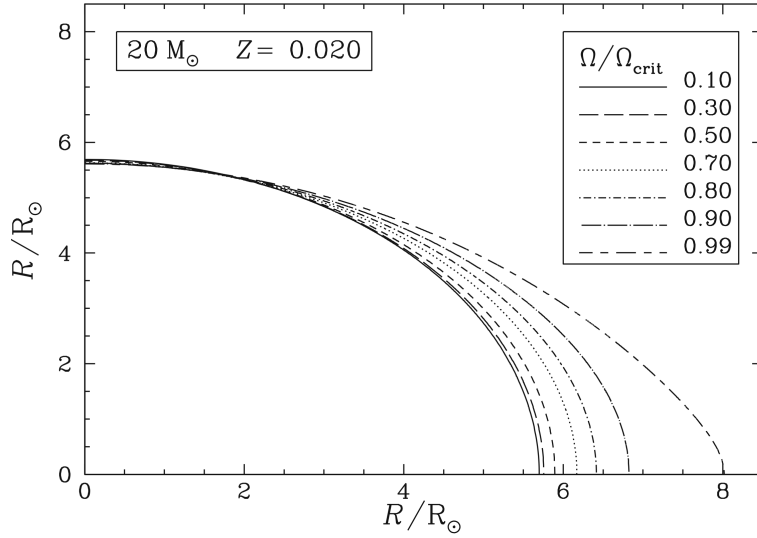
Figure 3.1: The shape of $R(\theta)$ in a quadrant of rotating 20 M$_\odot$ models with Z=0.02 on the ZAMS. One barely notices the small decrease of the polar radii for higher rotation velocities. Taken from Maeder 2009.

When the magnitude of the centrifugal force equals that of the gravitational attraction at the equator, the star is said to be rotating at the *critical velocity*, or *break-up velocity*. From equation (3.15), the critical angular velocity Ω_{crit} that yields $g_{eff} = 0$ at the equator ($\theta = \pi/2$) is given by:

$$\Omega_{crit}^2 = \frac{GM}{R_{e,crit}^3}, \tag{3.16}$$

Here, $R_{e,crit}$ denotes the *equatorial radius at break-up*. Substituting this value of Ω_{crit} into the surface equation (3.13) at the point of break-up yields the ratio of equatorial radius to polar radius at critical velocity:

$$\frac{R_{e,crit}}{R_{p,crit}} = \frac{3}{2}. \tag{3.17}$$

At break-up, the equatorial radius is 1.5 times the polar radius. The *equatorial break-up velocity* is then calculated as follows:

$$v_{crit}^2 = \Omega_{crit}^2 R_{e,crit}^2 = \frac{GM}{R_{e,crit}} = \frac{2GM}{3R_{p,crit}}. \tag{3.18}$$

This expression is commonly used; however, formally, it is applicable to solid body rotation. Now, introducing a non-dimensional rotation parameter ω, defined as the ratio of angular velocity to the angular velocity of break-up:

$$\omega = \frac{\Omega}{\Omega_{crit}} \quad \Longrightarrow \quad \omega^2 = \frac{\Omega^2 R_{e,crit}^3}{GM}. \tag{3.19}$$

This can also be expressed as:

$$\Omega^2 = \frac{8}{27}\frac{GM\omega^2}{R_{p,crit}^3}, \tag{3.20}$$

And the surface equation (3.13) can be rewritten in terms of a non-dimensional parameter $x = R/R_{p,crit}$ as:

$$\frac{1}{x} + \frac{4}{27}\omega^2 x^2 \sin^2\theta = \frac{R_{p,crit}}{R_p(\omega)}. \tag{3.21}$$

Equation (3.21) is a cubic algebraic equation. Fig. 3.2 shows the critical velocities v_{crit} for stars of various masses and metallicities. The critical velocities grow with stellar masses, because the stellar radii increase only slowly with stellar masses. The critical velocities are very large for low metallicity stars, since their radii are much smaller as a result of their lower opacities. The shape of a Roche model is illustrated in Fig. 3.1 for different
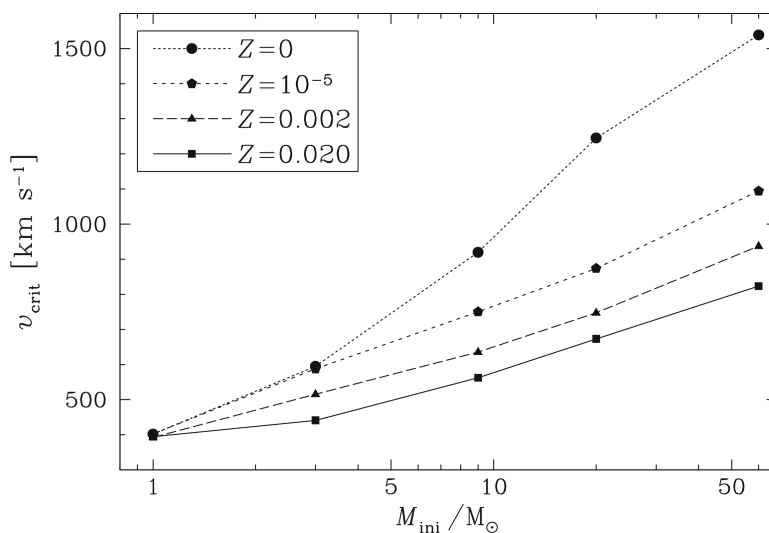

Figure 3.2: The critical velocities v_{crit} as a function of stellar masses for different metallicities Z for stars on the ZAMS. The effect of the changes of the polar radius with rotation is accounted for. Taken from Maeder 2009.

rotation velocities. Fig. 3.3 shows the variation of the ratio of the equatorial radius to the polar radius for the Roche model as a function of the parameter $\omega = \Omega/\Omega_{crit}$. We see that up to $\omega = 0.7$, the increase of the equatorial radius is inferior to 10%. The substantial increase in the equatorial radius predominantly takes place within the high rotation regime.

3.1.3 Breakdown of Radiative Equilibrium

Within the interior of the star, the departure from radiative equilibrium on equipotential surfaces triggers internal fluid motions known as *meridional circulation currents* (as discussed in Section 3.1.6). These currents are extensive and contribute to the mixing of chemical elements as well as the transport of angular momentum. Both of these effects play a substantial role in influencing the course of the star's evolution.
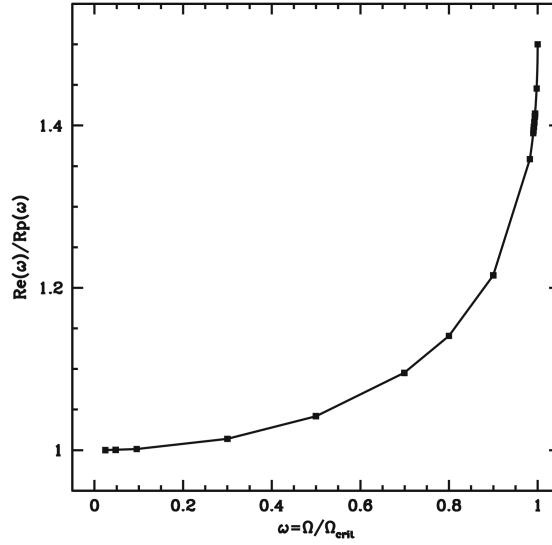
Figure 3.3: The variation of the ratio R_e/R_p of the equatorial to the polar radius as a function of the rotation parameter ω in the Roche model. Taken from Maeder 2009.

The deviation from radiative equilibrium on equipotential surfaces becomes evident through a straightforward analysis of the radiative flux expression. Consider the scenario of a star exhibiting solid body rotation. As outlined in Section 3.1.1, the temperature T, pressure P, and density ρ are solely functions of the total potential Ψ, encompassing both gravity and rotation effects. At a specific level r, the radiative flux is given by:

$$\boldsymbol{F} = -\frac{4acT^3}{3\kappa\rho}\boldsymbol{\nabla}T = \left(-\frac{4acT^3}{3\kappa\rho}\frac{dT}{d\Psi}\right)\boldsymbol{\nabla}\Psi. \tag{3.22}$$

This is due to $T = T(\Psi)$, with the same being applicable for ρ and P. Notably, the terms within the parentheses in the above expression are functions solely of Ψ, as the opacity κ relies on ρ and T. Therefore, we can deduce the following observations:

- The radiative flux is aligned with the gradient of Ψ.

- On an equipotential, the flux is solely proportional to $\boldsymbol{\nabla}\Psi$, as the term in parentheses remains constant across equipotentials.

This implies that a change in temperature (T) on a level surface will solely impact the average flux, without altering the flux's direction or its relative contributions based on the surface's location. Now, we calculate the divergence of the radiative flux, which should be zero in the absence of energy production or absorption:

$$\nabla \cdot \boldsymbol{F} = \frac{d}{d\Psi}\left(-\frac{4acT^3}{3\kappa\rho}\frac{dT}{d\Psi}\right)(\nabla\Psi)^2 + \left(-\frac{4acT^3}{3\kappa\rho}\frac{dT}{d\Psi}\right)\nabla^2\Psi. \tag{3.23}$$

Additionally, from (3.4)-(3.6)-(3.7), it follows that $\nabla^2\Psi = 4\pi G\rho - 2\Omega^2$, where Ω represents the constant angular velocity. Consequently, in (3.23), all quantities remain constant on

an equipotential except $\nabla\Psi$, as the equipotentials exhibit varying spacings with respect to colatitude θ. In polar regions, they are closer together, whereas they are more spread out in equatorial regions. Consequently, $\nabla\cdot\boldsymbol{F}$ must change on an equipotential, unlike the case where radiative equilibrium holds everywhere, and $\nabla\cdot\boldsymbol{F}$ would be uniformly zero. This local variation leads to the local breakdown of radiative equilibrium. On average over an equipotential, $\langle\nabla\cdot\boldsymbol{F}\rangle = 0$, as no energy is locally produced or consumed. When transitioning from the pole to the equator, $\nabla\cdot\boldsymbol{F}$ assumes positive values over a range of colatitudes and negative values over others. When $\nabla\cdot\boldsymbol{F} > 0$ locally, there is an excess of energy within the medium, causing it to heat up and ascend locally. Conversely, in the opposite scenario, cooler regions lead to descending motion.

The first term in the right-hand side of (3.23), which behaves like $(\nabla\Psi)^2$, is more significant at the pole than at the equator (particularly more pronounced in the deep interior compared to external regions). This term primarily drives the circulation currents. For the case of solid body rotation, it implies that within the deep radiative layers, circulation motion rises at the pole and descends at the equator, in response to local deviations from radiative equilibrium. Further exploration of this circulation is carried out in Section 3.1.6.

3.1.4   The Von Zeipel Theorem

The *Von Zeipel theorem* establishes a relationship between the radiative flux at a specific colatitude θ on the surface of a rotating star and the local effective gravity $\boldsymbol{g}_{eff}(\Omega,\theta)$. This flux is given by (3.22) and as previously highlighted, in the case of a star rotating as a solid body, the equipotentials and isobars coincide (barotropic). Moreover they also represent surfaces of constant T and ρ. Utilizing the equation of hydrostatic equilibrium (3.8), one can express (3.22) as:

$$\boldsymbol{F}(\Omega,\theta) = -\frac{4acT^3}{3\kappa\rho}\frac{dT}{dP}\nabla P(\Omega,\theta) = -\rho\frac{4acT^3}{3\kappa\rho}\frac{dT}{dP}\cdot\boldsymbol{g}_{eff}(\Omega,\theta). \qquad (3.24)$$

Notably, the pressure gradient and effective gravity are parallel. The term $(\rho\frac{4acT^3}{3\kappa\rho}\frac{dT}{dP})$ remains constant on a given equipotential, leading to the flux being proportional to the effective gravity on the equipotential.

It can be demonstrated (Maeder 2009) that:

$$\boldsymbol{F}(\Omega,\theta) = -\frac{L}{4\pi GM^*}\cdot\boldsymbol{g}_{eff}(\Omega,\theta) \qquad (3.25)$$

$$\text{with}\quad M^* = M\left(1 - \frac{\Omega^2}{2\pi G\overline{\rho}_M}\right). \qquad (3.26)$$

Here, $\overline{\rho}_M$ represents the average density of the star. Equation (3.25) constitutes the *Von Zeipel theorem* (von Zeipel 1924), which implies that the radiative flux at the surface

of a rotating star is proportional to the local effective gravity at the considered colatitude. According to the *Stefan-Boltzmann law*, $F = \sigma T^4$, which means that the effective temperature also takes on a dependency on Ω and θ:

$$T_{eff} = \left[\frac{L}{4\pi\sigma GM^*} g_{eff}(\Omega, \theta) \right]^{1/4}. \tag{3.27}$$

Both g_{eff} and T_{eff} exhibit variation across the surface of a rotating star and consequently influence the emergent spectrum. Equatorial regions appear dimmer and cooler compared to polar areas, which are brighter and hotter. This phenomenon is termed *gravity-darkening.* Given that deformation becomes notable only during rapid rotation
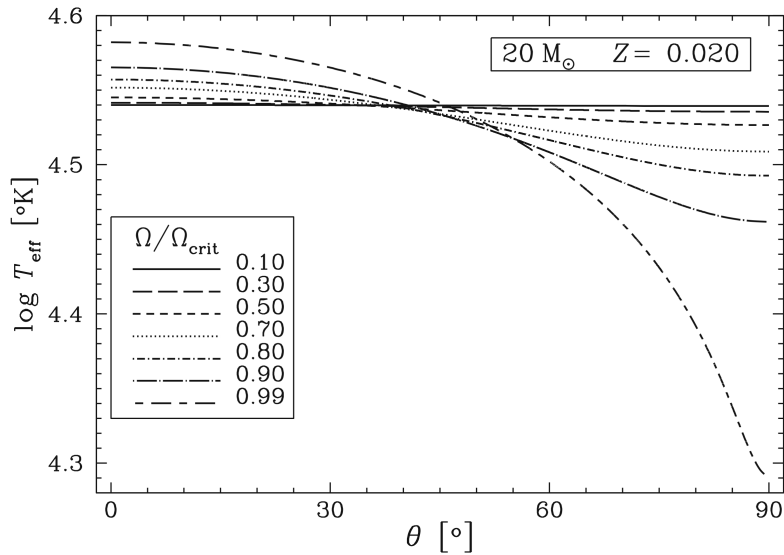
Figure 3.4: The local T_{eff} as a function of the colatitude θ for the same models of Fig. 3.1. Taken from Maeder 2009.

($\omega > 0.7$), stars observed at this magnitude present higher L and T_{eff} when viewed pole-on compared to the same star observed with an average inclination. Conversely, a rapidly-rotating star viewed equator-on will appear dimmer and cooler than usual (Georgy et al. 2014a). This can potentially impact the inferred mass and age for the observed star.

3.1.5   Shellular Rotation

Internal rotation within stars generally evolves towards rotation laws that are non-conservative, which renders the treatment described in the preceding sections physically inconsistent. However, as demonstrated by Meynet and Maeder 1997, it remains possible to formulate the equations of stellar structure consistently by employing coordinates that refers to the mass enclosed within isobaric surfaces. Consequently, the problem of addressing the structural properties of a differentially rotating star characterized by an

angular velocity $\Omega = \Omega(r)$ can be reduced to a one-dimensional problem. This specific form of differential rotation is referred to as *shellular rotation*, and its validity is supported by studies of turbulence in the sun and other stars (Spiegel and Zahn 1992, Zahn 1992). Such a law results from the fact that turbulence is very anisotropic, with a much stronger, geostrophic-like transport[2] in the horizontal direction than in the vertical one, where stabilization is favored by the stable temperature gradient and gradients in chemical composition. The horizontal turbulence enforces essentially constant rotation rate on isobars, thus producing the above mentioned rotation law. Given the relationship $\nabla P = \rho \boldsymbol{g}_{eff}$, the phrase "constant in the horizontal direction" signifies constancy along isobars, that is, $\Omega = \Omega(P)$. At a specific point (r, θ) in spherical coordinates, the angular velocity Ω is expressed as:

$$\Omega(P, \theta) = \overline{\Omega}(P) + \hat{\Omega}(P, \theta), \tag{3.28}$$

where $\hat{\Omega} << \overline{\Omega}$ (the average $\overline{\Omega}$ over an isobar with radius r is determined to satisfy the angular momentum conservation equation 3.47, see Maeder 2009). The term $\hat{\Omega}(P, \theta)$ can be expanded using *Legendre polynomials*[3]. Taking into account terms beyond the second order allows for the consideration of higher rotation velocities (Mathis and Zahn 2004). Up to second order, the following expression holds:

$$\hat{\Omega}(P, \theta) = \Omega_2(P) P_2(\cos\theta), \tag{3.29}$$

where $P_2(\cos\theta)$ denotes the *second Legendre polynomial*.

Various variables, such as P, T, ρ, etc., can be represented using Legendre polynomials. For instance, a generic quantity $f(P, \theta)$ can be decomposed into its mean value and its latitudinal perturbation:

$$f(P, \theta) = \overline{f}(P) + f_2(P) P_2(\cos\theta). \tag{3.30}$$

It is important to highlight that the isobars are not spherical surfaces. There exists an angle ϵ between the radial direction and the direction of gravity, or between a spherical shell and an equipotential surface. Thus, when expressing shellular rotation as $\Omega \approx \Omega(r)$, extreme rotation velocities are not considered in this context.

---

[2]Geostrophic flow is a flow characterised by the balance between pressure, gravity and Coriolis forces. An imbalance between pressure gradient and gravity can forces the fluid to start moving. As soon as the fluid starts to move, the Coriolis force acts at right angles to this movement. The faster the flow speed, the greater the deflection. Eventually the Coriolis force will balance the pressure gradient force and the flow will move parallel to the isobars.

[3]The Legendre polynomials are a set of orthogonal functions utilized to solve Laplace's equation $\nabla^2 \Phi = 0$ in spherical coordinates when azimuthal symmetry $\partial \Phi = 0$ is present. The second-order Legendre polynomial is $P_2(x) = \frac{1}{2}\left(3x^2 - 1\right)$.

Properties of the Isobars

In the case of shellular rotation, the centrifugal force cannot be derived from a potential. Let's focus on the surface of constant Ψ (3.12), which, in this context, is not an equipotential [4]:

$$\Psi = \Phi - \frac{1}{2}\Omega^2 r^2 \sin^2 \theta = const. \tag{3.31}$$

It is important to note that in this case, Ω is no longer constant. As in Section 3.1.1, the gravitational potential is defined by $\partial\Phi/\partial r = GM_r/r^2$ and $\Phi = -GM_r/r$ in the Roche approximation. The components of the gradient of ψ in polar coordinates (r, θ) are given by:

$$\frac{\partial\Psi}{\partial r} = \frac{\partial\Phi}{\partial r} - \Omega^2 r \sin^2 \theta - r^2 \sin^2 \theta \Omega \frac{\partial\Omega}{\partial r}, \tag{3.32}$$

$$\frac{1}{r}\frac{\partial\Psi}{\partial\theta} = \frac{1}{r}\frac{\partial\Phi}{\partial\theta} - \Omega^2 r \sin\theta\cos\theta - r^2 \sin^2 \theta \Omega \frac{1}{r}\frac{\partial\Omega}{\partial\theta}. \tag{3.33}$$

In the Roche model, according to (3.14), the first two components of the effective gravity $\boldsymbol{g}_{eff} = (-g_{eff,r}, g_{eff,\theta}, 0)$ are:

$$g_{eff,r} = \frac{\partial\Phi}{\partial r} - \Omega^2 r \sin^2 \theta, \tag{3.34}$$

$$g_{eff,\theta} = \Omega^2 r \sin^2 \theta \cos\theta. \tag{3.35}$$

By comparing these expressions with the derivatives of Ψ, we can write:

$$\boldsymbol{g}_{eff} = -\boldsymbol{\nabla}\Psi - r^2 \sin^2 \theta \Omega \boldsymbol{\nabla}\Omega. \tag{3.36}$$

The equation of hydrostatic equilibrium $\boldsymbol{\nabla}P = \rho\boldsymbol{g}_{eff}$ becomes:

$$\boldsymbol{\nabla}P = -\rho(\boldsymbol{\nabla}\Psi + r^2 \sin^2 \theta \Omega \boldsymbol{\nabla}\Omega). \tag{3.37}$$

Given that Ω is constant on isobars, the vector $\boldsymbol{\nabla}\Omega$ is parallel to $\boldsymbol{\nabla}P$. Equation (3.37) implies that $\boldsymbol{\nabla}P$ and $\boldsymbol{\nabla}\Psi$ are parallel. Therefore, in this non-conservative case, the surfaces defined by $\Psi = const.$ (3.31) are isobaric surfaces. It is worth noting that the shape of these isobars for a *shellular rotation law* matches the shape of equipotential surfaces in a conservative scenario. However, the effective gravity can't be defined as $\boldsymbol{g}_{eff} = -\boldsymbol{\nabla}\Psi$ anymore, as Ψ is not a potential. Consequently, for shellular rotation, one can choose to formulate the equation of stellar structure on the isobars, making use of a method similar to the one designed for the conservative case (Meynet and Maeder 1997). This approach retains the advantage of maintaining one-dimensional equations for stellar structure.

---

[4]An equipotential is defined by the condition that a displacement $\boldsymbol{ds}$ on the equipotential neither requires nor produce energy, so $\boldsymbol{g}_{eff} \cdot \boldsymbol{ds} = 0$

Equation of the Surface for Shellular Rotation

In the context of shellular rotation, the equation for the isobars is defined by the expression (3.31), which interestingly matches the expression describing equipotentials in the case of solid body rotation. To explore the equation governing equipotentials, particularly for the star's surface, we consider the condition where a displacement $\boldsymbol{ds}$ on the equipotential neither requires nor produce energy:

$$\boldsymbol{g}_{eff} \cdot \boldsymbol{ds} = 0. \tag{3.38}$$

Using the expression for the effective gravity provided by (3.36), this equation can be expressed as:

$$\frac{\partial \Psi}{\partial r} + \frac{1}{r}\frac{\partial \Psi}{\partial \theta}rd\theta + r^2\sin^2\theta\,\Omega\frac{\partial}{\partial r}dr + r^2\sin^2\theta\frac{\Omega}{r}\frac{\partial\Omega}{\partial\theta}rd\theta = 0. \tag{3.39}$$

When considering shellular rotation, where Ω approximately depends on r, this equation simplifies to:

$$d\Psi + r^2\sin^2\theta\,\Omega\frac{d\Omega}{dr}dr = 0. \tag{3.40}$$

This is a more generalized version of the equation describing equipotentials. If Ω is a constant, this simplifies further to $\Psi = const.$, aligning with the familiar result. Integrating the equation above leads us to the equation governing the shape $R(\theta)$ of the stellar surface as a function of $\Omega(r)$ in the outer regions:

$$-\frac{GM}{R(\theta)} - \frac{1}{2}\Omega^2 R^2(\theta)\sin^2\theta + \sin^2\theta\int_{R_p}^{R(\theta)} r^2(\theta)\Omega\frac{d\Omega}{dr}dr = \frac{GM}{R_p}. \tag{3.41}$$

This equation provides insight into how $R(\theta)$ varies based on $\Omega(r)$ in the external regions. If $d\Omega/dr < 0$ in the outer layers, this equation suggests that the actual oblateness of the star is slightly more pronounced than that inferred using the Ω value observed at the equator. Generally, in the outer stellar layers, the gradient $d\Omega/dr$ is relatively flat, making the discrepancy from the conventional Roche surface rather small. Consequently, this rationalizes the common practice of applying formulas for critical velocities derived for solid body rotation even when dealing with shellular rotation.

3.1.6   Meridional Circulation

Physically, meridional circulation arises because the equipotential surfaces, or levels, are closer together in the polar regions and more widely spaced in the equatorial regions due to the centrifugal force in rotating stars. This varying spacing directly impacts the radiative flux, which is proportional to the effective gravity and, consequently, to the distance between equipotential surfaces. This scenario leads to an excess flux along the polar axis

and a deficit near the equatorial plane, resulting in a thermal imbalance. This thermal imbalance triggers global circulation patterns to develop in the meridian plane (Fig. 3.5). However, we will focus on outlining the main characteristics and equations of this process without delving into the derivations. The velocity of meridional circulation is the primary
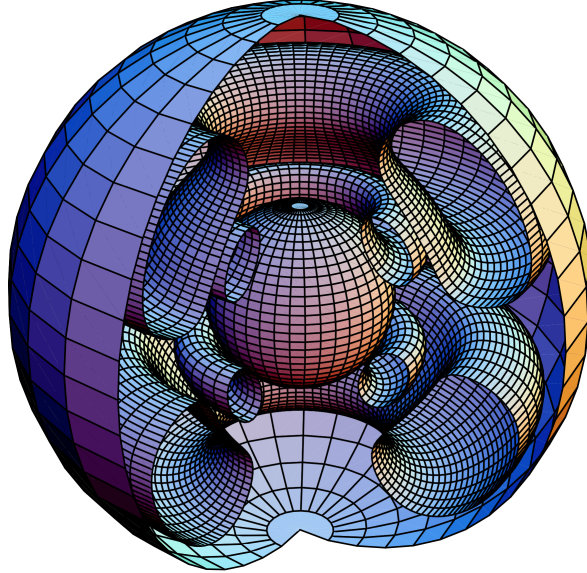
Figure 3.5: Stream lines of meridional circulation in a rotating 20 $M_\odot$ model with solar metallicity and $v_{ini} = 300$ km s^{-1} at the beginning of the H-burning phase. Taken from Meynet and Maeder 2002.

quantity characterizing this phenomenon, and it can be decomposed into two components: radial (U_r) and horizontal (U_θ). In cases of axial symmetry, such as shellular rotation, these components can be represented using spherical functions. For our discussion, we'll limit the expansion of the Legendre polynomials to the second order[5]:

$$\boldsymbol{U} = U_2(r)P_2(\cos\theta)\boldsymbol{e}_r + V_2(r)\frac{dP_2(\cos\theta)}{d\theta}\boldsymbol{e}_\theta, \tag{3.42}$$

Here, $U_2(r)$ represents the amplitude of the radial component of the meridional circulation velocity. Similarly, $V_2(r)$ denotes the amplitude of the horizontal component. Interestingly, these two parameters are linked by the condition:

$$\frac{1}{r}\frac{d}{dr}\left[\rho r^2 U_2(r)\right] - 6\rho V_2(r) = 0. \tag{3.43}$$

For our subsequent exploration of the vertical transport of angular momentum, our focus lies on its vertical component, given by $u(r,\theta) = U_2(r)P_2(\cos\theta)$, where $P_2(x)$ is the second Legendre polynomial.

---

[5]The reason we exclude zero-order polynomials is that P_0 is a constant, preventing the velocity from vanishing. Additionally, odd-order terms such as P_3, P_5, and so on, are not symmetric with respect to the equator, and thus, they are set to zero.

The formulation of the radial amplitude $U_2(r)$ was first established by Zahn 1992 and then the effects of horizontal turbulence, chemical gradients and non-stationarity were accounted for by Maeder and Zahn 1998:

$$U_2(r) = \frac{P}{\overline{\rho g} C_P \overline{T}} \frac{1}{[\nabla_{ad} - \nabla + (\phi/\delta)\nabla_\mu]} \cdot \left(\frac{L}{M_*} [E_\Omega + E_\mu] + \frac{C_P}{\delta} \frac{\partial \Theta}{\partial t} \right). \qquad (3.44)$$

This comprehensive expression captures the fundamental features of meridional circulation. Various quantities (P, $\overline{T}$, $\overline{\rho g}$, E_Ω, etc.) are evaluated at the specific level r. Overlined terms represent the average density over the considered isobar, reflecting values provided by equations of stellar structure for rotating stars. C_P stands for the specific heat at constant pressure, and ∇_{ad} refers to the adiabatic gradient. Furthermore, $M_* = M \left(1 - \frac{\Omega^2}{2\pi g \rho_m}\right)$, where ρ_m is the mean density inside the considered level surface and $\Theta = \tilde{\rho}/\overline{\rho}$ represents the ratio of density variation to the average density on an equipotential. Terms such as ϕ and δ are derived from the generic equation of state ($d\rho = \alpha \frac{dP}{P} + \phi \frac{d\mu}{\mu} - \delta \frac{dT}{T}$), while E_Ω^* and E_μ are components that dependent on $\Omega-$ and $\mu-$distributions, respectively and they have a quite long expression that is given in Appendix 7.1.
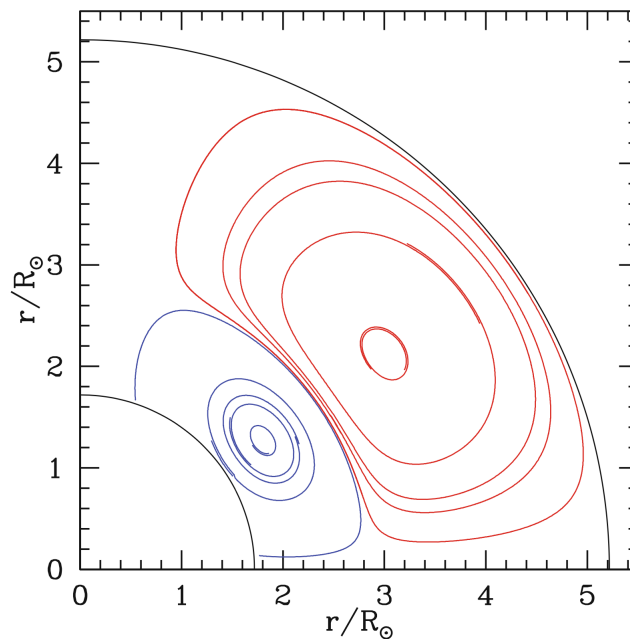
Figure 3.6: Circulation currents in a 20 M$_\odot$ star in the middle of the H-burning phase. The initial rotation velocity is 300 km/s. The inner loop is raising along the polar axis, while the outer loop, the Gratton–Öpik circulation cell, is going up in the equatorial plane. Taken from Maeder 2009.

A particularly significant term, ∇_μ in Eq. (3.44), originates from the vertical chemical gradient and the coupling between horizontal and vertical $\mu-$gradients, driven by horizon-

tal turbulence. The presence of ∇_μ may considerably reduce the amplitude $U_2(r)$, as it can be one or two orders of magnitude larger than $\nabla_{ad} - \nabla$ in certain layers. The horizontal component V_2 is defined by Eq. (3.43) at each level. A positive value of $U_2(r)$ indicates a positive velocity, signifying an upward current along the polar axis and an inward motion near the equatorial plane, as depicted by the inner loop in Fig. 3.6. As we approach the surface, the term $\overline{\Omega^2}/(2\pi G\overline{\rho})$ within E_Ω^*, reported in equation (7.1), becomes significant. This can potentially reverse circulation, a phenomenon initially recognized by Gratton 1945 and Öpik 1951. This reversal leads to the emergence of an outer circulation cell, referred to as the Gratton–Opik circulation cell, see Fig. 3.6. This outer cell rotates in the opposite direction and facilitates the outward transport of angular momentum. This circulation pattern significantly influences stellar evolution by enhancing surface rotation through angular momentum transport within the interior.

3.1.7   Shear Turbulence

Differential rotation gives rise to shear turbulence at the interfaces of layers with varying rotational velocities. Stability of a layer is maintained if the additional kinetic energy resulting from differential rotation doesn't overcome the buoyancy force, a criterion known as the *Richardson criterion*. Shear turbulence becomes prominent as thermal dissipation diminishes the buoyancy force. In this context, Maeder 1997 determined the coefficient of diffusion due to shear turbulence as:

$$D_{shear} = \frac{\overline{K}}{\frac{\phi}{\delta}\nabla_\mu + (\nabla_{ad} - \nabla_{rad})} \cdot \frac{H_p}{\overline{g}\delta} \left[f_{energ} \left(\frac{9\pi}{32}\overline{\Omega}\frac{d\ln\overline{\Omega}}{d\ln r} \right)^2 - (\nabla' - \nabla) \right]. \qquad (3.45)$$

Here, $K = \frac{4acT^3}{3\kappa\rho^2 C_P}$ represents the thermal diffusivity, while f_{energ} denotes the fraction of excess energy in the shear contributing to mixing here taken equal to 1. Additionally, $(\nabla' - \nabla)$ is the difference between the internal non-adiabatic gradient and the local gradient, which can often be neglected in most scenarios.

3.1.8   Horizontal Turbulence

Turbulent motions within a rotating star emerge due to the presence of differential rotation, which leads to shear instabilities between layers with varying velocities. This phenomenon results in the generation of turbulent flows. In stable radiative zones, the turbulence tends to be more pronounced in the horizontal direction compared to the vertical direction. This distinction arises because the stable thermal gradient and chemical gradient in the vertical direction exerts stronger opposing forces against fluid motions than in the horizontal direction. Specifically, the characteristics of horizontal turbulence

are captured by a coefficient known as horizontal kinematic viscosity, denoted as ν_h. Remarkably, this coefficient ν_h also serves as the coefficient D_h utilized to quantify horizontal diffusion of elements. The relationship between the diffusion coefficient and the viscosity arising from horizontal turbulence is described by Zahn 1992:

$$D_h \approx \nu_h = \frac{1}{c_h} r |2V_2(r) - \alpha U_2(r)|. \tag{3.46}$$

In the equation above, $U_2(r)$ is the vertical component of the meridional circulation velocity, while $V_2(r)$ represents the horizontal component. The constant c_h is dimensionless and typically around unity. Additionally, α is defined as $\alpha = \frac{1}{2} \frac{d \ln r^2 \overline{\Omega}}{d \ln r}$.

3.1.9 Transport of Angular Momentum

In the context of angular momentum transport, particularly for shellular rotation, the equation describing the transport of angular momentum in the vertical direction, expressed in Lagrangian coordinates, is given by Zahn 1992 and Maeder and Zahn 1998:

$$\overline{\rho} \frac{d}{dt} (r^2 \overline{\Omega})_{M(r)} = \frac{1}{5r^2} \frac{\partial}{\partial r} (\overline{\rho} r^4 \overline{\Omega} U_2(r)) + \frac{1}{r^2} \frac{\partial}{\partial r} (\overline{\rho} D r^4 \frac{\partial \overline{\Omega}}{\partial r}). \tag{3.47}$$

Here, $\overline{\rho}$ represents the mean density, and $\overline{\Omega}$ signifies the mean angular velocity on an isobar at the level r. This equation automatically accounts for the effects of expansion or contraction. Taking into consideration the detailed expression of $U_2(r)$ for meridional circulation (described in Sect. 3.1.6), which involves terms up to the third spatial derivative of $\Omega(r, t)$, Eq. (3.47) becomes a fourth-order equation, requiring careful numerical solutions. The term D in the equation stands for the total diffusion coefficient that encompasses various considered instabilities responsible for angular momentum transport, including convection, semiconvection, and shear turbulence. Notably, a substantial diffusion coefficient in convective regions implies a rotation law that closely resembles solid body rotation.

The transport of angular momentum due to circulation has often been modeled as a diffusion process (Endal and Sofia 1976; Pinsonneault et al. 1989; Heger et al. 2000). However, it is important to highlight the functional distinction between the terms involving U (advection) and D (diffusion) in Equation (3.47). Physically, advection and diffusion differ significantly: diffusion redistributes a quantity from regions of abundance to regions of scarcity, while advection doesn't necessarily adhere to this pattern. In fact, a circulation with a positive value of $U(r)$—indicating upward motion along the polar axis and downward motion at the equator—essentially results in an inward transport of angular momentum (as shown for example by the inner circulation cell in Fig. 3.6). Consequently, when this process is treated as a diffusion, particularly as a function of $\partial\Omega/\partial r$, the sign of the effect might be incorrectly predicted.

3.1.10 Mixing and Transport of Chemical Elements

An equation combining diffusion and advection, like Equation (3.47), should normally be used to describe the transport of chemical elements. However, in cases where the turbulent diffusion's horizontal component, represented by D_h in Equation (3.46), becomes substantial, the combined effects of the advective vertical transport of chemicals and the horizontal transport of chemicals by horizontal turbulence behave globally as a diffusive process, as discussed by Chaboyer and Zahn 1992, with an effective diffusion coefficient, denoted as D_{eff}. Fig. 3.7 visually illustrates this concept, elucidating the consequences of
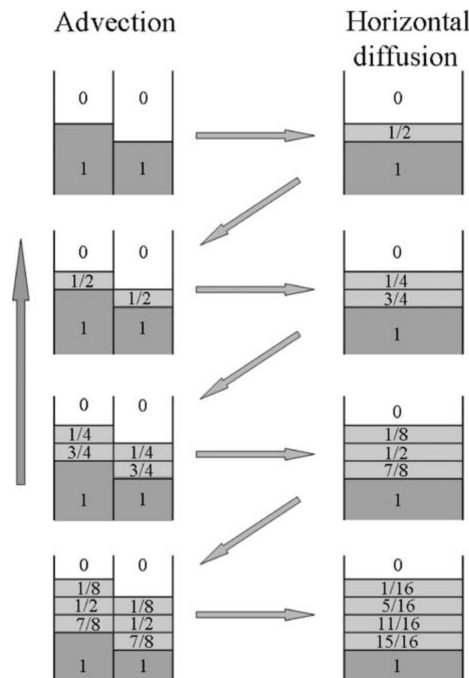
Figure 3.7: Schematic illustration of the combination of the effects of circulation and horizontal turbulence. The very left column is moving up, at each time step the horizontal turbulence mixes the layers. This makes a distribution like the error function, showing that the combination of both motions acts as a diffusion as far as the mixing of elements is concerned. Taken from Maeder 2009.

vertical movement and horizontal diffusion. Importantly, in line with Chaboyer and Zahn 1992, it's worth noting that this idea doesn't extend to the transfer of angular momentum. The formula for D_{eff} is expressed as:

$$D_{eff} = \frac{|rU(r)|^2}{30 D_h}. \tag{3.48}$$

Here, D_h represents the coefficient of horizontal turbulence, as defined in Equation (3.46).

In radiative zones, the primary mechanisms governing mixing are meridional circulation and shear-induced mixing. Therefore, the vertical movement of chemical elements fol-

lows a diffusion equation that not only includes macroscopic movement but also accounts for the impact of vertical turbulent transport. This diffusion equation is formulated as:

$$\rho \frac{d\overline{X}_i}{dt} = \frac{1}{r^2}\frac{\partial}{\partial r}\left(\rho r^2 (D_{mix})\frac{\partial \overline{X}_i}{\partial r}\right) + \left(\frac{d\overline{X}_i}{dt}\right)_{nuc}, \tag{3.49}$$

The second term on the right-hand side accounts for changes in composition due to nuclear reactions. The coefficient D_{mix} is the sum $D_{mix} = D_{shear} + D_{eff}$, with D_{eff} determined by Equation (3.48). The characteristic timeframe for the mixing of chemical species is therefore $t_{mix} \approx \frac{R^2}{D_{mix}}$.

3.1.11 Equations of Stellar Evolution with Rotation

Four equations govern the structural evolution of a star, and within the framework of shellular rotation, they can be expressed as follows (Meynet and Maeder 1997, Maeder 2009):

1. **Hydrostatic Equilibrium**:
$$\frac{\partial P}{\partial M_P} = -\frac{GM_P}{4\pi r_P^4}f_P. \tag{3.50}$$

2. **Continuity Equation**:
$$\frac{\partial r_P}{\partial M_P} = \frac{1}{4\pi r_P^2 \overline{\rho}}. \tag{3.51}$$

3. **Energy Conservation**:
$$\begin{aligned}\frac{\partial L_P}{\partial M_P} &= \epsilon_{nuc} - \epsilon_\nu + \epsilon_{grav} \\ &= \epsilon_{nuc} - \epsilon_\nu - c_P\frac{\partial T}{\partial t} + \frac{\delta}{\rho}\frac{\partial P}{\partial t}.\end{aligned} \tag{3.52}$$

4. **Energy Transport Equation**:
$$\frac{\partial \ln \overline{T}}{\partial M_P} = -\frac{GM_P}{4\pi r_P^4}f_P \min\left[\nabla_{ad}, \nabla_{rad}\frac{f_T}{f_P}\right]. \tag{3.53}$$

- *In convective zones (in the case of abiabatic convection, valid in deep stellar interiors):*
$$\nabla = \nabla_{ad} = \frac{P\delta}{\overline{T}\overline{\rho}c_P}. \tag{3.54}$$

- *In radiative zones:*
$$\nabla = \nabla_{rad} = \frac{3}{16\pi acG}\frac{\kappa L(P)P}{M_*(r)\overline{T}^4}. \tag{3.55}$$

Other variables are defined as:

$$f_P = \frac{4\pi r_P^4}{GM_P S_P} \frac{1}{\langle g_{eff}^{-1} \rangle}, \tag{3.56}$$

$$f_T = \left(\frac{4\pi r_P^2}{S_P} \right)^2 \frac{1}{\langle g_{eff} \rangle \langle g_{eff}^{-1} \rangle}. \tag{3.57}$$

Here, $\langle x \rangle$ represents the average of quantity x on an isobaric surface, while $\overline{x}$ represents the average of quantity x in the volume between two consecutive isobars. The index P pertains to the isobar with a pressure equal to P, and S_P is the surface area of that isobar. The rest of the variables maintain their conventional meanings. To solve these equations, the following physical aspects are essential:

- Nuclear reaction rates to evaluate ϵ_{nuc} and ϵ_ν.

- The equation of state to determine ρ and other relevant thermodynamic values.

- Opacities for calculating ∇_{rad}.

- A convection treatment for computing the convective flux.

Furthermore, the equations governing the transport of angular momentum and chemical element abundances must also be followed. When atomic diffusion is integrated into the stellar model, equations describing the change in chemical composition due to diffusion are necessary. The aforementioned developments enable the construction of equilibrium models for rotating stars in one dimension, which is particularly valuable for generating grids of evolutionary models for rotating stars. It's crucial to emphasize that, in general, the primary effects of rotation on evolution comes from internal chemical element mixing, angular momentum transport, and the increased mass loss observed in massive stars. These effects are explored in subsequent sections.

3.1.12 Interaction of Rotation and Radiation Effects

The total luminosity $L(\Omega)$ of a rotating star undergoes changes due to the alterations in structure as described by Equations (3.52)-(3.53)-(3.56)-(3.57). In general, the luminosity tends to decrease with rotation due to the expansion induced by rotation, leading to a slight cooling effect and an increase in opacity. Figure 3.8 provides an illustration of the typical variations of luminosity with rotational speed (ω). We can depict the luminosity variation with rotation using the following expression:

$$L(\omega) = L(0)(1 - b\omega^2) \tag{3.58}$$

For the stellar masses of 1, 3, 9, 20, and 60 $M_\odot$, the models shown in Figure 3.8 yield values of $b = 0.23$, 0.07, 0.065, 0.06, and 0.05 respectively.
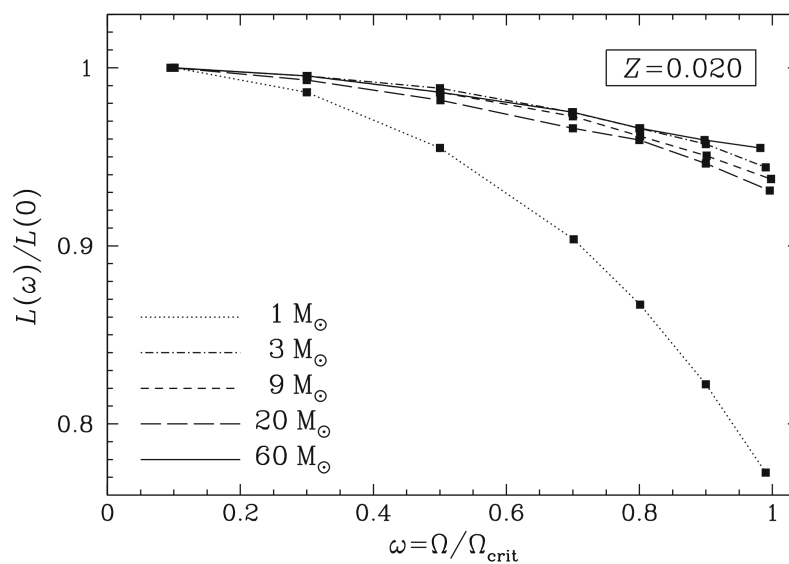
Figure 3.8: Relative variations of the total stellar luminosity for models of various masses on the ZAMS at $Z = 0.02$ as a function of the rotation parameter $\omega = \Omega/\Omega_{crit}$. Taken from Maeder 2009

.

Chapter 4

Rotating Models

The above developments allow us to construct equilibrium models of rotating stars in one dimension, which holds significant value when considering the generation of grids of evolutionary models for rotating stars. Disregarding the impact of rotation on the structural equations, even though it can serve as a reasonably good approximation in several instances, still overlooks a fundamental physical process that, in other cases, can exert a significant influence on the properties of stars.

For this study, we will utilize two stellar evolution codes, namely GENEC (Eggenberger et al. 2008) and MESA (Paxton et al. 2011, Paxton et al. 2013, Paxton et al. 2015, Paxton et al. 2018, Paxton et al. 2019). However, it is important to note that MESA's treatment of rotational effects differs notably from that of GENEC, particularly regarding the equation governing angular momentum transport. In MESA, angular momentum transport is primarily addressed as a diffusive process, as described in Heger et al. 2000, leading to substantial differences in the efficiency of rotational mixing. When considering fixed stellar masses, the Geneva rotating models exhibit higher temperatures and luminosities at the Terminal Age Main Sequence (TAMS) with respect to MESA rotating models. This implies that rotational mixing is more efficient in Geneva models compared to that in MESA models. For a more comprehensive discussion of these differences, refer to Choi et al. 2016. As discussed in detail in the following sections, efficient rotational mixing gives rise to hotter temperatures and higher luminosities due to larger core sizes and increased μ in the envelope.

The MIST project (Choi et al. 2016) computed comprehensive set of stellar evolutionary tracks and isochrones using MESA including rotation. Notably, the default rotating model in MIST experiences only a moderate extension in the Main Sequence (MS) lifespan. In contrast, the GENEC model, with the same rotation, demonstrates an approximate $\approx 25\%$ increase in the MS lifespan for stars exceeding 2 M$_\odot$. Current observations are not uniquely constraining, so we still do not have the possibility to rule out a treatment in favour of another one.

4.1 Reference Rotating Models

For the rest of this work, we will use GENEC models as our reference rotating models, as we believe their advecto-diffusive treatment of rotation, due to all the previously discussed reasons, better captures the nature of the physical process. In particular, we chose to compute models using the prescriptions from the grid presented in Georgy et al. 2013. This grid incorporates rotation using the advecto-diffusive treatment and covers the mass range of 2RC stars, although with limited resolution. Additionally, it spans the interval of $0.0 \leq \Omega_{ini}/\Omega_{crit} \leq 0.95$ with good resolution and, most importantly, the efficiency of rotational mixing is calibrated to reproduce the typical chemical enrichments observed at the surface of solar-metallicity MS stars for a typical initial rotation velocity. Here we will summarize, and in some cases describe in more detail, only the properties of these models that are relevant for our discussion and we refer to Georgy et al. 2013 for additional informations.

- The grid of models contains ten different masses: 1.7, 2.0, 2.5, 3.0, 4.0, 5.0, 7.0, 9.0, 12.0 and 15.0 M$_\odot$.

- Nine different initial rotation rates: $\Omega_{ini}/\Omega_{crit} = 0.0, 0.1, 0.3, 0.5, 0.6, 0.7, 0.8, 0.9, 0.95$.

- Three different metallicities: $Z = 0.014$ (solar metallicity), $Z = 0.006$ (Large Magellanic Cloud metallicity) and $Z = 0.002$ (Small Magellanic Cloud metallicity).

- The models are evolved up to the helium flash ($M_{ini} \leq 2$ M$_\odot$), the early asymptotic giant branch (2.5 M$_\odot \leq M_{ini} \leq 9$ M$_\odot$) or the end of central carbon burning ($M_{ini} \geq 9$ M$_\odot$).

- The initial abundances of H, He, and metals are set to $X = 0.720$, $Y = 0.266$, and $Z = 0.014$, obtained by calibrating a 1 M$_\odot$ model.

- The mixture of heavy elements is assumed to be that of Asplund et al. 2005 except for the Ne abundance, which is taken from Cunha et al. 2006.

- The convective zones are determined with the Schwarzschild criterion. For the H- and He-burning phases, the convective core is extended with an overshoot parameter $d_{ovsh}/H_p = 0.10$ from 1.7 M$_\odot$ and above.

- The value of the overshoot parameter was calibrated in the mass domain $1.35 - 9$ M$_\odot$ to ensure that the rotating models closely reproduce the observed width of the MS band when the same mean initial velocity on the ZAMS of $v_{ini}/v_{crit} = 0.4$ is used for the different masses.

- The outer convective zone is treated according to the mixing length theory, with a solar calibrated value for the mixing-length parameter of the low-mass stars ($\alpha_{MLT} \equiv l/H_p = 1.6467$). For more massive stars, i.e. for stars with $M > 1.25$ M$_\odot$, the difference in the EOS implies a slightly lower value for this parameter: $\alpha_{MLT} = 1.6$.

- Rotation and rotational mixig are implemented as already discussed above. The efficiency of the mixing (the f_{energ} factor in Eq. (3.45)) was calibrated to reproduce typical chemical enrichments at the surface of solar-metallicity MS B-type stars for a typical initial rotation velocity.

4.1.1 Mixing Efficiency

In Figure 4.1, we present the profiles of the diffusion coefficients that are responsible for the transport of chemical species. This includes the effective diffusion coefficient D_{eff} which considers the combined effects of meridional circulation and strong horizontal turbulence, the shear-mixing diffusion coefficient D_{shear}, and the total diffusion coefficient $D_{mix} = D + D_{eff}$ (with $D = D_{conv} + D_{shear}$). These profiles are depicted around the midpoint of the MS phase ($X_{H,c} = 0.3$) for a 2.5 M$_\odot$ model with an initial rotation rate of $\Omega_{ini}/\Omega_{crit} = 0.5$. We can see that except near the edge of the convective core, where D_{eff}
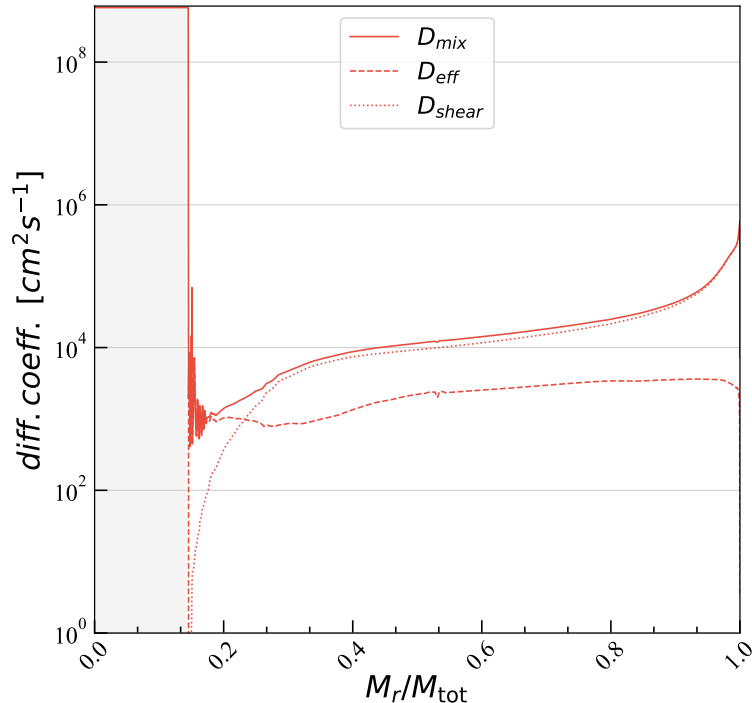
Figure 4.1: Profiles of the diffusion coefficients D_{mix}, D_{eff} and D_{shear} at roughly the middle of the MS phase ($X_{H,c} = 0.3$) for a 2.5 M$_\odot$ model with an initial rotation rate $\Omega_{ini}/\Omega_{crit} = 0.5$. The gray-shaded area is the convective core.

dominates, shear mixing predominantly contributes to the transport of chemical species in the majority of the radiative envelope. There's a distinct trend when comparing different initial masses with the same initial rotation rate $(\Omega_{ini}/\Omega_{crit})$ and the same metallicity (Z). Both D_{eff} and D_{shear} exhibit higher values for greater initial masses, as illustrated in Figure 4.2. Conversely, as highlighted in Georgy et al. 2013, the coefficients show
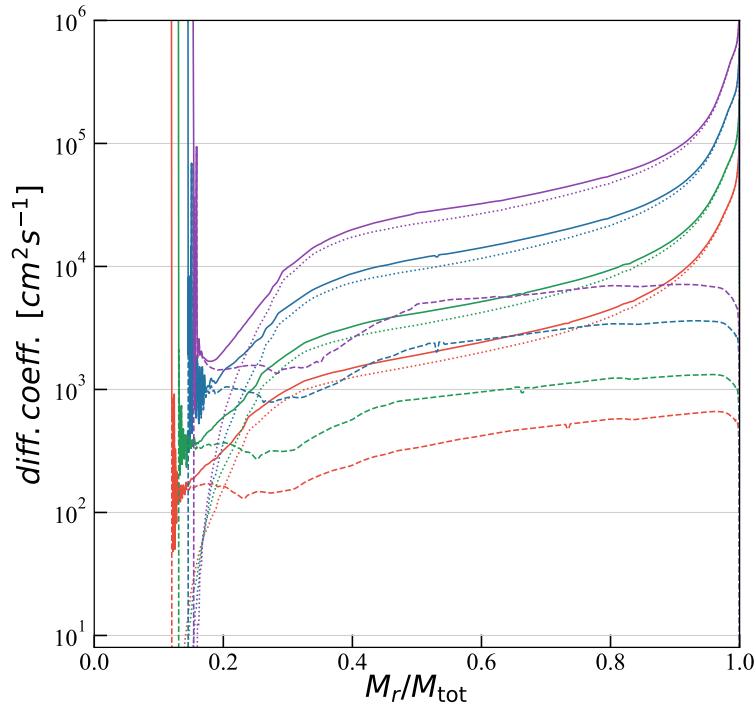
Figure 4.2: Profiles of the diffusion coefficients D_{mix} (solid), D_{eff} (dashed) and D_{shear} (dotted) of a 1.7 M$_\odot$ (red), 2.0 M$_\odot$ (green), 2.5 M$_\odot$ (blue), 3.0 M$_\odot$ (violet) models at roughly the middle of the MS phase $(X_{H,c} = 0.3)$ for $\Omega_{ini}/\Omega_{crit}$=0.5.

negligible variations concerning metallicity. However, owing to lower opacities at lower metallicities, stars with lower Z values are more compact. This leads to shorter timescales for diffusion $(\tau_{diff} \approx R^2/D)$ and consequently more efficient surface enrichment.

Another trend emerges when comparing models with different initial rotation rates $(\Omega_{ini}/\Omega_{crit})$ while maintaining a fixed mass and metallicity. On average, both D_{shear} and D_{eff} tend to be higher for higher initial rotation rates. Although D_{eff} displays a notably slower rate of increase compared to D_{shear}, the rise tends to slow down for higher $\Omega_{ini}/\Omega_{crit}$ values. In some cases, for the fastest rotators (0.8, 0.9, 0.95 $\Omega_{ini}/\Omega_{crit}$), the increase can even reverse, as shown in Figure 4.3. Furthermore, the mixing efficiency isn't uniform throughout the MS phase; it intensifies with lower $X_{H,c}$ values. Lower $X_{H,c}$ leads to higher values for both D_{shear} and D_{eff}, as demonstrated in Figure 4.4. One crucial observation that will come in handy later when parameterizing the diffusion coefficient profiles for MESA models is that despite the intricate behavior of these profiles - often showing spikes
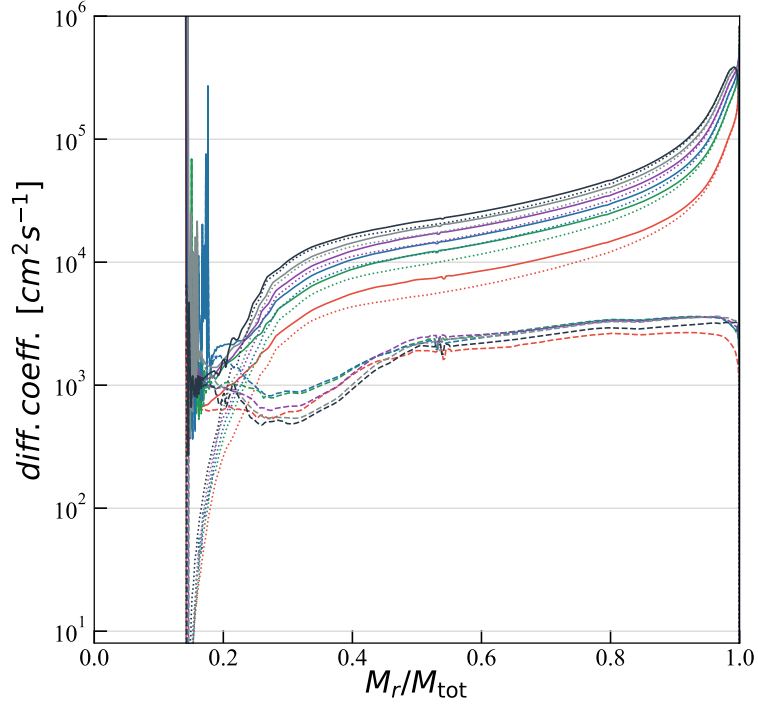
Figure 4.3: Profiles of the diffusion coefficients D_{mix} (solid), D_{eff} (dashed) and D_{shear} (dotted) of 2.5 $M_\odot$ models at roughly the middle of the MS phase ($X_{H,c} = 0.3$) for 0.3, 0.5, 0.6, 0.7, 0.8, 0.9 $\Omega_{ini}/\Omega_{crit}$. 0.1, 0.95 $\Omega_{ini}/\Omega_{crit}$ are not plotted for a cleaner visualization, but they follow the same trend.

and irregularities as seen in Figure 4.4 - their overall shape tends to remain consistent on average, resembling the pattern shown in Figure 4.1. These deviations are transient and short-lived during MS evolution.

In the post-MS phases preceding the QCHeB phase, the evolution is several orders of magnitudes faster, while the values of D_{mix} remains of the same order, or even decrease due to the slowdown of rotation, see Fig. 4.10. This means that $\tau_{PoMS} << \tau_{diff}$ ($\tau_{diff} \approx R^2/D_{mix}$), so rotational mixing is practically negligible during these phases. During the QCHeB phase, the star's evolution slows down again, requiring a closer examination of how τ_{QCHeB} compares to τ_{diff}. As illustrated in Figure 4.10, during this phase, only the core experiences rotation while the envelope's rotation is negligible. Consequently, we shouldn't expect substantial rotational mixing in the envelope. Furthermore, Any shear mixing that could be expected at the core's boundary, where strong differential rotation is present, is inhibited by the steep chemical gradient ∇_μ at the same location, as depicted in Figure 4.5b and detailed in Section 3.1. As a result of these considerations, the influence of rotational mixing becomes substantial primarily throughout the MS phase. The impact of MS rotational mixing is clearly evident in Figure 4.5a. The μ profile of the non-rotating model exhibits a steep decline and a sharp change of slope at the boundary of the Helium
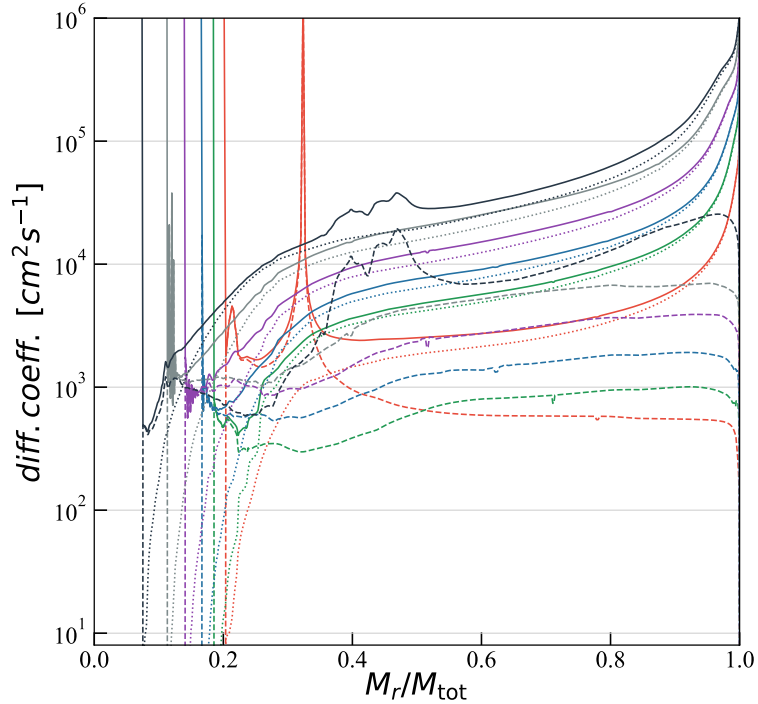
Figure 4.4: Profiles of the diffusion coefficients D_{mix} (solid), D_{eff} (dashed) and D_{shear} (dotted) of a 2.5 $M_\odot$ model with an initial rotation rate of 0.5 $\Omega_{ini}/\Omega_{crit}$ at different stages during the MS: $X_{H,c} = 0.67$ (red), 0.54 (green), 0.41 (blue), 0.27 (violet), 0.14 (gray), 0.01 (black).

core, generated by the receding convective core. In contrast, in the rotating models, we observe that the sharp μ profile at the Helium core boundary is smoothed by the rotational mixing near the core and further diffused outward by the extended diffusion coefficient profile. This effect grows progressively with $\Omega_{ini}/\Omega_{crit}$ until approximately $\Omega_{ini}/\Omega_{crit} \approx 0.5$, beyond which it remains relatively unchanged. For $\Omega_{ini}/\Omega_{crit} > 0.5$, the primary difference lies in the increased efficiency of envelope mixing, while the near-core mixing remains roughly constant. This leads to a slight decrease in μ nearer to the core and an increase further in the envelope.

These rotational mixing effects at the TAMS stage bear consequences on the properties of initial QCHeB models. As shown in Figure 4.6b, a prominent outcome is that the constant envelope μ value increases with larger $\Omega_{ini}/\Omega_{crit}$ until it tends to saturate around $\Omega_{ini}/\Omega_{crit} \approx 0.5$. This arises from the fact that as the convective envelope progressively penetrates deeper during post-MS phases, in rotating models, it mixes regions with higher $\overline{\mu}$ (average mean molecular weight). Additionally, an effect can be observed on the size of the Helium core. This influence on Helium core size is critical for the characteristics of the secondary clump, a point that will be discussed in depth later, along with the results of the complete model grid. The effects of rotational mixing are also discernible in the smoothness of the chemical abundance profiles near the Helium core at TAMS, as

(a)

(b)
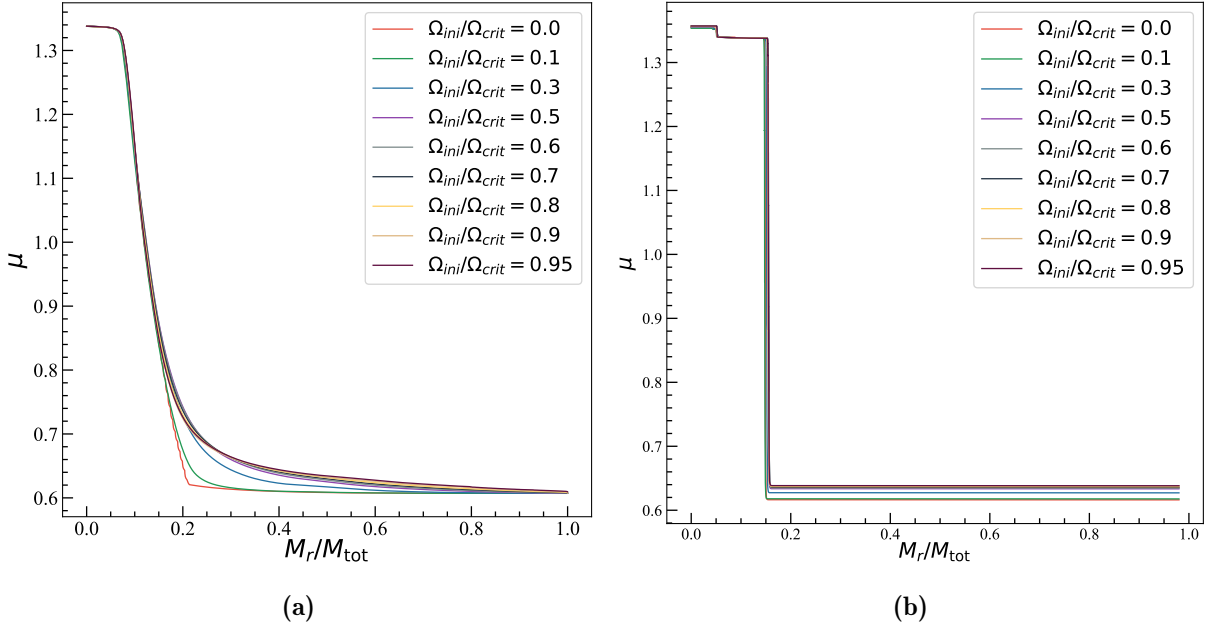
Figure 4.5: Mean molecular weight profiles at TAMS (a) and at initial QCHeB (b) for 2.5 M$_\odot$ models for 0.0, 0.1, 0.3, 0.5, 0.6, 0.7, 0.8, 0.9, 0.95 $\Omega_{ini}/\Omega_{crit}$.

shown in Fig. 4.6a for a 2.5 M$_\odot$ model with $\Omega_{ini}/\Omega_{crit} = 0.5$ with respect to the non rotating model shown in Fig. 4.7a. It is important to note that the observed behaviors of the diffusion coefficient profiles described in this section remain consistent across all the `GENEC` models explored in this study.

4.1.2   HRD and Lifetimes

The effect of the centrifugal force governs the position of stars on, or near, the ZAMS: rotating models behave similarly to lower-mass ones, leading to shifts in their tracks towards lower values of both luminosity (L) and effective temperature (T_{eff}). This shift arises from a combination of atmospheric distortions and a reduction in effective gravity, as discussed in Section 3.1.12 and by Kippenhahn and Thomas 1970. This behavior is evident in the downward shift of ZAMS models in Figure 4.11.

As stellar evolution progresses, rotational mixing introduces fresh hydrogen into the core, thereby slowing down the convective core's mass decrease. Furthermore, newly generated helium is transported into the radiative zone, causing the model to evolve along a bluer and more luminous track. In Figure 4.11, it is evident that the luminosity achieved at the end of the MS, and consequently during the SGB, increases with the rotation rate up to approximately $\Omega_{ini}/\Omega_{crit} \approx 0.6$. Beyond this threshold, the luminosity either stabilizes or even decreases, a trend also apparent in the HRD-crossing luminosity. This behavior is directly related to the size of the convective core, which has a decisive
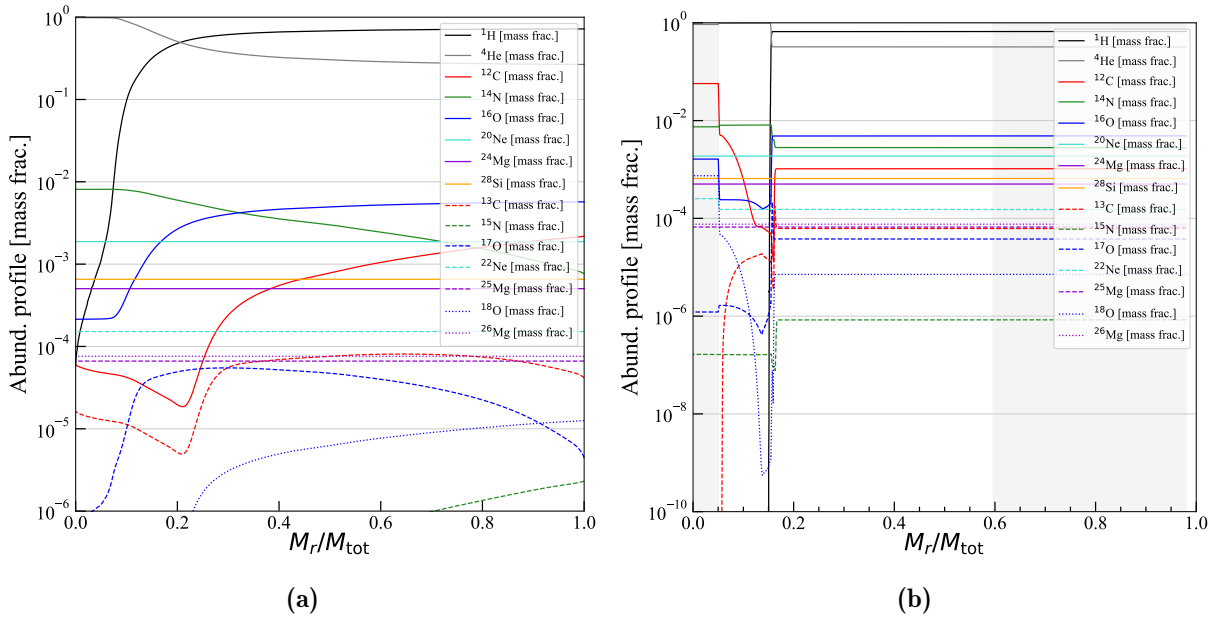
Figure 4.6: Chemical abundances profiles at TAMS (a) and at initial QCHeB (b) for a 2.5 $M_\odot$ model for a 2.5 $M_\odot$ model with 0.5 $\Omega_{ini}/\Omega_{crit}$.

influence on the luminosity at the MS end. The evolution of the convective core size during the MS is governed by two opposing physical processes associated with rotation. Firstly, rotation introduces additional support against gravity due to the centrifugal force, which works to reduce the core's size and luminosity. The explanation for this effect will be elaborated upon in the subsequent paragraph. Secondly, rotational mixing near the core's periphery progressively introduces fresh material into the core, increasing its mass and, consequently, its luminosity. Both of these effects contribute to the non-monotonic behavior of luminosity at the HRD crossing with respect to the initial rotation rate. As depicted in Figure 4.8, rotational mixing extends the duration of the MS phase. For the considered mass range and under solar metallicity conditions, this extension remains relatively consistent across various initial masses. The increase amounts to approximately 15-25% for initial rotation rates of 0.3 and 0.5 times Ω_{crit}. For the fastest rotating stars, this enhancement can reach values as high as 30-35%. Notably, the sensitivity of the 1.7 $M_\odot$ and 2.0 $M_\odot$ models is amplified due to their central temperature at the onset of core hydrogen burning lying around $20 \cdot 10^6$ K. This temperature range corresponds to the regime in which CNO-burning begins to dominate the pp-chain as the primary energy production channel. High rotation rates cause the hydrostatic effects of rotation to lower the central temperature, favoring the dominance of the pp-chain in energy production. This leads to a smaller convective core during the initial part of the MS phase. As evolution continues and central temperature rises, the convective core expands, reaching sizes even greater than those observed in non-rotating models at the beginning of core

(a)

(b)
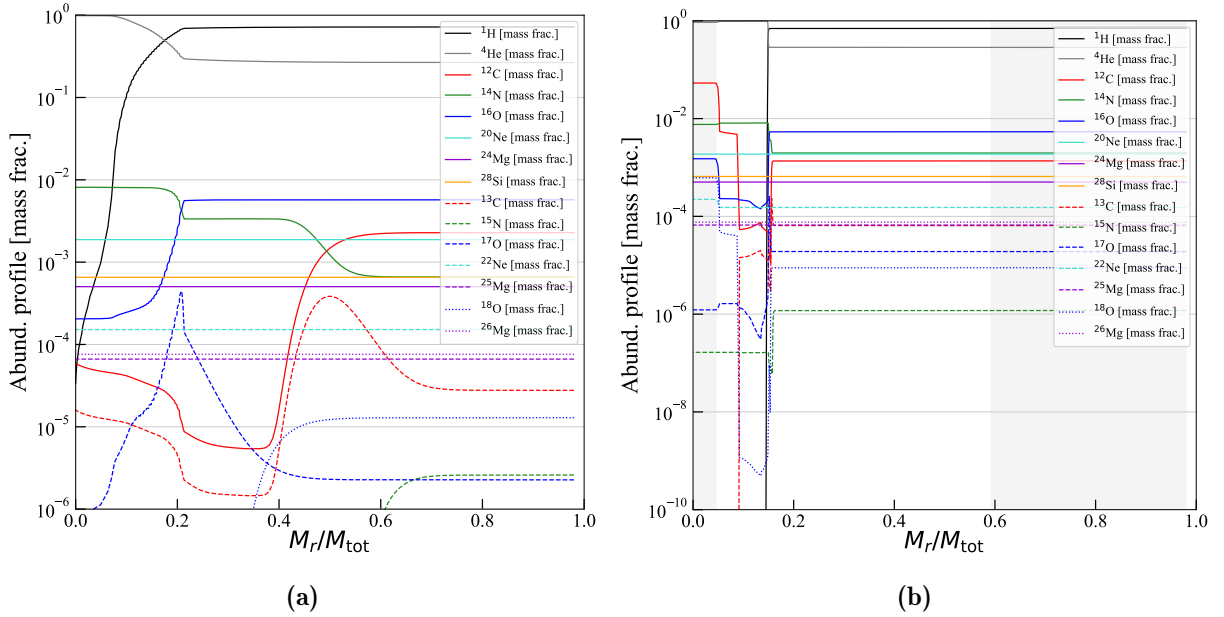
Figure 4.7: Chemical abundances profiles at TAMS (a) and at initial QCHeB (b) for a 2.5 $M_\odot$ model for a non-rotating 2.5 $M_\odot$.

hydrogen burning.

It is important to highlight that, as demonstrated in Georgy et al. 2013, within the low-mass range of the considered grid, changes in metallicity exert a more substantial impact on MS lifetimes than variations in initial velocity. This discrepancy arises from the reduced efficiency of rotational mixing in low-mass stars (as seen in Figure 4.13), coupled with the fact that changes in opacity resulting from alterations in chemical composition have a more pronounced effect at lower masses[1].

4.1.3 Core Mass vs. Rotation

As mentioned earlier, the added support against gravity due to rotation leads to lower central temperatures for higher initial velocities. Consequently, the size of the convective core on the ZAMS diminishes with increasing initial rotation velocity. However, as stellar evolution progresses, the more efficient mixing within more rapidly rotating stars serves to enlarge their convective cores, see Fig. 4.9a and 4.9b. This effect becomes particularly evident at the end of the MS phase, where the convective core's size is directly proportional to the star's initial rotation rate.

---

[1]The opacity in the temperature range of the massive stars is dominated by electron scattering, which is only marginally affected by a change in the chemical composition.
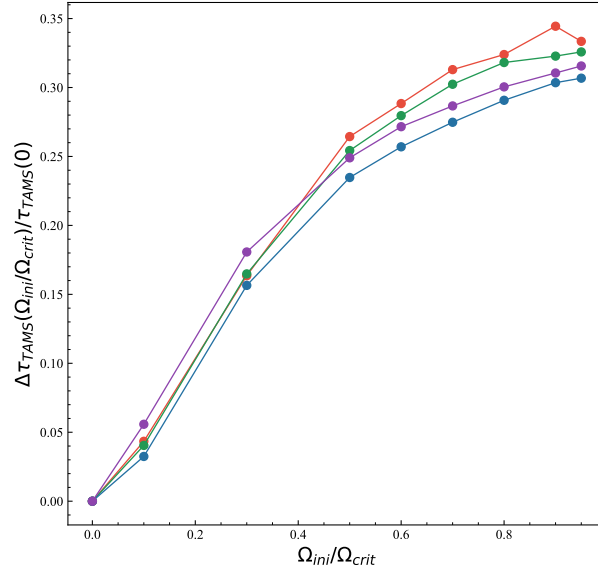
Figure 4.8: MS duration enhancement as a function of the initial rotation rate for 1.7 $M_\odot$ (red), 2.0 $M_\odot$ (green), 2.5 $M_\odot$ (blue), 3.0 $M_\odot$ (violet) models.

(a)

(b)
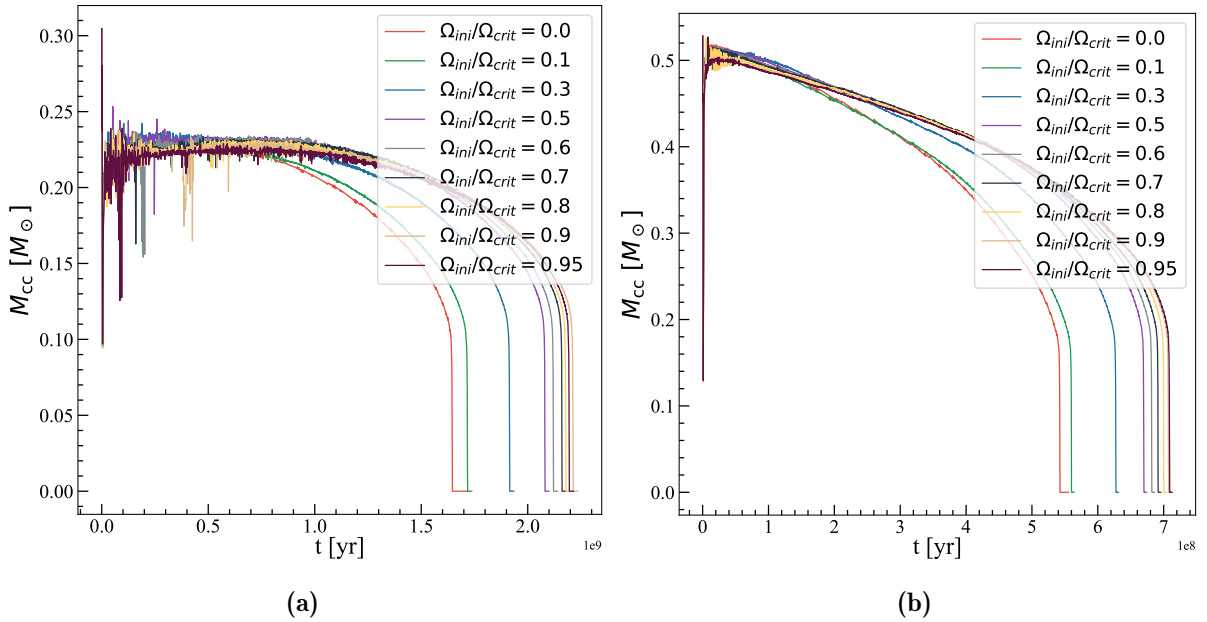
Figure 4.9: Evolution of the mass of the convective core M_{cc} during the MS for a 1.7 $M_\odot$ (a) and a 2.5 $M_\odot$ (b) model.
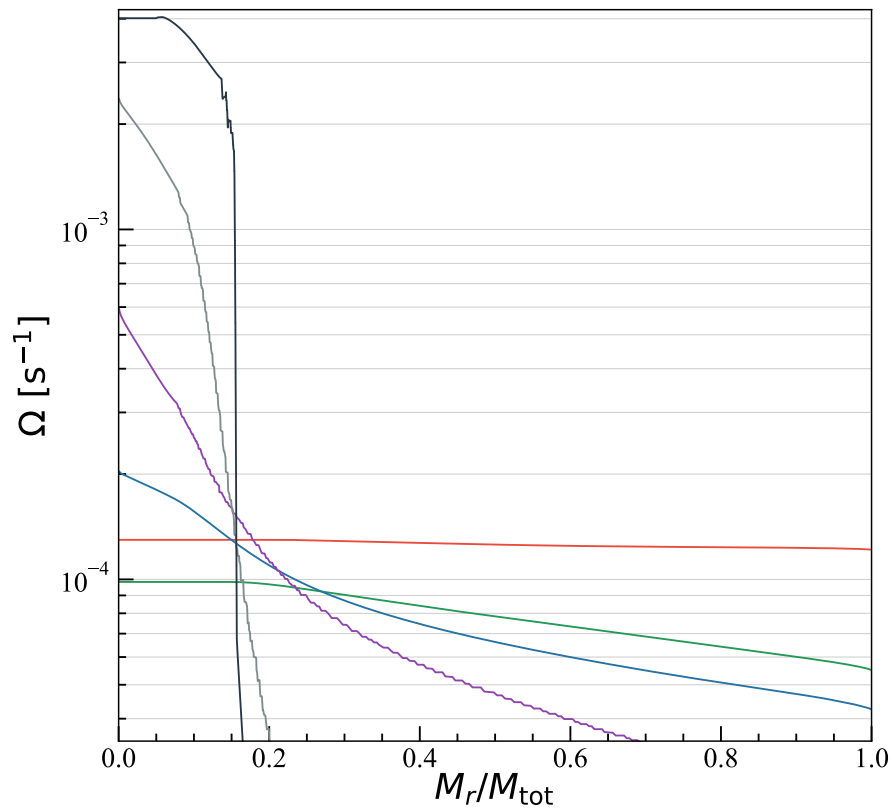
Figure 4.10: Angular velocity profiles of a 2.5 M$_\odot$ model with $\Omega_{ini}/\Omega_{crit}$ at ZAMS (red), middle of the MS phase with $X_{H,c} = 0.3$ (green), TAMS (blue), HRD crossing (violet), bottom of the RGB (gray) and initial QCHeB (black) phases.
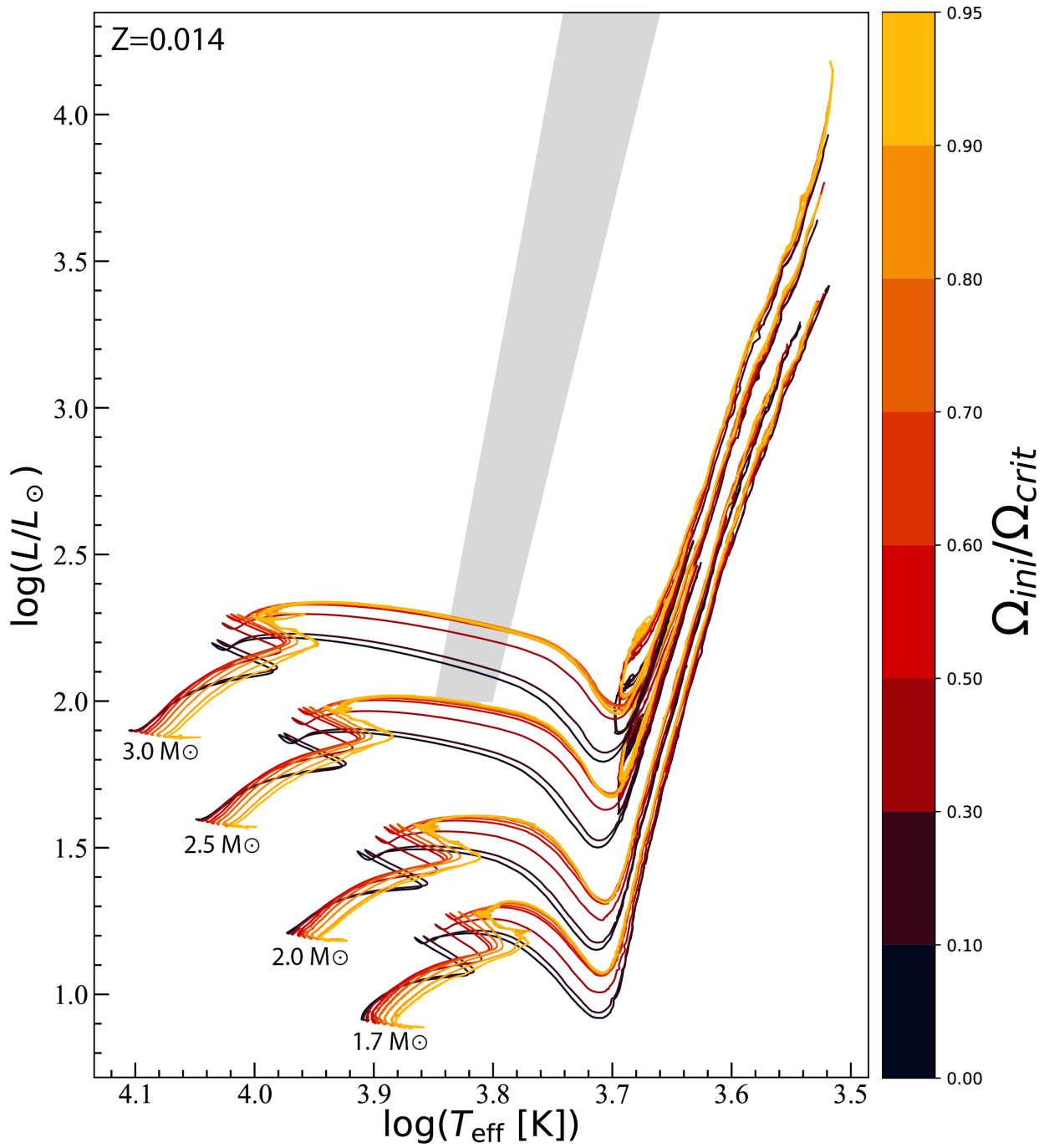
Figure 4.11: Evolutionary tracks of the `GENEC` reference models from the grid presented in Georgy et al. 2013. The gray shaded area represents the Cepheid instability strip.

4.1.4   Evolution of the Surface and Internal Rotation

As discussed extensively in previous research by Heger et al. 2000, pre-main-sequence (PMS) stars achieve rigid rotation due to convection. Therefore, models are initialized at the ZAMS with the assumption of solid body rotation, a simplification that is later relaxed as the star evolves. When differential rotation is permitted, the star's angular velocity profile undergoes an adjustment (depicted in Fig. 4.10) to reach a quasi-equilibrium state. The initial uniform angular velocity profile is not in equilibrium due to the influence of meridional circulation. This explains the swift decline in equatorial velocity at the early stages of evolution, as depicted in Fig. 4.12a.

Once the equilibrium profile is reached, the angular velocity within the star (and with it the equatorial velocity) varies as a function of time because of three main physical processes:

- Local conservation of angular momentum, which alters angular velocity during contractions or expansions of the star.

- Internal transport mechanisms that redistribute angular momentum throughout the stellar structure.

- Stellar winds that remove angular momentum from the stellar surface.

During the MS phase, these models develop an external meridional circulation cell known as the Gratton-Öpik cell (described in Section 3.1.6). This circulation pattern transfers angular momentum from the inner regions of the star to its surface, causing acceleration. The efficiency of the meridional circulation is greater for higher masses, for higher initial rotation rates and for higher metallicity. In contrast, the stellar mass loss due to radiative winds tends to brake the stellar surface. Similar to the meridional circulation, stellar wind strength increases with higher masses, initial rotation rates, and greater metallicity.

These opposing effects influence the evolution of the stellar surface velocity. In stars with low to intermediate masses, the transport mechanisms are relatively inefficient. Simultaneously, mass loss is either absent or minimal, especially during the MS phase. Consequently, these stars experience nearly constant equatorial velocities, as illustrated in Fig. 4.12a. However, according to the relation in Eq. (3.18), the critical velocity v_{crit} decreases throughout the MS phase due to the increasing radius R_{eq}. Consequently, the ratio v_{eq}/v_{crit} rises, as demonstrated in Fig. 4.12b. After the MS, in these models, the evolution of the angular velocity within the star is essentially governed by the local conservation of angular momentum. The envelope expands significantly during the HRD crossing and the RGB slowing down its rotation, while the core is slowly contracting and therefore increasing its rotation. This explains the post MS profiles in Fig. 4.10 in which the core tends to rotate much faster than the envelope.

(a)   **(b)**
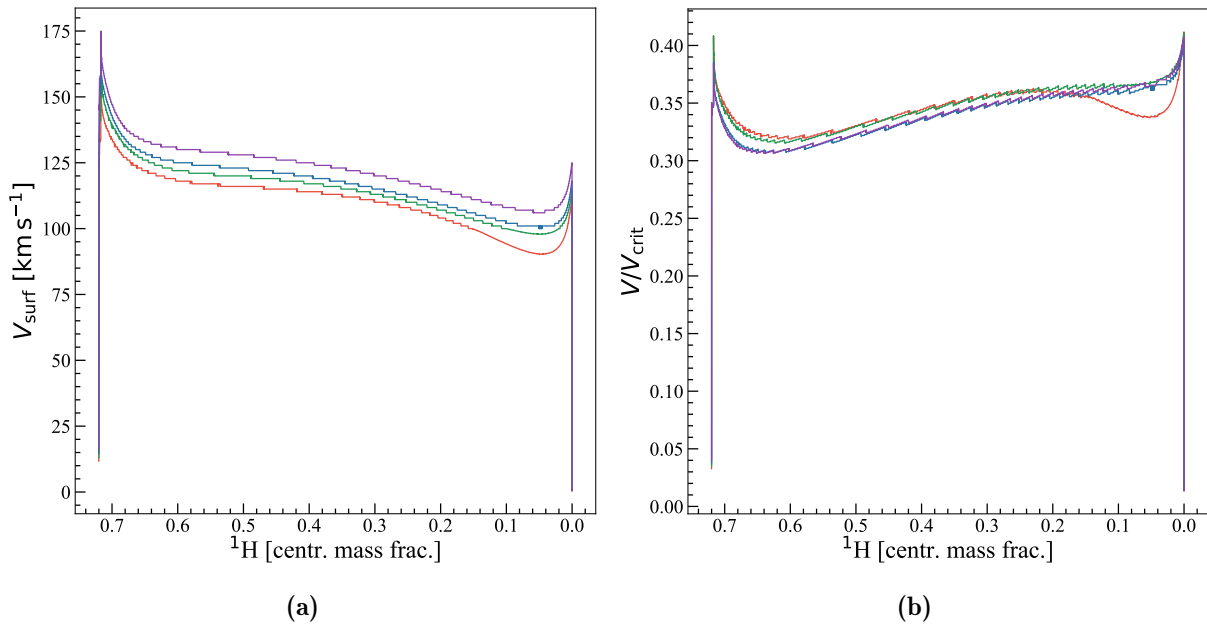
Figure 4.12: Evolution of rotation on the MS as a function of the central mass fraction of hydrogen for models with $\Omega_{ini}/\Omega_{crit} = 0.5$ and masses of 1.7 $M_\odot$ (red), 2.0 $M_\odot$ (green), 2.5 $M_\odot$ (blue), 3.0 $M_\odot$ (violet). *Left*: evolution of the equatorial velocity v_{eq}. *Right*: evolution of the v_{eq}/v_{crit} ratio.

Observations suggest that this picture is not complete, in fact some additional angular momentum transport is missing during these evolutionary phases (see Section 4.2). However, as already pointed out, the properties of 2RC stars that we are interested in are mainly affected on what happens during the MS, where despite some indications of an additional angular momentum transport mechanism also in this phase, there are also indications of differential rotation (see Section 4.2), preserving the significance of these models for this application.

4.1.5   Surface Abundances

The variations in the surface abundances at the end of the MS are shown in Fig. 4.13. We see that for a given $\Omega_{ini}/\Omega_{crit}$, the enrichment is stronger for higher masses. In Fig. 4.13 the shadowed area corresponds to a variation of 0.02 dex with respect to the initial N/H ratio (corresponding roughly to the typical error bars in the APOGEE DR17). The models evolving out of this area will therefore have a strong enough enrichment to be observable.
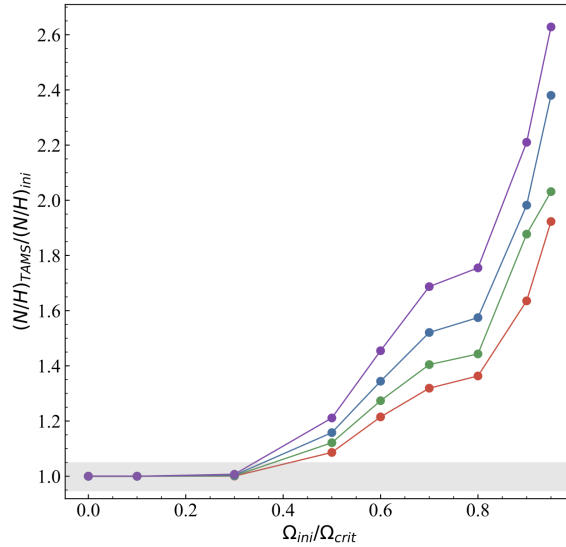
Figure 4.13: N/H ratio relative surface abundance at TAMS as a function of rotation for 1.7 $M_\odot$ (red), 2.0 $M_\odot$ (green), 2.5 $M_\odot$ (blue), 3.0 $M_\odot$ (violet) models. /The gray shaded area corresponds to the typical uncertainty in APOGEE DR17 of 0.02 dex.

4.2 Magnetic Fields

In the reference models chosen for this work neither a dynamo mechanism in the stellar interior, nor any strong fossil field that would impose solid body rotation is accounted for. We know today that stellar models including only hydrodynamical processes fail to reproduce the angular velocity of stellar cores in different evolutionary phases (e.g Eggenberger et al. 2012). In particular, the cores of stellar models on the lower RGB rotate too fast by up to three orders of magnitude compared to expectations based on asteroseismic constraints. This indicates that at least one efficient additional AM transport process must be at work in the interior of evolved stars, similarly to what is found for the Sun (Eggenberger et al. 2019) or for the rotation rates of compact objects (Suijs et al. 2008). Helioseismic measurements show that an efficient mechanism for angular momentum transport in radiative zones is needed in addition to the transport of angular momentum by meridional currents and the shear instability. Similar results are found for solar-type stars (Eggenberger 2019). As shown by Bétrisey et al. 2023, in general for MS stars in the colder part of the HR diagram (masses typically below $\approx$ 1.2 $M_\odot$ at solar metallicity) observations suggest a clear disagreement between the rotational properties of models that only includes hydrodynamic processes and asteroseismic constraints, while models with magnetic fields correctly reproduce the observations, similarly to the solar case. For MS stars in the hotter part of the HR diagram (masses typically above $\approx$ 1.2 $M_\odot$ at solar metallicity), models with hydrodynamic transport processes alone, and models with additional transport by magnetic instabilities are found to be consistent with

measurements. For these stars, the combination of asteroseismic constraints and of the surface rotation rate does not allow to conclude that an efficient AM transport is required in addition to the transport by meridional circulation and shear instability alone (Bétrisey et al. 2023).

It is evident that we still do not have a clear picture about the transport of AM and internal rotation in stars both during MS and post MS phases. Especially it is not clear wether these additional AM transport mechanisms, for which magnetic fields are cosidered among the best candidates, are needed and how important they are during the MS phase in the mass range considered in this work. The main reasons for introducing the effects of internal magnetic fields is that they would ensure an additional efficient transport of angular momentum. We choose to not consider the effects of magnetic fields in this work because, as discussed above, the present knowledge of these processes is still far from being well established and it is currently a very active topic of research, and despite GENEC models including these effects already exists (e.g. Moyano et al. 2023), due to the early stage of this research topic, an extended and homogeneous grid of models with internal magnetic fields and rotational mixing calibrated to reproduce the observed chemical enrichment is still not available. Indeed, an efficient transport of angular momentum in radiative zones results in a very low degree of radial differential rotation, which implies an inefficient transport of chemicals by the shear instabilitiy. However, due to the additional efficient transport of angular momentum related to magnetic fields, the transport of chemicals by the meridional circulation is increased when magnetic effects are accounted for. This implies that the internal transport of chemicals can still be efficient in fast rotating stars, despite the approximately flat rotation profile imposed by magnetic fields. In the case of slowly rotating stars, the situation is different, since both the transport of chemicals by the shear instability and meridional currents are inefficient when magnetic fields are taken into account. This is typically the case of solar-type stars with an extended convective envelope, for which the strong braking of the surface by magnetized winds results in surface velocities that rapidly decrease during the first part of their evolution on the main sequence (see Eggenberger et al. 2010 and Eggenberger 2019).

Chapter 5

Effect of Rotation-Induced Mixing of Chemicals on Secondary-Clump Stars

In this chapter, we'll build upon the ideas discussed in the previous chapter to develop methods for studying how the rotation-induced mixing of chemicals affects the observable properties of secondary clump stars. These secondary clump stars, often referred to as 2RC stars, represent a transitional phase between low- and intermediate-mass stars. These stars go through a different evolution determined by the degree of degeneracy of the environment in which helium begins to burn in their cores. It is crucial to analyze the entire range of masses around this transition in order to properly probe the change in the characteristics of their evolution. As highlighted by Girardi 1999, to accurately characterize this group of stars, it is important to compute stellar evolutionary tracks with a precise mass resolution of at least $\Delta M = 0.1$ M$_\odot$ across the entire relevant mass range. This transition, as we will demonstrate, is influenced by various factors, including metallicity, rotation, and more broadly, the effectiveness of near-core mixing mechanisms. If the mass resolution is too low or the range of masses considered is too limited, there's a risk of focusing solely on one side of the transition or even overlooking the transition entirely. Due to all these reasons, we have determined that a practical strategy for studying this group of stars involves creating a grid of models. This grid will possess a fine mass resolution, covering the complete range of masses relevant to the transition. We will explore various initial rotation rates for these models within the grid. Our approach goes beyond the examination of individual models; we are also interested in analyzing collective properties. To do so, we will generate synthetic stellar populations using the grid of models. This will enable us to investigate how the rotation-induced mixing of chemicals impacts the 2RC feature in Hertzsprung-Russell diagrams of stellar populations.

As previously indicated in Section 4.1, the grid of GENEC models presented in Georgy et al. 2013 has two issues that make it unsuitable for our study:

- Insufficient mass resolution.

- The QCHeB phase is not computed for models with $M < 2.5$ M$_\odot$, as these models are computed only up to the He flash phase.

Moreover, the option of supplementing this grid by calculating more GENEC models to enhance mass resolution wasn't feasible for our research objectives for several reasons. One reason is related to the computational cost: considering the mass and rotation ranges along with the necessary resolution, the models that need to be computed would amount to several hundreds. After several tests we concluded that GENEC is not currently optimized for efficiently handling such a substantial number of models in this low mass range, within a reasonable timeframe, given the available computational resources. Additionally, a subset of these models requires computation of the He flash phase, which is computationally demanding. Unfortunately, we concluded that GENEC is not optimized and thoroughly tested for this particular phase. Furthermore, for our investigation into the influence of asteroseismic indicators of rotational mixing of chemicals, we required a straightforward interface with a stellar oscillation code, such as the one linking MESA and GYRE (Townsend and Teitler 2013).

However, as discussed earlier, we believe that GENEC's treatment of rotation through an advecto-diffusive method more accurately captures the underlying physical processes. Considering these factors, to compute our models we opted to use the MESA stellar evolution code (Paxton et al. 2011, Paxton et al. 2013, Paxton et al. 2015, Paxton et al. 2018, Paxton et al. 2019). MESA is well-suited for calculating large grids of models, it is optimized and thoroughly tested for models that include the He flash phase, and it provides a direct interface with the GYRE stellar oscillation code.

To retain the effects of rotation-induced chemical mixing of the Geneva models from the grid presented by Georgy et al. 2013 and examined in detail in Section 4.1, we decided to compute non-rotating MESA models. We incorporated an additional diffusive mixing into these models, calibrated and fine-tuned to replicate the level of rotational mixing observed in the GENEC models within the grid.

5.1   Grid of Models

The stellar models that compose the grid were computed with the code MESA-r11701 (Paxton et al. 2011, Paxton et al. 2013, Paxton et al. 2015, Paxton et al. 2018, Paxton et al. 2019). These models are non-rotating models in which the effect of rotationally induced mixing is introduced as an extra diffusive mixing parameterised and calibrated on GENEC models described in Section 4.1. The grid covers a mass range between $M = 1.7 - 3$ M$_\odot$, with a step $\Delta M = 0.025$ M$_\odot$, and rotationally induced mixing is calibrated for nine

rotation rates on the zero-age main sequence (ZAMS): $\Omega_{ini}/\Omega_{crit} = 0$, 0.1, 0.3, 0.5, 0.6, 0.7, 0.8, 0.9, 0.95.

The following points summarize the relevant physical inputs used.

- The tracks were computed starting from the pre-main sequence (PMS) up to the first thermal pulse of the asymptotic giant branch (TP-AGB).

- We adopt the Asplund et al. 2009 heavy elements partition and high- and low-temperature radiative opacity tables were computed for these specific metal mixtures, the solar and alpha-enhanced[1] ones.

- The initial He mass fraction Y depends on Z and was set using a linear He enrichment expression:

$$Y = Y_p + \frac{\Delta Y}{\Delta Z} Z \tag{5.1}$$

  with the primordial He abundance $Y_p = 0.2485$ and slope $\Delta Y/\Delta Z = (Y_\odot - Y_p) = 0.6969$, where $Y_\odot = 2.57706 \cdot 10^{-1}$ at $Z = Z_\odot$ is the initial value of Y necessary for the solar calibrated model to set the input physics.

- A custom table of nuclear reaction rates was used (JINA; Cyburt et al. 2010).

- The atmosphere is taken according to the Krishna Swamy 1966 model.

- The convective zones are determined with the Schwarzschild criterion.

- Envelope convection is described by the mixing length theory (Cox and Giuli 1968); the corresponding α_{MLT} parameter, the same for all the grid, was derived from the solar calibration with the same physics.

- Below the convective envelope, we added a diffusive undershooting (Herwig 2000) with a size parameter $f = 0.02$ (see Khan et al. 2018).

- For the convective core overshooting during central H burning, we used a diffusive exponential overshooting (Freytag et al. 1996 and Herwig et al. 1997) with an f_{ov} parameter set according to Claret and Torres 2017 (who obtained the relation $\alpha_{ov}/f_{ov} = 11.36 \pm 0.22$) in order to have a equivalent effect of an $\alpha_{ov} \equiv d_{ovsh}/H_p = 0.10$ in the step overshooting formalism as used in GENEC models.

- Extra mixing over the convective core limit during the core He-burning phase was treated following the formalism by Bossini et al. 2017.

---

[1]Alpha-enhanced stars exhibit elevated abundances of alpha-capture elements such as oxygen (O), magnesium (Mg), silicon (Si), calcium (Ca), and titanium (Ti) with respect to the solar values.

- Element diffusion, which includes the effects of radiative accelerations, has been omitted from our models. This omission is due to the fact that during the main-sequence phase, non-rotating or slowly rotating models would necessitate the introduction of an artificial diffusion coefficient profile to prevent excessive metal depletion in the surface layers. In practice, the use of these profiles would result in a contamination of the effects of rotation. Therefore, we chose to exclude element diffusion to avoid these difficulties. Additionally, it's worth noting that element diffusion and radiative acceleration have negligible impacts on giants, the category of stars that we are primarily concerned with in this study.

- Rotation-induced mixing has been introduced as an extra diffusive mixing parameterised and calibrated on GENEC models described in Section 4.1. The parameterisation and calibration of the MESA models is described in Section 5.1.1.

- Mass loss is not considered.

5.1.1 Implementation of Rotation-Induced Mixing of Chemical Species

As discussed in Section 3.1.10, the influence of rotational mixing on the distribution of chemical species along the vertical direction can be described using a diffusion equation (3.49). This equation involves a combined diffusion coefficient $D_{mix} = D_{eff} + D$, where $D = D_{shear} + D_{conv}$. The specific profiles and contributions to D_{mix} during the evolution of stars with masses between 1.7 $M_{\odot}$ and 3 $M_{\odot}$ are explained in detail in Section 4.1. The same equation is used to describe chemical species mixing in MESA. However, the diffusion coefficient D_{mix}, calculated as the sum of individual mixing processes (Heger et al. 2000), may not be exactly the same. This discrepancy is mainly due to the differing treatment of rotational mixing compared to GENEC. Nonetheless, MESA allows for adjustments to be made to the default behavior of the code, particularly through the run_star_extras.f file. This provides the option to customize the value of D_{mix} as needed.

We took advantage of this opportunity to incorporate the impact of rotational mixing from the GENEC models, as described in Section 4.1, into non-rotating MESA models. This addition contributes to the overall D_{mix}. To achieve this, our initial task was to find a way to represent the D_{mix} profile that could be added to D_{mix}. As explained in Section 4.1, the D_{mix} profile depends on factors like initial mass M, initial rotation rate $\Omega_{ini}/\Omega_{crit}$, and the star's position on the main sequence (characterized by either age or $X_{H,c}$). Despite the complex behavior of these profiles – sometimes showing abrupt changes and irregular patterns as illustrated in Figure 4.4 – their general shape tends to stay somewhat consistent on average, similar to the pattern shown in Figure 4.1. It is important to note that these deviations are temporary and short-lived during the main

sequence evolution. Considering this observation, it makes sense to come up with a generalized form that can match the average D_{mix} profile in a systematic way. This form can then be scaled based on the values of mass M, initial rotation rate $\Omega_{ini}/\Omega_{crit}$, and either age or $X_{H,c}$.

Parameterization of the D_{mix} profile

We start by separating the various functional dependencies:

$$D_{mix} = D_{eff} + D_{shear}. \tag{5.2}$$

The last remark in the previous paragraph assures us that, with a good approximation, the various dependencies can be factored as:

$$D_{eff} = D_{eff}(X_{^1H,c}, q, \Omega_{ini}/\Omega_{crit}, M) \approx f(q)g(X_{^1H,c})h(\Omega_{ini}/\Omega_{crit})k(M), \tag{5.3}$$

$$D_{shear} = D_{shear}(X_{^1H,c}, \Omega_{ini}/\Omega_{crit}, M) \approx F(q)G(X_{^1H,c})H(\Omega_{ini}/\Omega_{crit})K(M), \tag{5.4}$$

where $q = M_r/M$. Regarding D_{eff}, as a first approximation for $f(q)$, we can consider $f = f(q) = const.$ (see Fig. 4.1) and $g(X_{^1H,c}) = \overline{g(X_{^1H,c})}$ as an "effective value" for the entire MS (see Fig. 4.4):

$$D_{eff} \approx f(q)g(X_{^1H,c})h(\Omega/\Omega_{crit})k(M) \approx f \cdot \overline{g(X_{^1H,c})}h(\Omega/\Omega_{crit})k(M) \approx$$
$$\approx \overline{D_{eff}}(\Omega/\Omega_{crit}, M). \tag{5.5}$$

The values of $\overline{D_{eff}}(\Omega/\Omega_{crit}, M)$ will be fixed for each value of $\Omega_{ini}/\Omega_{crit}$ and M, using the calibration technique presented later. For D_{shear}, as a first approximation, we can consider $G(X_{^1H,c}) = \overline{G(X_{^1H,c})}$ as an "effective value" for the entire MS (see Fig. 4.4). Also, $F(q)$ is well approximated (see Fig. 5.1 to compare with the dotted line in Fig. 4.1) by the following function:

$$F(q) \approx \sigma \cdot \{[q - (q_{cc} + \Delta q_{ovsh} + \delta q)] + 10^{a \cdot q - b}\}. \tag{5.6}$$

Where Δq_{ovsh} is the extension of overshooting from the convective boundary. Also:

$$\sigma \approx \overline{G(X_{^1H,c})}H(\Omega/\Omega_{crit})K(M) \approx \sigma(\Omega/\Omega_{crit}, M), \tag{5.7}$$

and its value will be fixed for each value of $\Omega_{ini}/\Omega_{crit}$ and M using the calibration technique presented later. Finally, a, b, δq are fine-tuned parameters, which work well for all masses
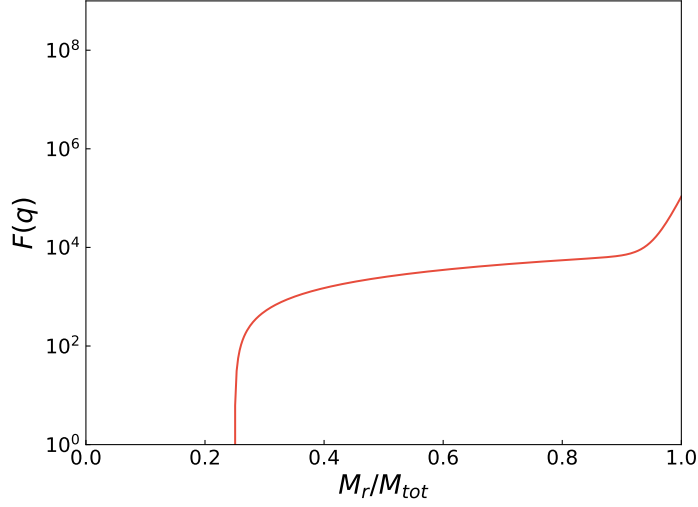
Figure 5.1: Example of a profile given by (5.6): $F(q) = 10000 \cdot [x - 0.25 + 10^{(24x-23)}]$.

and rotations[2]:

$$
\begin{aligned}
a &= 24, \\
b &= -23, \\
\delta q &= 0.03.
\end{aligned}
\tag{5.8}
$$

So, ultimately, the D_{mix} profile is parameterized as follows:

$$
D_{mix} = \overline{D_{eff}} \qquad\qquad\qquad\qquad\qquad\qquad if\ q \leq (q_{cc} + \Delta q_{ovsh} + \delta q) \tag{5.9}
$$
$$
D_{mix} = \overline{D_{eff}} + \sigma \cdot \{[q - (q_{cc} + \Delta q_{ovsh} + \delta q)] + 10^{a \cdot q - b}\} \quad if\ q \geq (q_{cc} + \Delta q_{ovsh} + \delta q). \tag{5.10}
$$

Essentially, $\overline{D_{eff}}(\Omega_{ini}/\Omega_{crit}, M)$ sets the value of the near-core region of the profile (where the dominant contribution comes from the combined effect of meridional circulation and horizontal turbulence), while $\sigma(\Omega_{ini}/\Omega_{crit}, M)$ scales the contribution of the shear.

Calibration of $\overline{D_{eff}}(\Omega_{ini}/\Omega_{crit}, M)$ and $\sigma(\Omega_{ini}/\Omega_{crit}, M)$

Now we need to calibrate $\overline{D_{eff}}(\Omega_{ini}/\Omega_{crit}, M)$ and $\sigma(\Omega_{ini}/\Omega_{crit}, M)$ to reproduce the effects of rotation-induced mixing of chemicals discussed for the GENEC models. In practice, we

---

[2]The fine-tuning of a, b, δq was performed by comparing the parameterized profile with D_{mix} profiles shown in Section 4.1 at different points in the MS, for all masses and initial rotations. We adjusted a, b, δq until the profiles were a good fit. Despite the apparent roughness of this technique, changes in the values of these parameters have a minimal impact. Any differences can be automatically compensated by slight changes in the parameters $D_{eff}(\Omega/\Omega_{crit}, M)$ and $\sigma(\Omega/\Omega_{crit}, M)$

need to assign, for each value of M and $\Omega_{ini}/\Omega_{crit}$ covered by the grid described in Section 4.1, a calibrated value of $\overline{D_{eff}}$ and σ.

Since the Geneva reference models and the MESA models computed for this work comes from two different evolutionary codes and with slightly different input physics, a direct comparison of tracks/quantities isn't a reliable calibration method. Such comparisons could result in significant offsets due to these differences. To avoid these issues, we calibrate, for each mass value M and $\Omega_{ini}/\Omega_{crit}$, σ and $\overline{D_{eff}}$ to replicate the relative changes in quantities affected by rotation-induced chemical mixing between rotating models (for each $\Omega_{ini}/\Omega_{crit}$) and non-rotating ones.

We define five parameters based on quantities sensitive to rotational mixing of chemicals during the MS:

1. The ratio between the total mass of ^4He in the rotating model and the non-rotating model at TAMS:

$$\Pi_1 \equiv M_{tot,^4He}^{rot}/M_{tot,^4He}^{norot} \quad \text{at TAMS.} \tag{5.11}$$

   This parameter is sensitive to rotational mixing because, between two models with the same input physics, but one rotating and the other non-rotating, in the rotating one, the rotational mixing during the MS continually brings fresh hydrogen into the core. This results in a larger fraction of hydrogen transforming into helium at TAMS. The advantage of this parameter, in contrast to others like the size of the convective core at a specific MS stage, is its dependence only on the overall mixing throughout the MS, making it more compatible with our chosen approach.

2. The ratio between the age at TAMS of the rotating model and the non-rotating one:

$$\Pi_2 \equiv age^{rot}/age^{norot} \quad \text{at TAMS.} \tag{5.12}$$

   This parameter is sensitive to rotational mixing because, between two models with the same input physics, but one rotating and the other non-rotating, in the rotating one, the rotational mixing during the MS continually brings fresh hydrogen into the core. The increased available fuel leads to a longer MS duration.

3. The ratio between the coordinate $q = M_r/M$ at which the μ profile has the value $\mu = 0.65$ in the rotating model and the non-rotating one:

$$\Pi_3 \equiv q_{|\mu=0.65}^{rot}/q_{|\mu=0.65}^{norot} \quad \text{at TAMS.} \tag{5.13}$$

   This parameter is sensitive to rotational mixing because it represents the coordinate of the change in slope of the μ profile. As seen in Fig. 4.5a, this region of the μ profile changes significantly with rotation due to helium being transported from the convective core to the radiative envelope.

4. The ratio between the surface abundance of ^{14}N in the rotating model and the non-rotating model at TAMS:

$$\Pi_4 \equiv {}^{14}N_{surf}^{rot}/{}^{14}N_{surf}^{norot} \quad \text{at TAMS}. \tag{5.14}$$

This parameter is sensitive to rotational mixing because, as the material is processed by CNO cycle reactions in the core, the abundance of ^{14}N relative to other elements, like ^1H or ^{12}C, increases. Rotational mixing transports this processed material to the surface.

5. The ratio between the surface abundance of ^4He in the rotating model and the non-rotating model at TAMS:

$$\Pi_5 \equiv {}^4He_{surf}^{rot}/{}^4He_{surf}^{norot} \quad \text{at TAMS}. \tag{5.15}$$

This parameter is sensitive to rotational mixing for the same reasons as $\Pi_{{}^{14}N_{surf}}$. We include a second parameter related to the surface abundances of elements sensitive to rotational mixing to avoid potential problems due to abundance variations resulting from processes unrelated to rotational mixing.

For each model from the grid described in Section 4.1, we computed the values of five parameters Π_i^{GENEC}, where $i = 1, 2, 3, 4$. Additionally, approximately at the middle of the MS, we determined the average value of the D_{eff} profile near the core $\langle D_{eff} \rangle_{nc}$ and the value of σ by fitting a D_{mix} profile using the profile given by Equation (5.6) to use as starting values $\overline{D_{eff}}_{start}$ and σ_{start} for the calibration. For each combination of M and $\Omega_{ini}/\Omega_{crit}$, we generated a grid of MESA models that were evolved up to the TAMS. In this grid, we varied $\overline{D_{eff}}$ and σ within intervals centered around $\overline{D_{eff}}_{start}$ and σ_{start}, with the limits being set by the maximum and minimum values of $\langle D_{eff} \rangle_{nc}$ and σ attained during the MS. The intervals $[\langle D_{eff} \rangle_{nc}^{min}, \langle D_{eff} \rangle_{nc}^{max}]$ and $[\sigma^{min}, \sigma^{max}]$ were divided into 25 equally spaced values, resulting in a calibration grid of 625 models. For each model in this calibration grid, we calculated the values of Π_i^{MESA} (where $i = 1, 2, 3, 4$) and determined the root mean square error (RMSE) compared to the corresponding parameters in the reference GENEC model:

$$RMSE = \sqrt{\frac{\sum_{i=1}^{4} (\Pi_i^{MESA} - \Pi_i^{GENEC})^2}{4}}. \tag{5.16}$$

The calibrated model was chosen as the one in the grid with the minimum RMSE[3]. If the model did not lie at the boundary of the intervals of $\overline{D_{eff}}$ and σ covered by the

---

[3]After identifying the RMSE minimum, a refined calibration grid was constructed around the optimal parameters, with the parameter range limited to the resolution of the previous grid. The minimization process was repeated in this refined grid.

Calibration parameter	$\Omega_{ini}/\Omega_{crit} = 0.3$	$\Omega_{ini}/\Omega_{crit} = 0.5$	$\Omega_{ini}/\Omega_{crit} = 0.8$
Π_1	1.0600	1.0953	1.1123
Π_2	1.1647	1.2544	1.3180
Π_3	1.5554	1.8125	1.9649
Π_4	1.0016	1.1206	1.4394
Π_5	1.0000	1.0015	1.0055

Table 5.1: Reference calibration parameters Π_i ($i = 1, 2, 3, 4, 5$) calculated for the 2 M$_\odot$ reference GENEC model.

grid, the grid was extended until the minimum was no longer located at the boundaries. This minimization method, while not ensuring discovery of the global minimum in the parameter space, facilitated identification of the local minimum closest to the initial values calculated from the reference models. It's noteworthy that this approach was usually effective in locating the local minimum within a few steps of the grid from the starting values.

Employing this method, each combination of $(M, \Omega_{ini}/\Omega_{crit})$ was matched with a MESA non-rotating model of mass M, incorporating an additional mixing using a diffusion coefficient profile as described by Equations (5.9)-(5.10). This profile was calibrated to replicate the rotational mixing of chemicals of a GENEC model with mass M and an initial rotation rate $\Omega_{ini}/\Omega_{crit}$. Figure 5.2 displays the outcomes of the $\overline{D_{eff}}$ and σ calibration for a 2.5 M$_\odot$ model. The observed behaviors of these parameters correlate with the qualitative observations derived from the diffusion coefficients μ profiles and tracks of the reference models. Specifically, $\overline{D_{eff}}$, influencing the near-core region of the profile representing the combined effect of meridional circulation and horizontal turbulence, demonstrated an increasing trend with $\Omega_{ini}/\Omega_{crit}$, with a decreasing slope that tended to flatten and even reverse for faster rotators (0.8, 0.9, 0.95 $\Omega_{ini}/\Omega_{crit}$). On the other hand, σ, primarily scaling the shear contribution, exhibited a more linear increase, with a markedly pronounced rise relative to $\overline{D_{eff}}$. Figures 5.3 and 5.4 showcase examples of D_{mix} profiles in our calibrated MESA models corresponding to different rotation rates for 2.5 M$_\odot$ models, and to different masses for a fixed $\Omega_{ini}/\Omega_{crit} = 0.5$ respectively.

With the calibration grid complete, the following step involved scrutinizing the results. This consisted in verifying whether the calibrated rotational mixing models adequately replicated the properties of the reference rotating models outlined in Section 4. Figure 5.5 shows the evolutionary tracks of the calibrated MESA models, presented in the same format used for the reference Geneva models depicted in Figure 4.11. These calibrated MESA models, being non-rotating models, of course does not include hydrostatic effects,
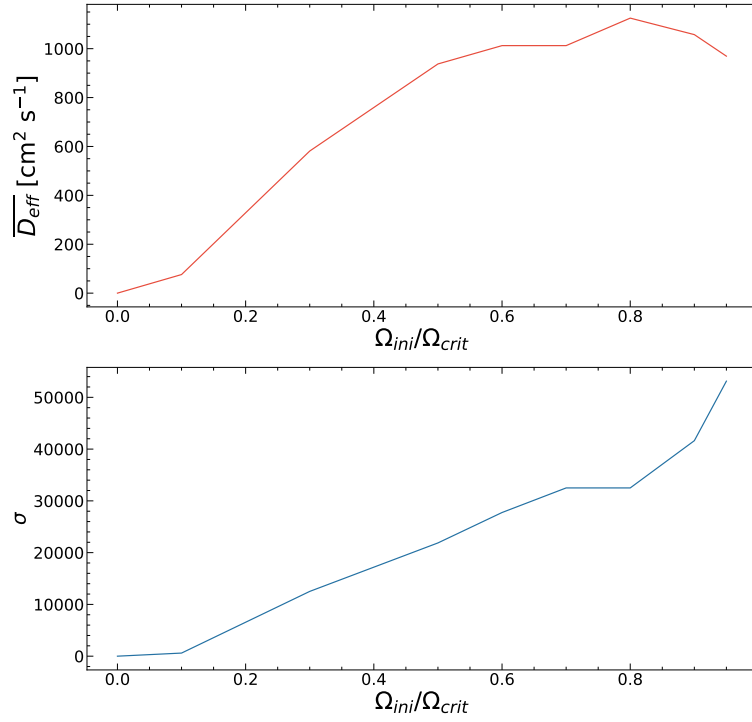
Figure 5.2: Results of the calibration of the two parameters $\overline{D_{eff}}$ and σ of the D_{mix} parametric profile (5.9)-(5.10) for 2.5 $M_\odot$ models a a function of initial rotational rate.
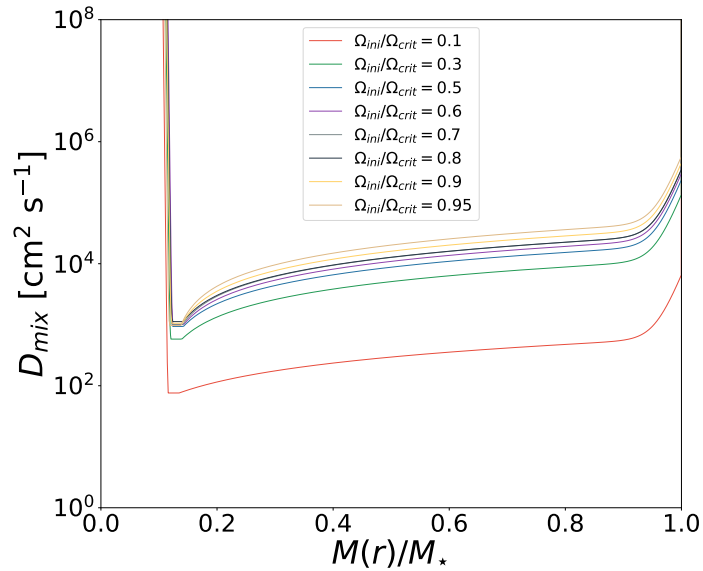
Figure 5.3: D_{mix} profiles in our calibrated MESA models of 2.5 $M_\odot$ corresponding to 0.3, 0.5, 0.6, 0.7, 0.8, 0.9 $\Omega_{ini}/\Omega_{crit}$.
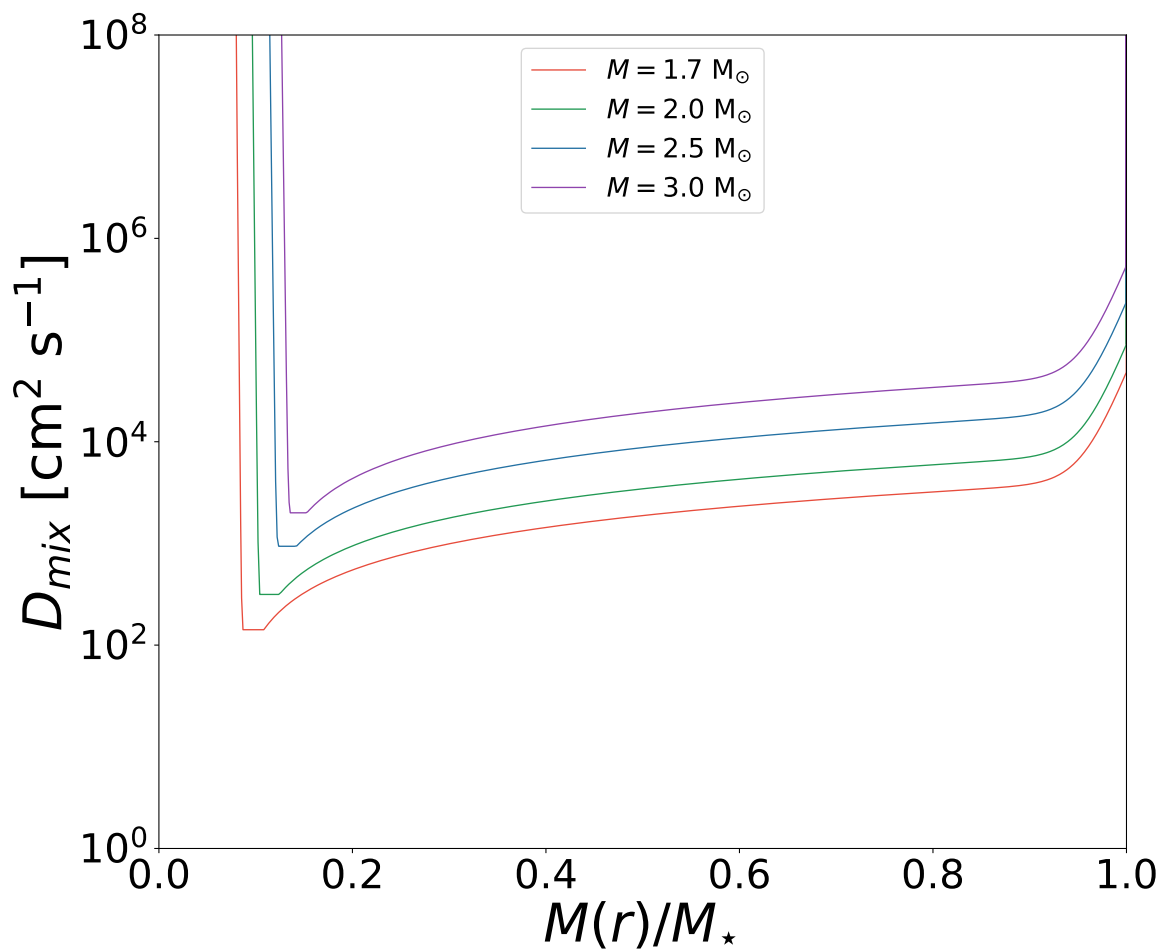
Figure 5.4: D_{mix} profiles in our calibrated MESA models of 1.7 M$_\odot$ (red), 2.0 M$_\odot$ (green), 2.5 M$_\odot$ (blue), 3.0 M$_\odot$ (violet) for a fixed $\Omega_{ini}/\Omega_{crit} = 0.5$.
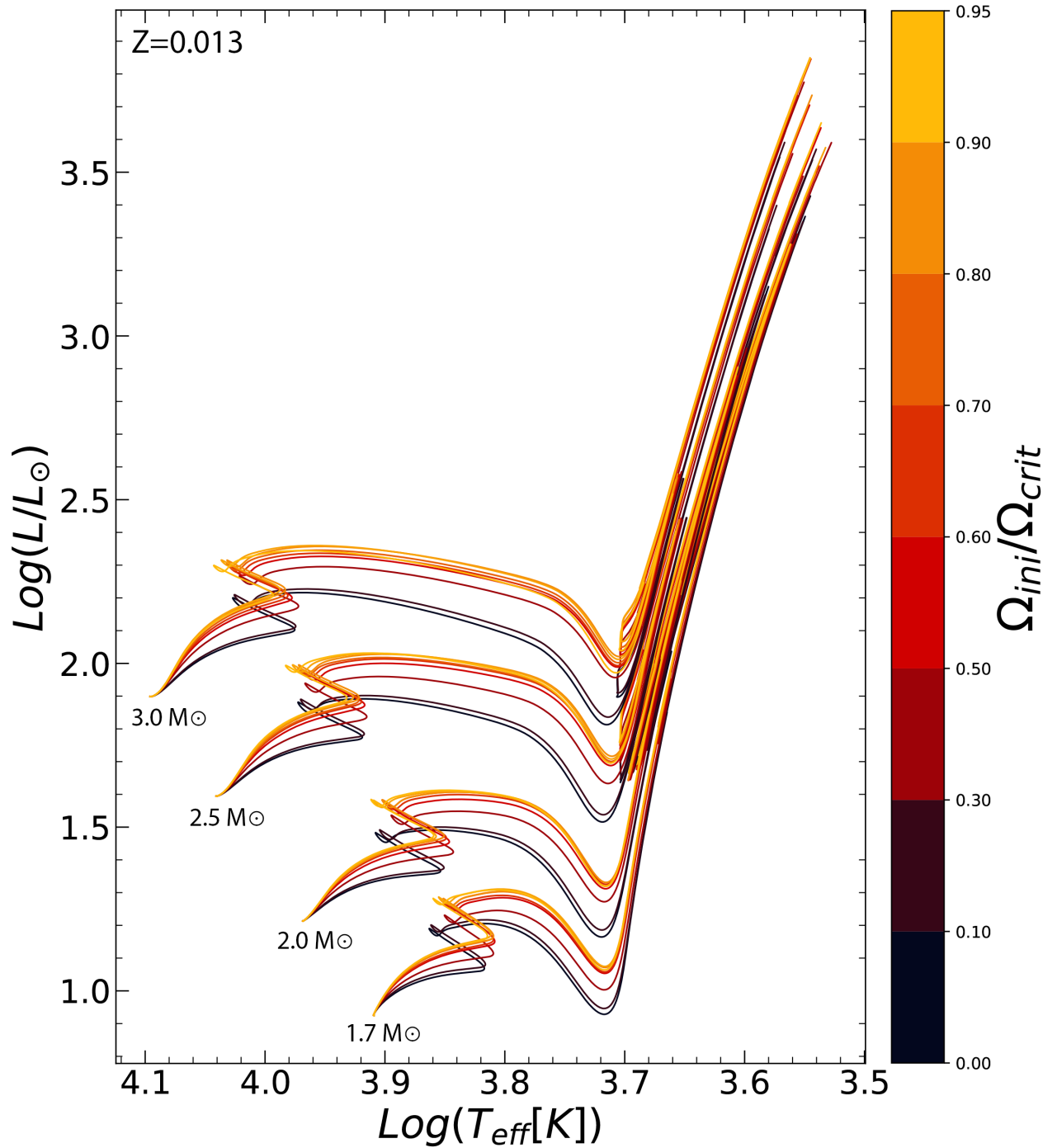
Figure 5.5: Evolutionary tracks of our `MESA` calibrated models for rotational mixing for models with the same masses and rotation rates presented for the `GENEC` reference models.

resulting in all tracks originating from the same ZAMS model. Consequently, unlike the post MS phases, the MS phase in these tracks is not reproduced correctly in the HR diagram. However, the effects of rotational mixing of chemicals were reasonably well captured. Notably, if one aligns the initial point of each track from the reference models on the ZAMS, approximately removing the hydrostatic effects, the trend of the tracks in our `MESA` calibrated models closely follows the behavior of the tracks of the reference models with increasing initial rotation. This alignment becomes even more evident post-MS, when the hydrostatic effects become negligible.

Further validation of the efficacy of the rotational mixing calibration emerges from the comparison of μ profiles and chemical abundances profiles at the TAMS and the initial QCHeB phase. As showed in Figure 5.9, the profiles for different $\Omega_{ini}/\Omega_{crit}$ values from our calibrated `MESA` models are almost indistinguishable from those of the reference Geneva models. Once the grid of calibrated `MESA` models was completed, we refined the mass
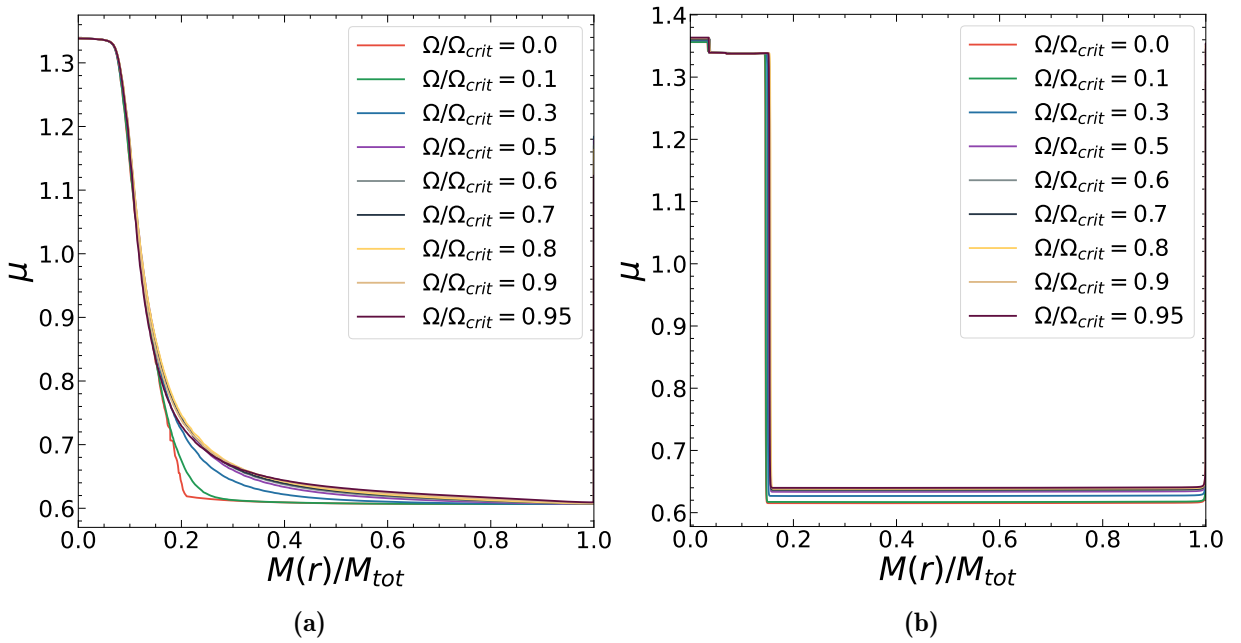
Figure 5.6: Mean molecular weight profiles at TAMS (a) and at initial QCHeB (b) for 2.5 M$_\odot$ `MESA` calibrated models for 0.0, 0.1, 0.3, 0.5, 0.6, 0.7, 0.8, 0.9, 0.95 $\Omega_{ini}/\Omega_{crit}$.

resolution by computing additional models to obtain a mass resolution of $\Delta M = 0.025$. In order to do this we linearly interpolated the values of $\overline{D_{eff}}$ and σ of the calibration grid.

It is important to remark that this approach represents an approximation of the rotational mixing effects in `GENEC` models. It relies on fitting an effective D_{mix} profile and overlooks its evolution during the MS, as well as rotational mixing effects in post-MS phases. This method was conceived as a workaround to circumvent the computational challenges of generating extensive grids of models that pass through the helium flash using

an evolutionary code like GENEC. Ideally, such a grid would have been constructed using GENEC itself. Nevertheless, the profile was calibrated to replicate the consequences of rotational mixing of chemicals in GENEC models, yielding an "effective D_{mix} profile" that, although possibly slightly deviating from the actual profile, still captures its primary features and effectively reproduces the effects on the transport of chemicals. Additionally, we remark that these models were calibrated solely to capture the effects of rotation-induced mixing of chemicals, and they do not account for hydrostatic effects. Thus, they should not be used to study the MS phase. Indeed, as demonstrated by Eggenberger et al. 2010., hydrostatic effects can significantly impact the MS phase, though they become negligible during post-MS phases. Despite this limitation, our models remain suitable for investigating post-MS phases, such as the red clump and 2RC.

5.2 Impact of Different Main Sequence Mixing Prescriptions

5.2.1 Convective Core Overshooting

The effect of rotation on the transport of chemical species in 1D stellar models is known to be similar, though not identical to, that of convective core overshooting. This is because chemical gradients left by overshooting, either step or exponential, are different from those produced by a diffusive process such as chemical transport in shellular rotation. Eggenberger et al. 2010 investigated the differences between evolutionary tracks including either diffusion or rotation in the colour-magnitude diagram. They conclude that the main-sequence widening and the increase of the H-burning lifetime induced by rotation are well reproduced by non-rotating models with an overshooting $\alpha_{ov} = 0.1$, while the increase of the stellar luminosity induced by rotational mixing (in particular during the post-MS phase) is better reproduced by a non-rotating model with a larger value of the overshooting parameter $\alpha_{ov} = 0.2$.

It is interesting to study the difference between our models from the calibrated grid described in Section 5.1 and models with the same input physics but without any additional D_{mix} with an exponential overshooting calibrated to produce the same amount of mixing present in the rotating reference models. We calibrated the f_{ov} with the same minimization technique, but since overshooting is not able to transport chemicals far from the boundary of the convective core, Π_3, Π_4, Π_5 are essentially not affected (only Π_3 is mildly affected, but it doesn't hold the same role) by overshooting. The approach that we decided to use in this case is to calibrate only using Π_1 and Π_2, in order to calibrate only the amount of mixing and not its extension in the envelope. The results of the calibration of f_{ov} for a 2.0 M$_\odot$ are shown in Tab.5.2, we can see how f_{ov} is increasing with $\Omega_{ini}/\Omega_{crit}$

$\Omega_{ini}/\Omega_{crit}$	f_{ov}
0.0	0.00000
0.1	0.00529
0.3	0.02114
0.5	0.02994
0.6	0.03346
0.7	0.03698
0.8	0.03698
0.9	0.03874
0.95	0.03874

Table 5.2: Result of the calibration of f_{ov} for 2.0 M$_\odot$ models.

of the reference models up to around 0.5 reflecting the already mentioned saturation of the effects of rotational mixing after $\Omega_{ini}/\Omega_{crit} \simeq 0.5$. In terms of mean molecular weight

(a)   **(b)**
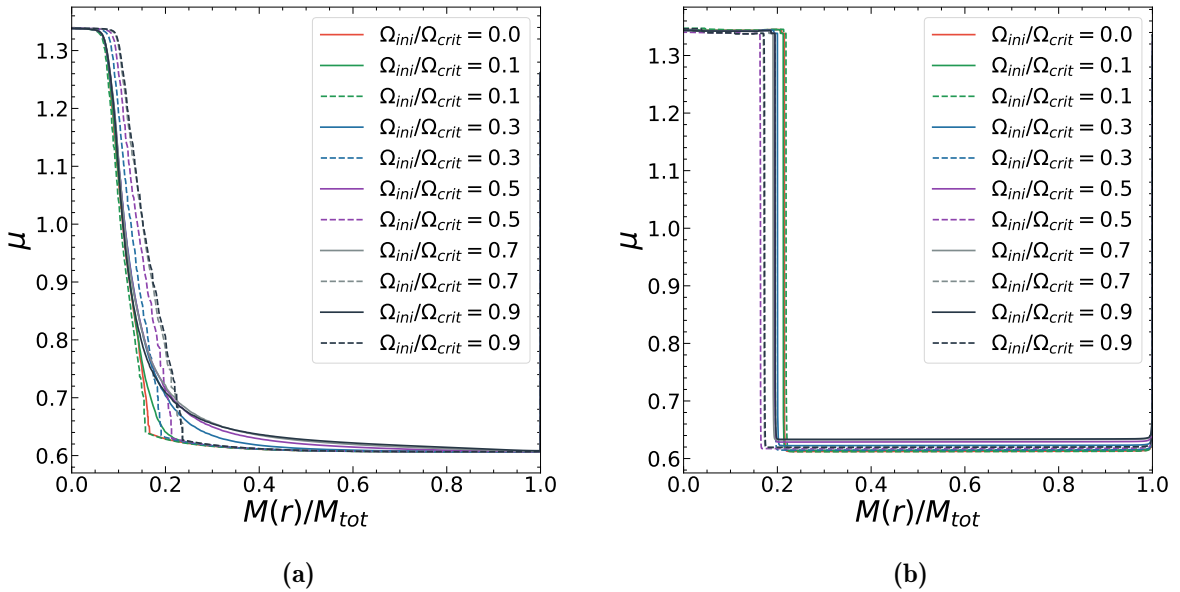
Figure 5.7: Mean molecular weight profiles at TAMS (a) and at initial QCHeB (b) for 2.0 M$_\odot$ MESA models with the D_{mix} parametric profile in Eq. (5.10) (solid lines) and only overshooting (dashed lines) calibrated to reproduce rotational mixing for different $\Omega_{ini}/\Omega_{crit}$.

profiles, it is evident that diffusive overshooting results in a distinctively steep and sharp μ profile near the TAMS, especially when compared to rotational mixing (refer to Fig.5.7a). During the initial QCHeB phase, this effect primarily influences the core size, while it has a minimal impact on the average μ within the envelope.

The effect on the evolutionary tracks is noticeable in Fig. 5.8, as there is a prolonged main sequence (MS) phase due to the increased availability of fuel facilitated by over-shooting, which is a more efficient near-core mixing process than rotational mixing. The post-MS phases are primarily influenced by the difference in the size of the He core, which is determined by the extent to which H has been transformed into He through nuclear reactions. The tracks with only diffusive overshooting generally have lower luminosity, primarily because the mean molecular weight (μ) within the envelope is reduced, as a result of the absence of extended mixing like rotational mixing.

For instance, in the case of 2.0 $M_\odot$ models, those with greater overshooting experience a decrease in luminosity during the quiescent core helium burning (QCHeB) phase. This decline occurs because the core is smaller at this stage, even though it is the opposite at the turn-off of the main sequence (TAMS). This phenomenon arises because, for 2.0 $M_\odot$ models, altering the value of the overshooting parameter, known as f_{ov}, can lead to either degenerate or weakly/non-degenerate ignition of helium in the core. This choice, in turn, influences the extent of core growth during the red giant branch (RGB) phase. Should the core become degenerate, it can grow more (in mass) compared to a model of similar mass, where the core remains weakly/non-degenerate. This concept is fundamental to understanding the transition responsible for the emergence of secondary clump stars. This effect is observed with rotational mixing as well, although it is somewhat mitigated by the increased mean molecular weight (μ) in the envelope, resulting in an increased luminosity.

5.2.2 Flat D_{mix} Profiles

An alternative method to the approach we have adopted in this study would involve refraining from assuming a specific shape for the diffusion coefficient profile. Instead, it would assume, as discussed in Section 3.1, that rotation induces an extended mixing process from the core to the surface, effectively resulting in a flat diffusion coefficient profile as done in Miglio et al. 2008. While this approach is more cautious as it avoids making particular assumptions about transport processes that, as previously emphasized, are still not well-understood, it does come with certain drawbacks. Namely, if the goal is to conduct a study that provides quantitative predictions rather than qualitative insights, a link between the values of D_{mix} and rotation rates is required. This link can only be established through a calibration of D_{mix} based on some rotating models. Thus, calibrating a flat profile against the existing reference models would yield a less accurate representation of rotational mixing within the models.

Nonetheless, it remains interesting to compare this alternative approach with the one chosen for this work, as it can help illustrate the impact of alterations to the D_{mix} profile.
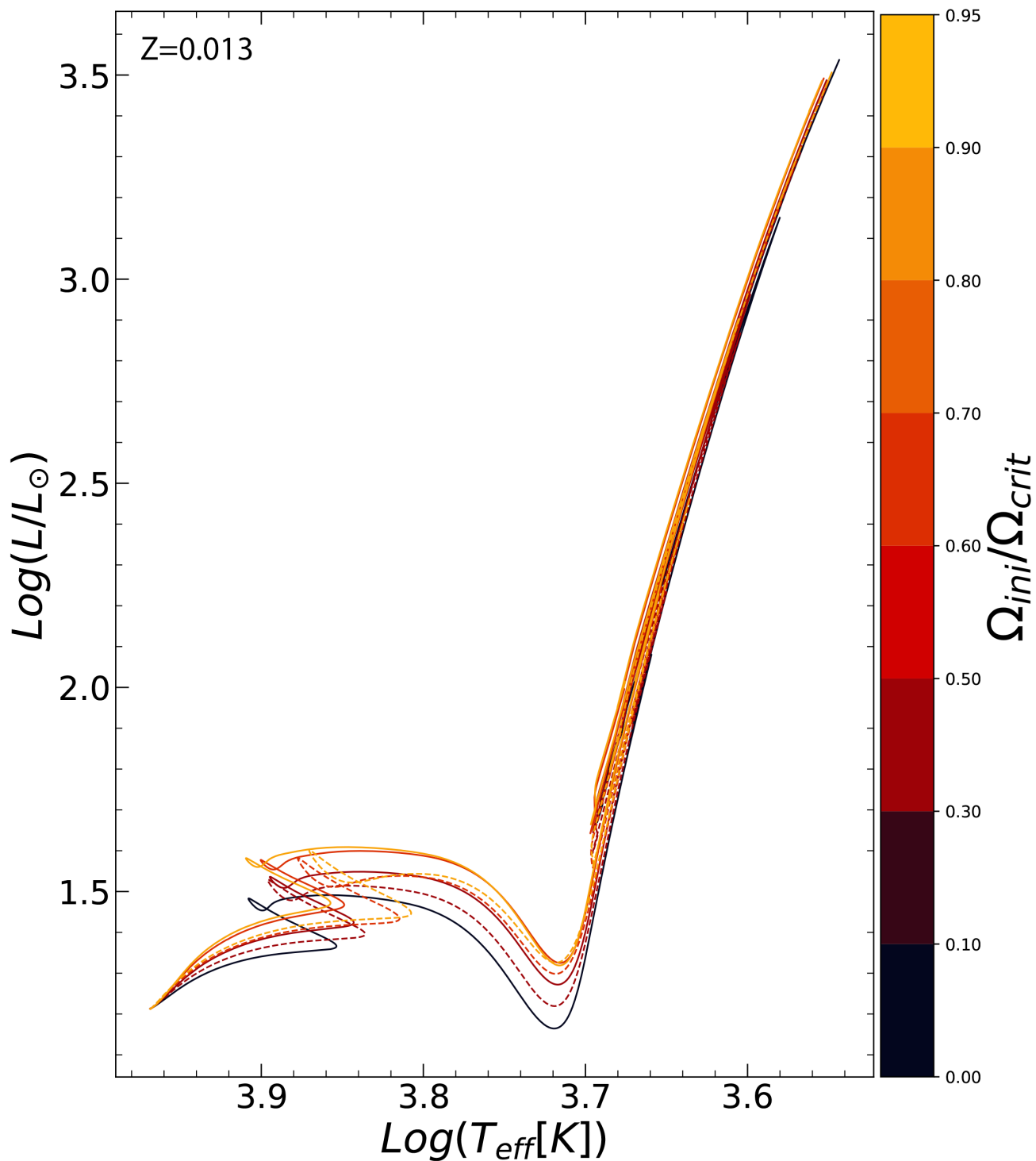
Figure 5.8: Evolutionary tracks of 2.0 $M_\odot$ MESA models, calibrated for rotational mixing at various rotation rates using the parametric D_{mix} profile (5.9)-(5.10), are depicted by the solid lines. In contrast, the dashed lines represent models incorporating solely an exponential overshooting with the calibrated parameter f_{ov}.

In order to do the comparison we reapeated the calibration described in Section 5.1.1 on

| Calibration parameter	$\Omega_{ini}/\Omega_{crit} = 0.3$ parametric / flat	$\Omega_{ini}/\Omega_{crit} = 0.5$ parametric / flat	$\Omega_{ini}/\Omega_{crit} = 0.8$ parametric / flat
Π_1	1.0612 / 1.0629	1.0926 / 1.0989	1.1114 / 1.1234
Π_2	1.1433 / 1.1473	1.2104 / 1.2230	1.2491 / 1.2708
Π_3	1.5760 / 1.5760	1.8295 / 1.8102	1.9449 / 1.9830
Π_4	1.0000 / 1.0000	1.1048 / 1.0000	1.4443 / 1.0000
Π_5	1.0001 / 1.0000	1.0007 / 1.0000	1.0042 / 1.0000
$\overline{D_{eff}}$	212.50 / 240.00	315.00 / 438.00	362.50 / 588.00
σ	2875.00 / 0.00	8333.33 / 0.00	12812.5 / 0.00
RMSE	0.0133 / 0.0122	0.0223 / 0.0558	0.0322 / 0.1979

Table 5.3: Calibration parameters Π_i ($i = 1, 2, 3, 4, 5$) and RMSE calculated for our calibrated MESA models with the parameteric and flat D_{mix} profiles.

models with a flat D_{mix} profile. In Tab.5.3 we show the results of the calibration of 2.5 $M_\odot$ models for 0.1, 0.5 and 0.8 $\Omega_{ini}/\Omega_{crit}$ with a parametric D_{mix} profile as described in Section 5.1.1 and with a flat one, while in Tab. 5.2 we show the reference calibration parameters calculated from the reference rotating models.

To achieve a flat D_{mix} profile, we set σ to zero and permit only $\overline{D_{mix}}$ to be adjustable during the calibration process. The outcomes of this calibration are presented in Tab.5.3. The calibration results in a higher value of $\overline{D_{mix}}$ which is necessary to compensate for the absence of contribution from the $F(q)$ profile. However, this adjustment leads to a less accurate reproduction of the rotational mixing found in the reference model. This is evident in the larger Root Mean Square Error (RMSE), indicating a less favorable match between the calibrated model and the reference model's rotational mixing properties. Regarding the mean molecular weight profiles, the increased $\overline{D_{mix}}$ results in enhanced near-core mixing, yet reduced mixing in the envelope. This leads to a more pronounced steepening of the μ profile near the TAMS. During the initial QCHeB phase, this effect primarily impacts the core size, while having a relatively smaller influence on the average μ in the envelope. The effect on the evolutionary tracks as shown in Fig.5.10, remains an extended main-sequence (MS) phase due to the augmented fuel supply caused by the larger $\overline{D_{mix}}$. The subsequent post-MS phases are shaped by both the variation in the He core's size, determined by the extent of H transformed into He through nuclear reactions, and the higher mean molecular weight (μ) in the envelope. However, it's important to note that μ is smaller compared to the case with the parametric D_{mix} because of the absence of the $F(q)$ profile (which takes into account the extended envelope mixing due to shear instability).
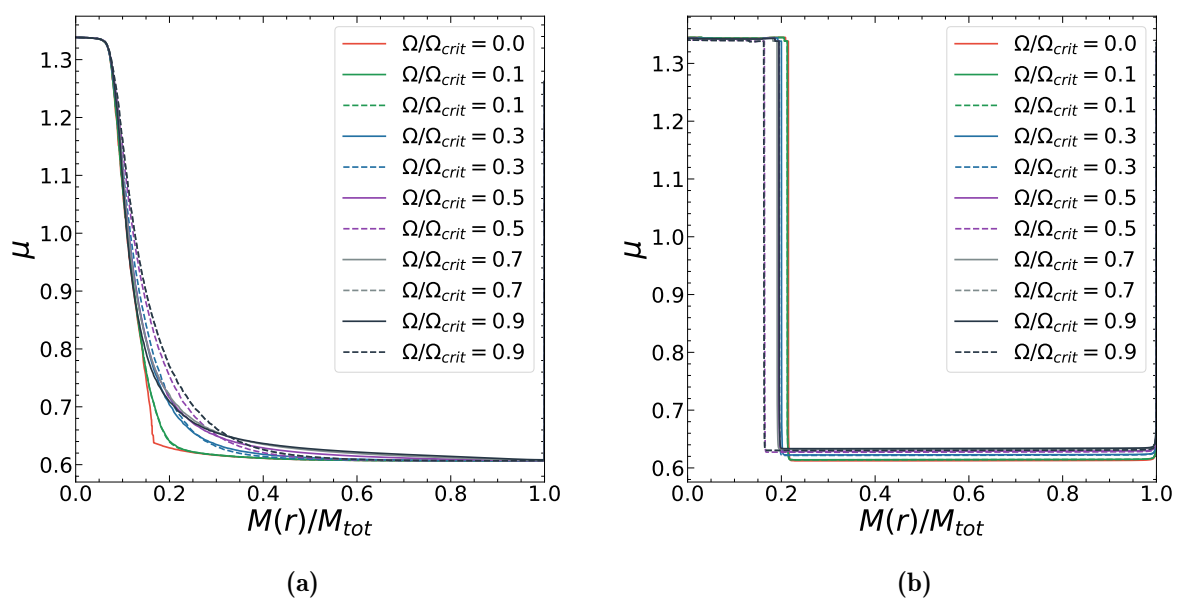
Figure 5.9: Mean molecular weight profiles at TAMS (a) and at initial QCHeB (b) for 2.0 $M_\odot$ MESA models with the D_{mix} parametric profile in Eq. (5.10) (solid lines) and a flat profile (dashed lines) calibrated to reproduce rotational mixing for different $\Omega_{ini}/\Omega_{crit}$.
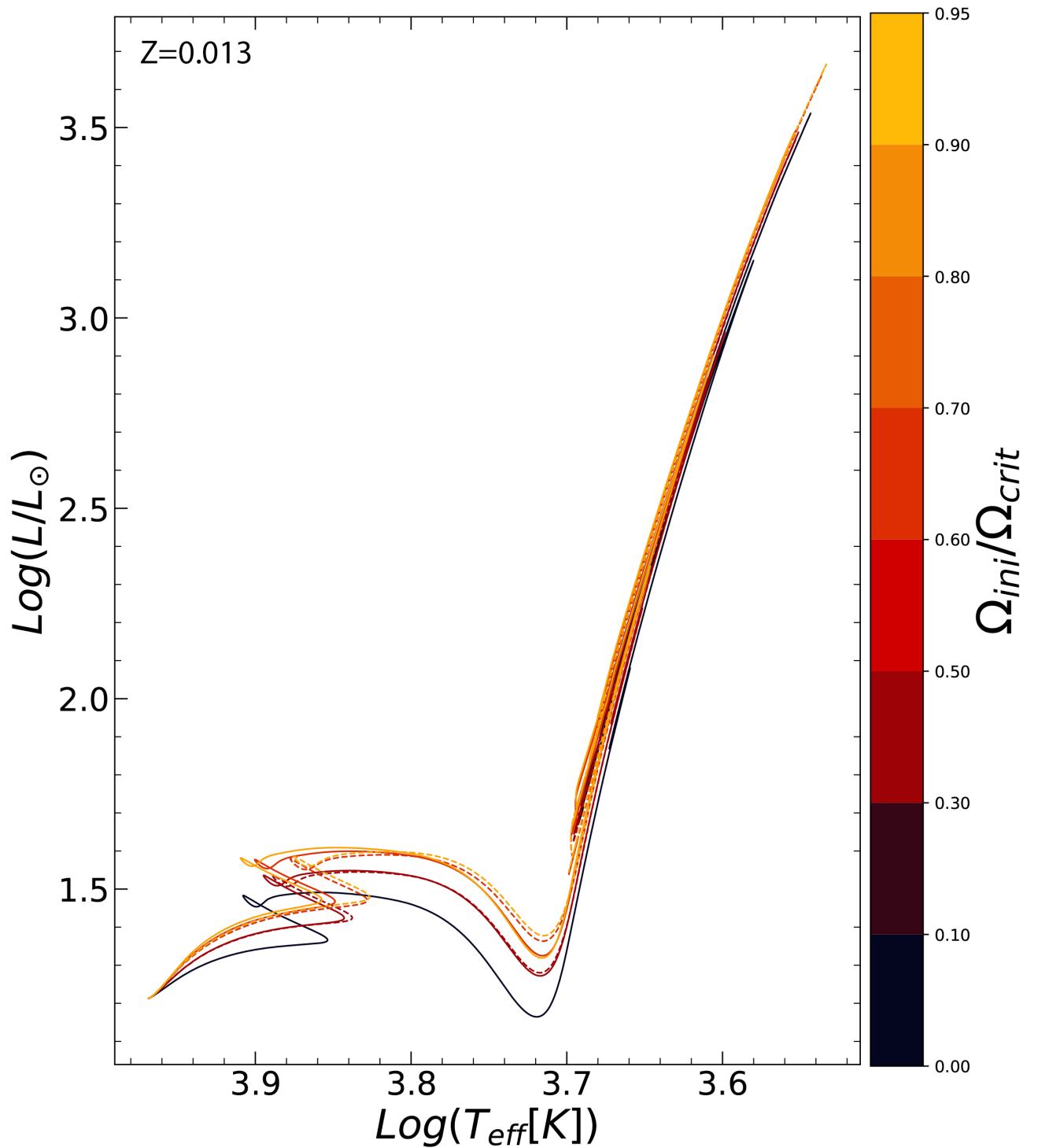
**Figure 5.10:** Evolutionary tracks of 2.0 M$_\odot$ MESA calibrated models for rotational mixing at different rotation rates by using the parametric D_{mix} profile (5.10)-(5.10) (solid lines) and a flat D_{mix} profile (dashed lines).

5.2.3 General Considerations

In the preceding sections, we discussed the effects of different mixing prescriptions, including a parametric profile, a flat D_{mix} profile, and solely diffusive overshooting. These prescriptions were calibrated to match the mixing levels in the reference rotating GENEC models. The key distinctions among these prescriptions lie in the relative efficiency of near-core mixing and extended mixing in the envelope. This discrepancy is particularly noticeable in the degree of surface nitrogen enrichment, denoted as $[N/H]$ (a signature of CNO-processed material).

Fig. 5.11 compares the $[N/H]$ variation at the initial QCHeB stage with respect to its initial value for 2.0 $M_\odot$ models under the three different mixing prescriptions, as a function of $\Omega_{ini}/\Omega_{crit}$. The figure clearly illustrates that the parametric D_{mix} profile, which we adopt as the effective profile for capturing rotational mixing effects, leads to a more substantial increase in $[N/H]$ during the initial QCHeB phase due to its greater efficiency in envelope-wide mixing. Another interesting aspect to investigate is how these
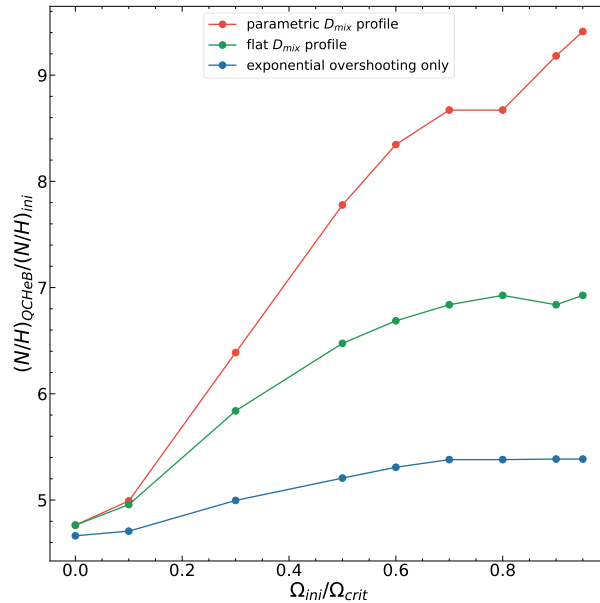
Figure 5.11: $[N/H]$ variation at the initial QCHeB stage with respect to its initial value for 2.0 $M_\odot$ models under the three different mixing prescriptions, as a function of $\Omega_{ini}/\Omega_{crit}$.

mixing processes influence the position of the transition, denoted as M_{Hef}, which separates stars that ignite helium in a degenerate core from those in a weakly or non-degenerate core. It can be anticipated that increasing near-core mixing levels may shift M_{Hef} to lower masses. This is because, for a given star mass, a more efficient near-core mixing will render the core at the Terminal Age Main Sequence (TAMS) similar to that of a higher-mass star. The envelope mixing, on the other hand, would affect the luminosity of stars at the transition.

In Fig. 5.12, various properties are plotted as functions of the mass of the star at the QCHeB phase (at the clump), denoted as M_{cl}. It is evident that rotational mixing (under the assumption of the parametric D_{mix} profile) shifts the transition, represented by the dip in core mass, luminosity, or radius at the clump, to lower masses and higher luminosities. This effect saturates typically around $\Omega_{ini}/\Omega_{crit} \simeq 0.5$. Such plots provide valuable tools for predicting the properties of extended clumps, as discussed in Section 5.3. In Fig. 5.13, a similar plot is presented, but with only diffusive overshooting as an additional mixing process. Here, the effect is to move the transition to lower masses while leaving its luminosity unchanged, as there is no supplementary mixing in the envelope to elevate its mean molecular weight (μ).
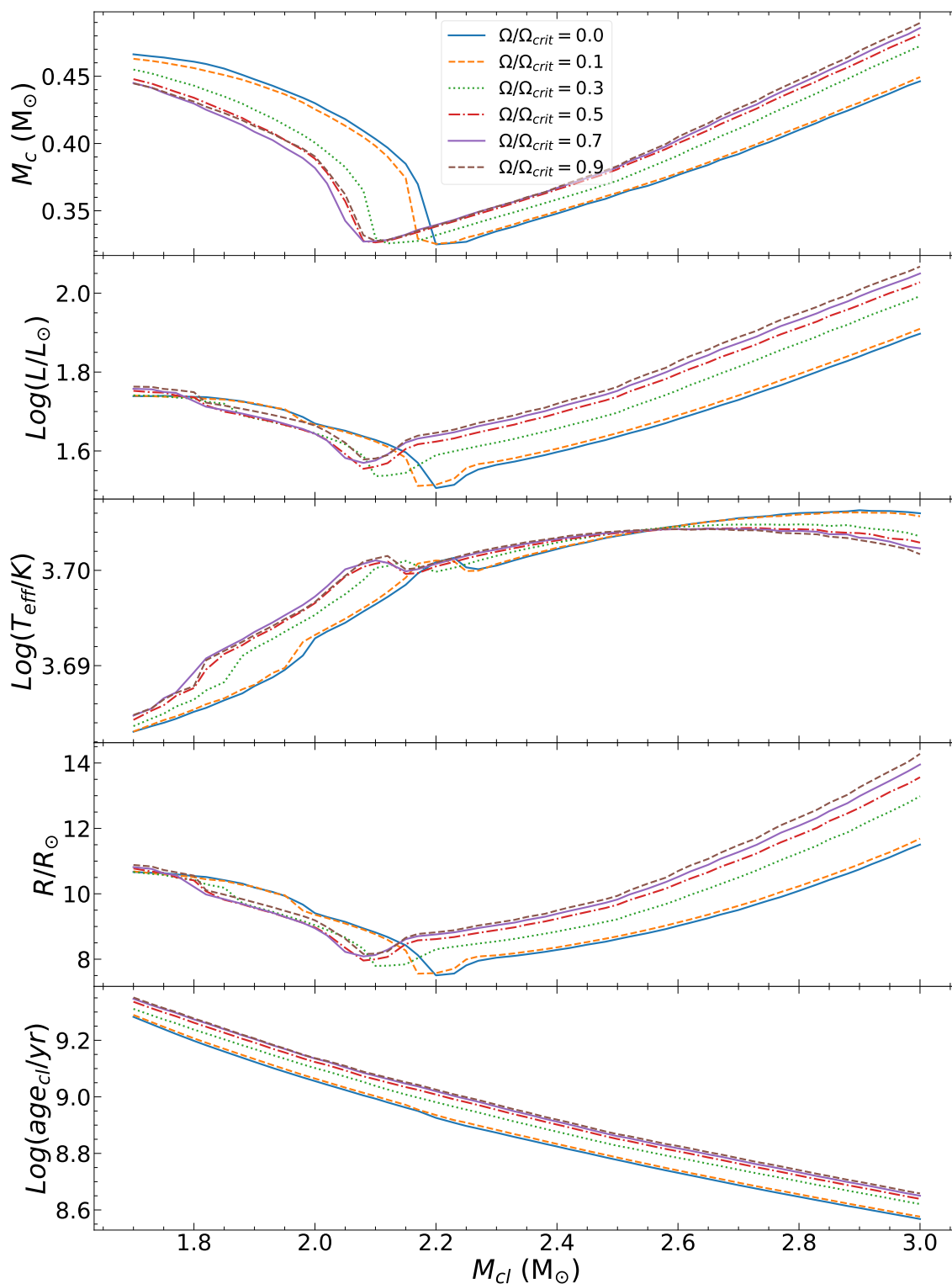
Figure 5.12: Various properties as functions of the mass of the star at the QCHeB phase (at the clump), denoted as M_{cl} for different values of $\Omega_{ini}/\Omega_{crit}$.
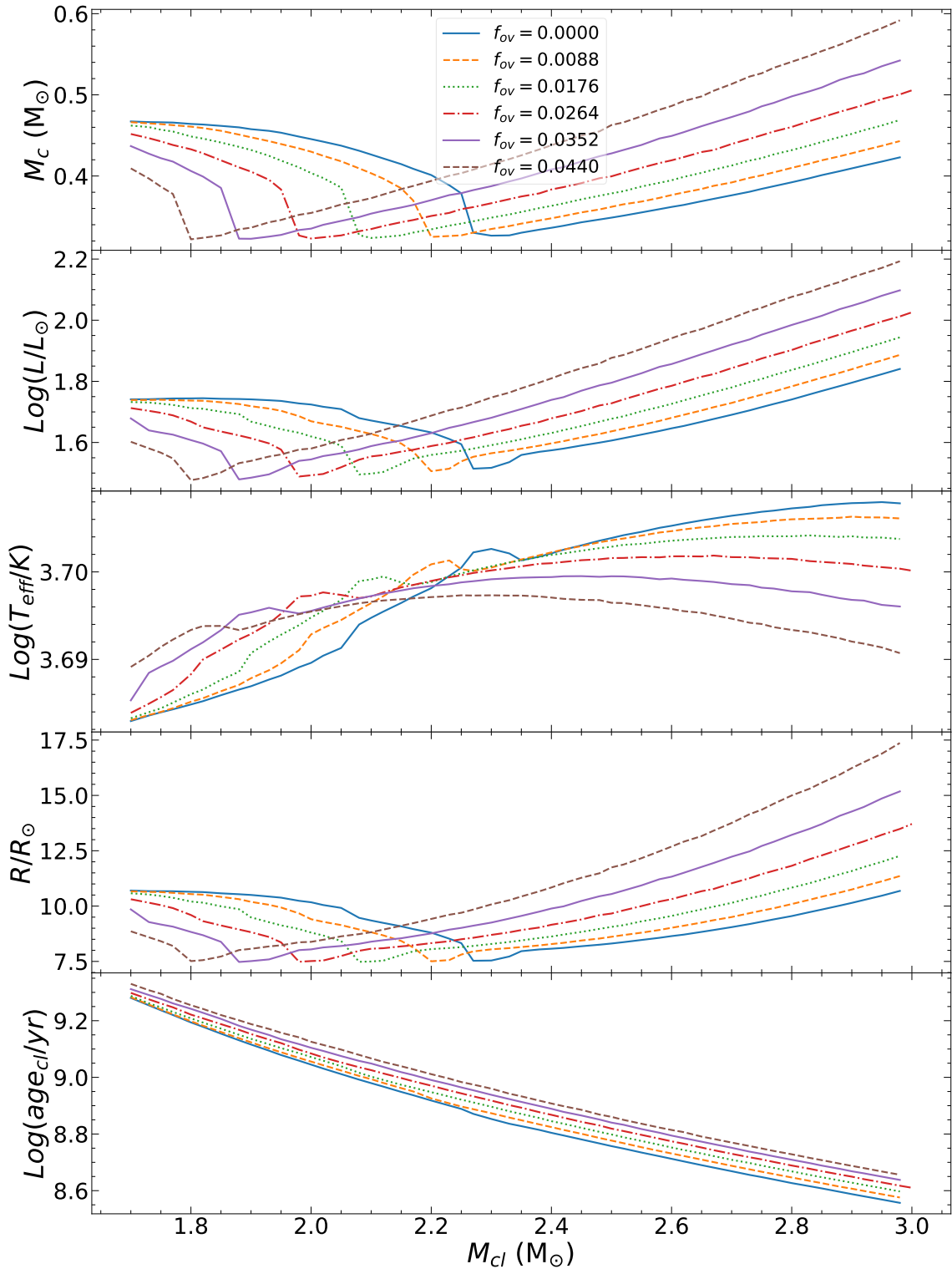
Figure 5.13: Various properties as functions of the mass of the star at the QCHeB phase (at the clump), denoted as M_{cl} for different values of diffusive overshooting parameter f_{ov}.

5.3 Impact of Rotational Mixing on Synthetic Stellar Populations

Given the potential of resolved stellar population studies in uncovering and constraining processes influencing stellar evolution, we computed synthetic Simple Stellar Populations (SSPs) from our grid of MESA calibrated models, incorporating varying distributions of initial rotation. A Simple Stellar Population (SSP) represents the most fundamental population of stars, comprising objects born at the same time during a burst of star formation activity with negligible duration and sharing the same initial chemical composition. Even in an SSP, which finds its most precise manifestation in globular and open clusters, it is reasonable to anticipate that the tumultuous and chaotic processes occurring during star formation can yield a spread in initial rotation velocities. As detailed in preceding chapters, different initial rotation rates can profoundly influence the evolutionary characteristics of stars. Consequently, we expect that an extended distribution of initial velocities within an SSP can generate significant effects on their HR diagrams and other properties.

To compute SSPs with varying distributions of initial rotation, we employed SYCLIST (SYnthetic CLusters, Isochrones, and Stellar Tracks), as described in Georgy et al. 2014b. SYCLIST was designed to generate single-aged stellar populations based on small grids of GENEC models, similar to the reference grid we used. To achieve this, we developed an interface to transform the output data from the grid of MESA models into the same format as the GENEC model grids, facilitating the incorporation of our grid into SYCLIST.

We computed a series of Gaussian and bimodal distributions of $\Omega_{ini}/\Omega_{crit}$, varying the combinations of medians and widths. We opted for bimodal distributions, not only to explore a broader range of possibilities but also due to evidence of bimodal distributions in angular velocities of late B and early A-type main-sequence stars, which serve as progenitors of secondary clump stars (as discussed in Royer et al. 2007). Such bimodal distributions could potentially result in bimodal characteristics within SSP properties.

On top of the SSP outputs, we introduced random fluctuations to quantities such as luminosity (L), effective temperature (T_{eff}), mass (M), surface abundances ($[C/N]$ and $[N/H]$), and radius (R). These fluctuations were drawn from Gaussian distributions with standard deviations equal in magnitude to the observational errors associated with currently operational instruments. This was done to investigate the predicted features that could potentially be observable. Specifically, the error values were extracted from the catalog of Willett et al. (in preparation), encompassing asteroseismic parameters from the pipelines of Mosser and Appourchaux 2009 and Elsworth et al. 2020, as well as spectroscopically derived abundances from APOGEE DR17 (Abdurro'uf et al. 2022), and five-parameter astrometric solutions from Gaia DR3 (Gaia Collaboration et al. 2023).

While we computed an extensive array of SSPs, encompassing all conceivable combi-

nations of $\Omega_{ini}/\Omega_{crit}$ distributions, we discovered that we could accurately describe all the significant features with a few representative cases, which we elaborate on in the following sections.

5.3.1 Stellar Populations with Extended Red Clumps

From the previous discussion in section 2.2.4, it becomes apparent that the occurrence of dual or extended red clumps should be a widespread phenomenon within galaxy fields encompassing stars of all initial masses (ages). This holds true as long as these distinct features in the color-magnitude diagram (CMD) remain unaffected by factors such as differential reddening[4], errors in photometric measurements, and variations in metallicity (Girardi 1999). Indeed, striking examples of faint secondary clumps are provided in the Hipparcos solar-neighbourhood CMD (Girardi et al. 1998) and by the CMDs of some outer Large Magellanic Cloud (LMC) fields (Bica et al. 1998; Piatti et al. 1998). Conversely, it is evident that the existence of dual red clumps was not anticipated within individual star clusters. This is due to the fact that, in the case of a single-age cluster, the variation in turnoff masses is practically negligible and significantly smaller than the approximately 0.2 $M_\odot$ necessary to account for the existence of dual red clumps (Girardi et al. 2000). A few star clusters in the Magellanic Clouds exhibit composite structures in the red-clump region of their colour–magnitude diagrams. There are also indications, despite still to be verified, of galactic star clusters with extended red-clumps, for instance NGC 1817 and NGC 6811 (Sandquist et al. 2020), and several others with confirmed 2RC stars. An exceptional example is observed in NGC 419, an intermediate-age star cluster ($t \approx 1.5$ Gyr) situated in the Small Magellanic Cloud (SMC), where the red clump exhibits a primary clump and a separate, identifiable secondary component, see Girardi et al. 2009 and Dresbach et al. 2023. It is established that this configuration is genuine and represents the coexistence of stars that underwent electron degeneracy after the depletion of central hydrogen and those that did not undergo this process.

The usual explanation for the existence of extended red clumps in clusters is based on the idea of prolonged periods of star formation, as outlined by Girardi et al. 2000, Girardi et al. 2009 and Girardi et al. 2010, that allow a variation in mass necessary to account for the existence of dual red clumps. As highlighted in previous studies, the presence of extended red clumps may be attributed to variations in helium content, CNO element abundances, or overshooting efficiency among populations. While these possibilities should not be dismissed and must be considered in future research, they represent more complex alternatives when compared to the straightforward explanation of prolonged

---

[4]Differential reddening is the non-uniform extinction of starlight by interstellar dust along a line of sight. It leads to variations in the observed colors and magnitudes of stars. Understanding and quantifying differential reddening is crucial for accurate astrophysical investigations.

periods of star formation. If these factors are assumed to be at play, then they should be elucidated in terms of alternative physical processes. Another plausible explanation, which, in our view, falls within the category of straightforward explanations for the existence of extended red clumps in clusters, has not been extensively investigated previously, but was suggested for further exploration by Girardi et al. 2009. This explanation pertains to a spread in rotation rates during the main sequence (MS) evolution of stars in the cluster, specifically in their initial rotation rates. It is reasonable to assume that even within a single-aged cluster, the chaotic and turbulent processes during star formation can result in a range of initial rotation velocities. Other authors (Girardi et al. 2009) already emphasized the importance of clarifying whether rotation can induce the slight variation in core mass at the end of the main sequence necessary to account for the extended red clump phenomenon. In other words, differences in rotation velocities during the main sequence must directly influence the mass of hydrogen-exhausted cores. In support of this hypothesis, we draw attention to a recent spectroscopic investigation of the cluster NGC 419 turn-off stars conducted by Kamann et al. 2018. Their study identified variations in the rotational velocity values between bluer and redder stars within the extended turn-off. Furthermore, Wu et al. 2016 proposed that the morphology of the NGC 419 subgiant branch does not align with the notion of an internal age spread, but rather suggests that the rotation scenario could provide a more plausible explanation. Moreover Dresbach et al. 2023 shows that there is no significant difference in the level of radial segregation of stars populating different regions of the extended red clump and turn-off featres in NGC 419, which would exclude the age spread scenario.

As demonstrated in the preceding sections, our findings affirmatively indicate that a distribution of initial rotation rates (assuming the validity of the rotational model) can induce a significant variation in core mass at the end of the MS and, as shown in the following paragraphs, give rise to extended red clumps within single-age clusters. We found that, with a spread in initial rotation rates Ω/Ω_{crit} comparable to the one given by a gaussian distribution with a standard deviation $\sigma = 0.1$, we have the appearance of an extended red clump in the age range $8.700 < Log_{10}(t/yr) < 9.200$ (0.50 Gyr $< t <$ 1.58 Gyr). Figure 5.14 illustrates a series of diagrams displaying the density of stars in the HRD for single-age synthetic clusters containing 10^5 stars, with ages at $Log_{10}(t/yr) =$ 8.700, 8.850, 9.040, and 9.200, all at solar metallicity and featuring a Gaussian distribution of $\Omega_{ini}/\Omega_{crit}$ centered at 0.2, with a standard deviation of $\sigma = 0.1$.

(a) $Log_{10}(t/yr) = 8.700$.

(b) $Log_{10}(t/yr) = 8.850$

(c) $Log_{10}(t/yr) = 9.040$

(d) $Log_{10}(t/yr) = 9.200$
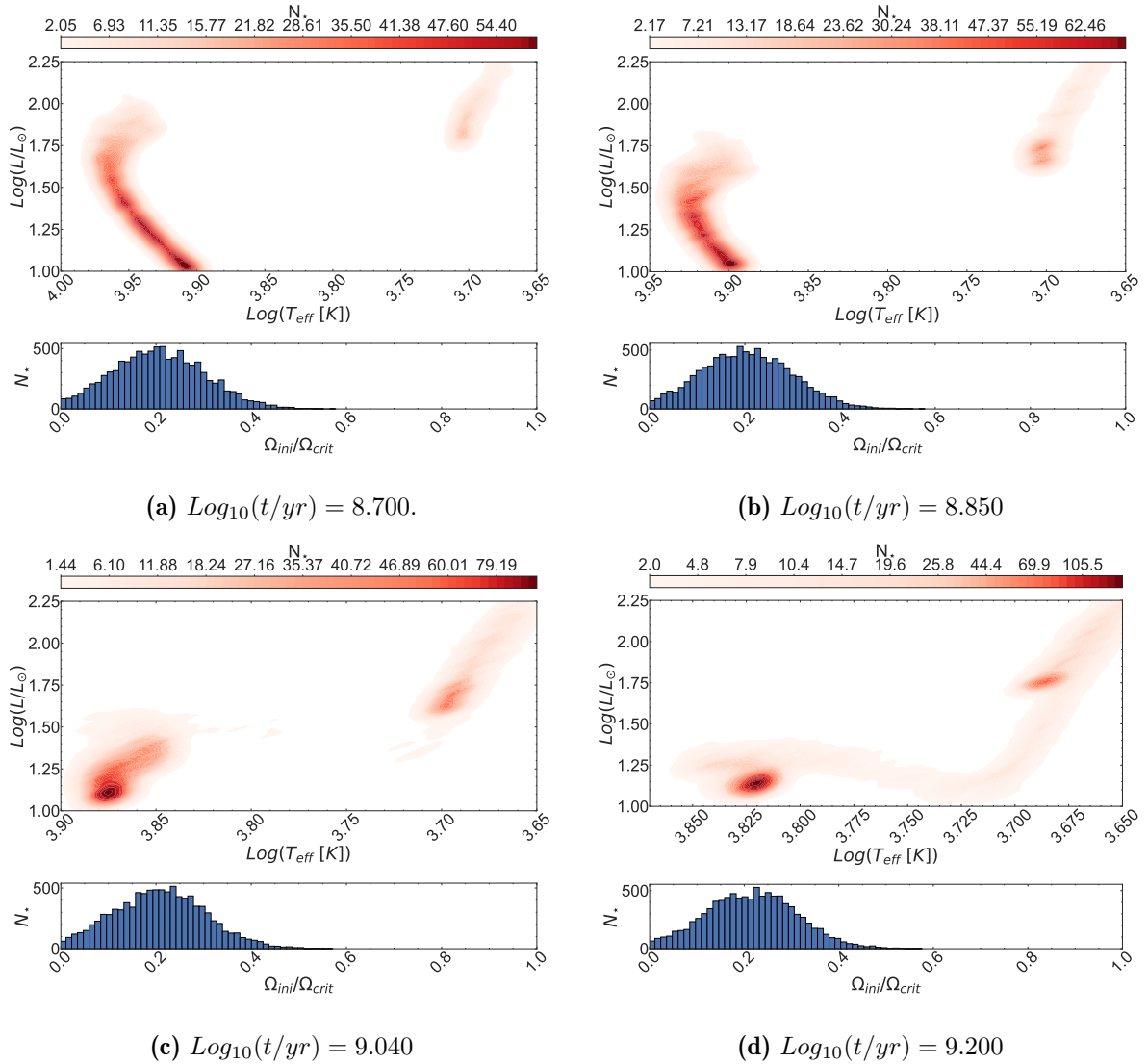
Figure 5.14: Density of stars in the HRD for single-age synthetic clusters containing 10^5 stars, with different ages, Salpeter IMF, all at solar metallicity and featuring a Gaussian distribution of $\Omega_{ini}/\Omega_{crit}$ centered at 0.2, with a standard deviation of $\sigma = 0.1$.

This way of plotting enables us to pinpoint the regions within the HRD that we expect to be statistically more populated. As depicted in Figure 5.14a, there is no prominent clump structure apparent in the HR diagram for ages up to approximately $Log_{10}(t/yr) \approx 8.700$ (corresponding to $t \approx 0.50$ Gyr). This absence of structure arises because He-burning objects within single-age clusters younger than this threshold age exhibit progressively larger loops towards the blue. For older ages, specifically at $Log_{10}(t/yr) = 8.850$ and 9.040, as shown in Figures 5.14b and 5.23a respectively, a dual/extended red clump becomes clearly discernible. However, this extended red clump configuration transitions into a single red clump starting from $Log_{10}(t/yr) = 9.200$ (equivalent to $t \approx 1.58$ Gyr) and continues for older ages. In clusters with ages exceeding

$Log_{10}(t/yr) = 9.200$, He-burning objects have all undergone He ignition within a degenerate environment. Consequently, the size of the He core, which governs luminosity, becomes nearly independent of the core mass at the conclusion of the MS, and this originates a regular/single red clump irrespectively of the spread in the size of the He cores at the end of the MS. The age span within which we observe the emergence of an extended red clump aligns with the age ranges reported by other researchers who documented extended red clumps in the context of clusters undergoing prolonged star formation. For instance, referring to works such as Girardi et al. 2000 and Girardi et al. 2009.

Now, we delve deeper into the characteristics of these dual/extended red clumps. The two scenarios depicted in Figures 5.14b and 5.23a serve as examples representing distinct regimes within the age range where dual or extended red clumps are observed. While a cursory examination of their positions in the HR diagram may suggest similarities, except for the fact that the two clumps in Figure 5.14b are nearly at the same temperature, whereas the dimmer clump in Figure 5.23a is hotter than the brighter one, a more detailed analysis of the stars populating them reveals that they possess contrasting properties. For simplicity we will call the case depicted in Figure 5.14b *young extended clump (YEC)*, while the case depicted in Figure 5.23a as *old extended clump (OEC)*.
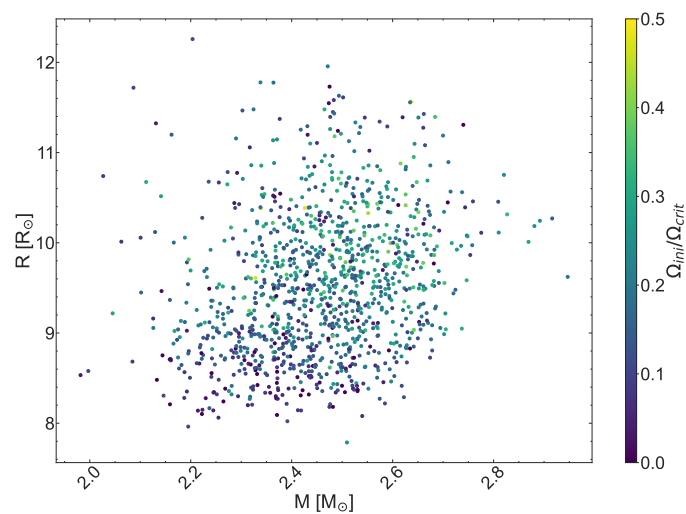
5.3.2   Young Extended Clump (YEC)

In Figure 5.15, we present a detailed view of the extended clump observed in the YEC scenario of Figure 5.14b. The left side displays a luminosity histogram, while the right side shows individual stars superimposed on the density plot, color-coded according to their $\Omega_{ini}/\Omega_{crit}$ values. It becomes evident that, on average, the brighter clump is predominantly populated by stars with higher initial rotation rates, whereas the dimmer clump primarily consists of stars with lower initial rotation rates. There is notable contamination of non-rotating (or very slowly rotating) stars in the brighter clump, which can be readily explained by the presence of slightly more massive stars in a slightly more advanced evolutionary stage, leading to increased luminosity. This configuration aligns with the predictions derived from the plot in Figure 5.12. Specifically, by examining the bottom panel, one can identify the approximate mass at the red clump (M_{cl}) at $\log_{10}(t/yr) = 8.850$ for different $\Omega_{ini}/\Omega_{crit}$ values by locating the intersection of the horizontal line at $\log_{10}(t/yr) = 8.850$ with various curves corresponding to different $\Omega_{ini}/\Omega_{crit}$ values. Once we determine the mass at the red clump (M_{cl}) at $\log_{10}(t/yr) = 8.850$ for different $\Omega_{ini}/\Omega_{crit}$ values, we can subsequently infer the luminosity, as shown in the second panel from the top. Notably, the luminosity of stars in the red clump with higher $\Omega_{ini}/\Omega_{crit}$ values is greater than that of stars with lower $\Omega_{ini}/\Omega_{crit}$ values. Regarding radii, a discernible pattern emerges: on average, stars characterized by higher $\Omega_{ini}/\Omega_{crit}$ values
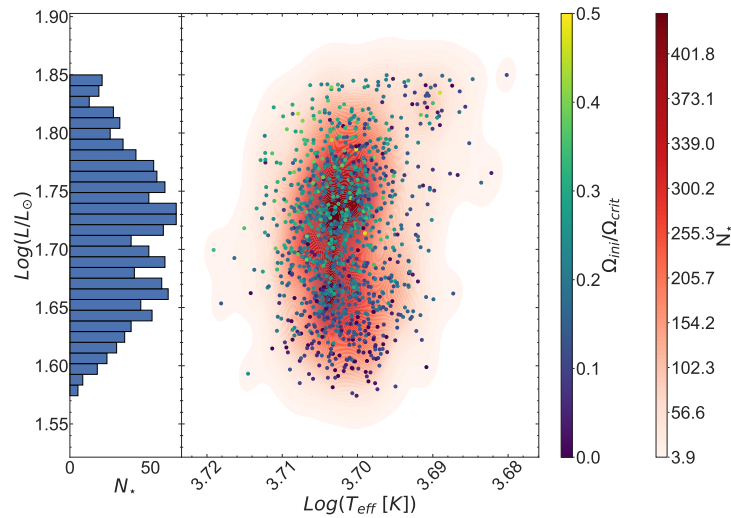
Figure 5.15: Focus on the extended clump observed in the young extended clump scenario depicted in Figure 5.14b. The left panel displays the luminosity histogram of the extended clump. The right panel showcases the density plot with single stars superimposed, color-coded according to the value of $\Omega_{ini}/\Omega_{crit}$.

(which predominantly populate the brighter clump) exhibit larger radii. Regarding stellar masses, while one might expect to observe a trend in which stars with higher $\Omega_{ini}/\Omega_{crit}$ values exhibit slightly larger masses, this trend does not appear to be distinguishable in Fig.5.16. It's important to consider that on top of these modelled data we added observational errors typical of current observations (taken from Willet et al. in preparation, including data from *Kepler*, APOGEE DR17, Gaia DR3), and the margin of error on mass measurements can be significant enough to obscure any discernible trend. One of the most

Figure 5.16: Radius vs mass of the young extended clump sample of Fig. 5.15, colored according to initial rotation.

interesting characteristics is the gradient in the ratio of surface carbon and nitrogen abundances, denoted as $[C/N]$. As elucidated in preceding sections, we anticipate that this parameter would be influenced by rotational mixing as it brings CNO-processed material to the surface. More specifically, we would expect a smaller $[C/N]$ value for stars with higher $\Omega_{ini}/\Omega_{crit}$ values. This trend is distinctly evident in Figure 5.17. Consequently, given that the brighter clump primarily consists of stars with higher initial rotation rates, while the dimmer clump is predominantly populated by stars with lower initial rotation rates, we anticipate observing a gradient in $[C/N]$, specifically, a decrease in this parameter from the brighter to the dimmer clump if a spread in rotation rates is responsible for the extended clump.

This particular characteristic holds the potential to differentiate between the influence of rotation and alternative factors, such as protracted phases of star formation, variations in metallicity, or variations in the efficiency of convective core overshooting, all of which can contribute to the existence of extended clumps. The distinction essentially hinges on how profoundly these alternative processes can impact the surface $[C/N]$ value at the red clump. For instance, we can confidently assert that different levels of overshooting efficiency are incapable of generating such a pronounced spread in $[C/N]$. This assertion is substantiated by the observation that, as depicted in Fig. 5.7b, varying overshooting primarily affects the core size, while the slight increase in μ in the envelope, stemming from the transport of material processed by the CNO cycle to the surface, is practically negligible. In the case of other potential mechanisms for producing extended clumps, additional factors may be at play, exerting influence on $[C/N]$. Investigating these intricacies will be a pivotal focus in the ongoing phases of this research.
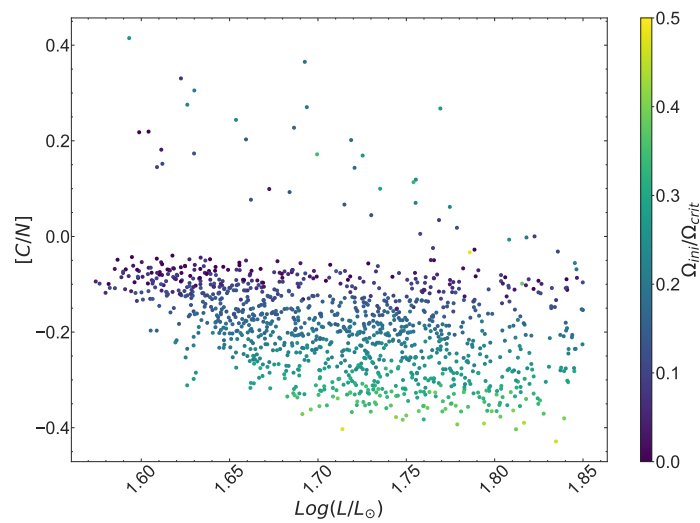
Figure 5.17: $[C/N]$ vs $Log(L/L_\odot)$ of the young extended clump sample of Fig. 5.15, colored according to initial rotation.
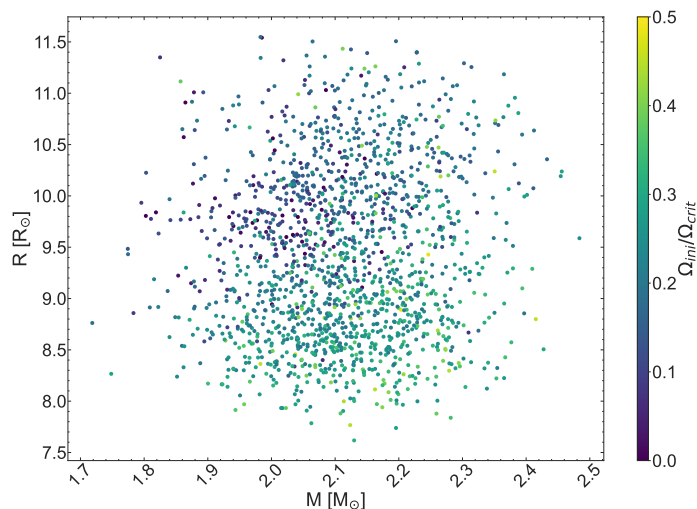
5.3.3   Old Extended Clump (OEC)

In Figure 5.18, we present a detailed view of the extended clump observed in the OEC scenario of Figure 5.14b. In this scenario, the dual clump properties are the inverse of
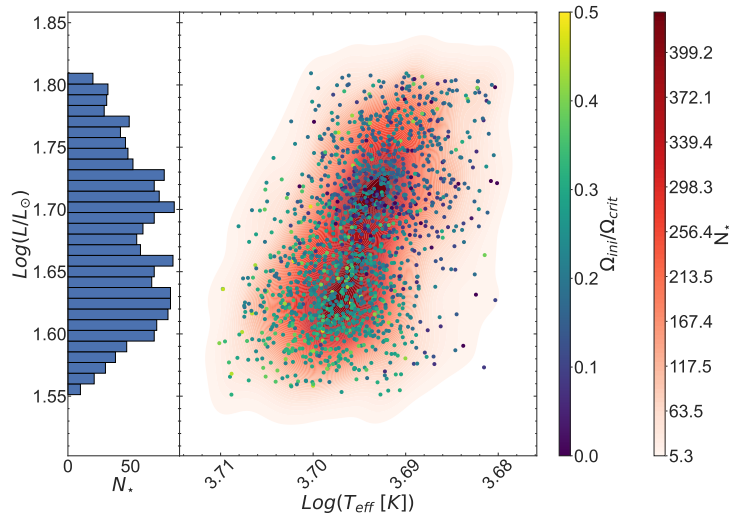
Figure 5.18: Focus on the extended clump observed in the old extended clump scenario depicted in Figure 5.23a. The left panel displays the luminosity histogram of the extended clump. The right panel showcases the density plot with single stars superimposed, color-coded according to the value of $\Omega_{ini}/\Omega_{crit}$.

those observed in the previous one. On average, the brighter clump is primarily composed of stars with lower initial rotation rates, while the dimmer clump consists mainly of stars with higher initial rotation rates. There is noticeable contamination of faster-rotating stars within the brighter clump, which can once more be explained by the presence of slightly more massive stars in a slightly more advanced evolutionary stage, resulting in increased luminosity. Following the same methodology as the previous case, this configuration aligns with the predictions obtained from the plot in Figure 5.12.

Concerning radii, an inverse pattern emerges compared to the previous case: on average, stars characterized by higher $\Omega_{ini}/\Omega_{crit}$ values (which predominantly populate the brighter clump) exhibit smaller radii. Regarding masses, we should expect the same trend; however, this trend is obscured by substantial uncertainties. The gradient in $[C/N]$ is opposite with respect to the previous case. As before we expect a smaller $[C/N]$ value for stars with higher $\Omega_{ini}/\Omega_{crit}$ values. This trend is distinctly evident in Figure 5.17. However, since in this case the brighter clump primarily consists of stars with lower initial rotation rates, while the dimmer clump is predominantly populated by stars with higher initial rotation rates, we anticipate observing an opposite gradient in $[C/N]$, specifically, an increase in this parameter from the brighter to the dimmer clump if a spread in ro-

Figure 5.19: Radius vs mass of the old extended clump sample of Fig. 5.18, colored according to initial rotation.

tation rates is responsible for the extended clump. This reversal in the characteristics
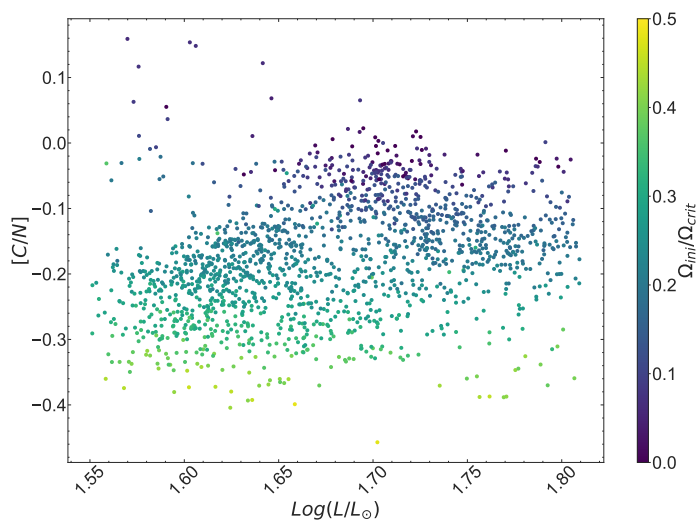
Figure 5.20: [C/N] vs $Log(L/L_\odot)$ of the old extended clump sample of Fig.5.18, colored according to initial rotation.

of the extended clumps is clearly evident in Figure 5.12 and is a reflection of sampling different sides of the transition (corresponding to the minimum in core mass at the clump) at varying ages.

If these characteristics of the extended clumps could be validated in actual clusters, it would not only serve to confirm that one possible origin of extended clumps could be

a spread in initial rotation rates but also provide stringent constraints on the efficiency of rotational mixing (and more broadly, near-core and envelope mixing). Additionally, it would have implications for our models of rotation in stars. Furthermore, it would impose rigorous constraints on the age determination of the clusters, contingent on which configuration of the clump is being observed, be it the young extended clump or the old extended clump.

5.3.4   Impact of Different Distributions of Initial Rotation Rates

In the examples shown in the previous paragraphs, we used a single distribution of initial rotation rates, in particular a Gaussian distribution of $\Omega_{ini}/\Omega_{crit}$ centered at 0.2, with a standard deviation of $\sigma = 0.1$. This choice wasn't random, in fact the range of rotation rates covered by this distribution (from 0.0 to 0.5 $\Omega_{ini}/\Omega_{crit}$) is the range in which the impact of different $\Omega_{ini}/\Omega_{crit}$ is larger. As discussed in Section 4 and as clearly visible from Fig. 5.12, the effects of rotation saturates around $\Omega_{ini}/\Omega_{crit} \approx 0.5$, so we have that by increasing $\Omega_{ini}/\Omega_{crit}$ furtherdoes not impact the prediction significantly. This is evident in Fig. 5.23 where it is clear that for Gaussian distributions of $\Omega_{ini}/\Omega_{crit}$ with the same σ but centerd at higher values of Gaussian distribution of $\Omega_{ini}/\Omega_{crit}$ the clump is very close to a normal single clump.

Moreover it is of interest to check wether a bimodal distribution has an appreciable impact on the properties of the extended clumps, because, if this is the case, we could have a potential method to discriminate between unimodal and bimodal distributions of initial rotation rates. Unfortunately, as shown in Fig. 5.23c at least from the morphology of the clumps in the HR diagram the only difference is a slightly more defined duality in the double clump feature, but definitely not enough to safely discriminate between an unimodal or a bimodal distribution covering the same range of $\Omega_{ini}/\Omega_{crit}$. The reason of this is that the duality in the red clump originates from the transition in the properties shown in Fig. 5.12, which is relatively sharp by itself, and it can arise even with a smooth distribution of $\Omega_{ini}/\Omega_{crit}$ provided that it sample the range of the transition at a given age. Although the shape of the initial rotation distribution cannot be studied solely from the clump's morphology in the HR diagram, the same cannot be said for $[C/N]$, which provides a closer reflection of the $\Omega_{ini}/\Omega_{crit}$ distribution. In Fig. 5.21, we present a detailed view of the extended clump with the bimodal distribution observed in the old extended clump scenario depicted in Figure 5.23c, and it becomes evident that there is minimal difference compared to the old extended red clump scenario with the Gaussian distribution in Fig. 5.18. Fig.5.22 shows $[C/N]$ vs. $Log(L/L_\odot)$ for the case of bimodal distribution in Fig.5.23c, here the bimodality in terms of $[C/N]$ is clear. Therefore, assuming that our models are accurate and that no factors other than rotation
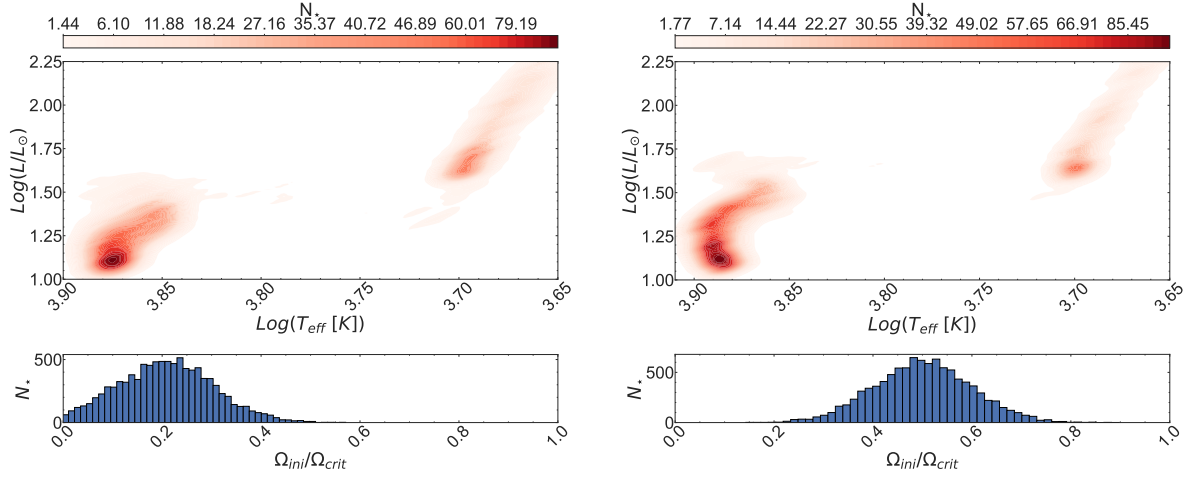
(a) Gaussian distribution of $\Omega_{ini}/\Omega_{crit}$ centered at 0.2, with a standard deviation of $\sigma = 0.1$.

(b) Gaussian distribution of $\Omega_{ini}/\Omega_{crit}$ centered at 0.5, with a standard deviation of $\sigma = 0.1$.
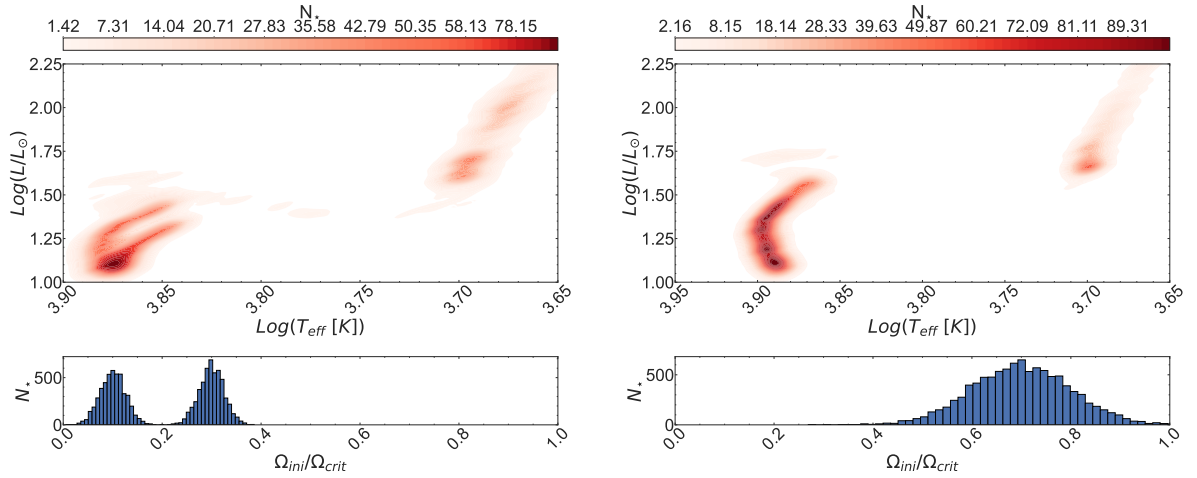
(c) Double Gaussian of $\Omega_{ini}/\Omega_{crit}$ centered at 0.1 and 0.3, with a standard deviation of $\sigma = 0.025$.

(d) Gaussian distribution of $\Omega_{ini}/\Omega_{crit}$ centered at 0.7, and a standard deviation of $\sigma = 0.1$.

Figure 5.23: Density of stars in the HRD for single-age synthetic clusters containing 10^5 stars, with an age of $\log_{10}(t/yr) = 9.040$, Salpeter IMF, all at solar metallicity and featuring different distributions of $\Omega_{ini}/\Omega_{crit}$.

and the standard processes considered in our models influence $[C/N]$, we could employ $[C/N]$ measurements to investigate the shape of the initial rotation distribution.
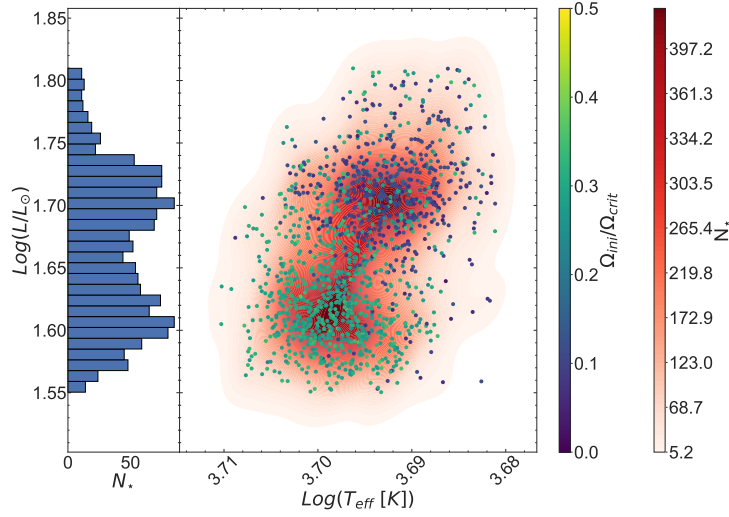
Figure 5.21: Focus on the extended clump observed in the old extended clump scenario with a bimodal distribution depicted in Figure 5.21. The left panel displays the luminosity histogram of the extended clump. The right panel showcases the density plot with single stars superimposed, color-coded according to the value of $\Omega_{ini}/\Omega_{crit}$.
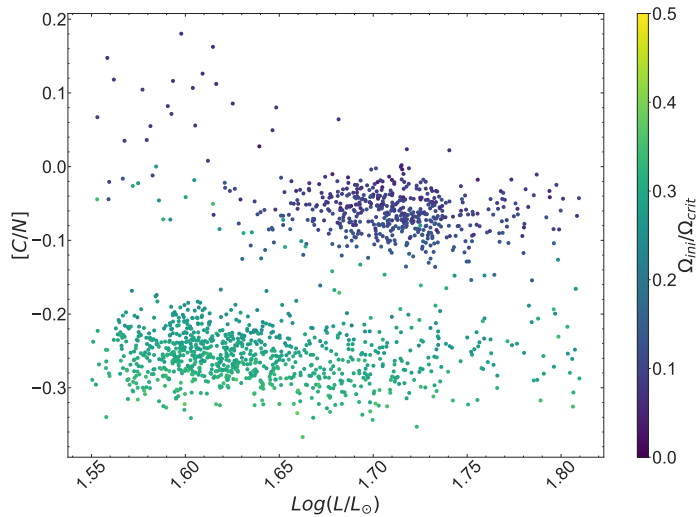
Figure 5.22: $[C/N]$ vs $Log(L/L_\odot)$ of the old extended clump sample of Fig. 5.21, colored according to initial rotation.

5.4 Preliminary Comparison with Observations

Since this aspect of the secondary clump, particularly in these specific terms, has remained relatively unexplored until now, a substantial portion of the work conducted thus far has predominantly involved theoretical modeling. This effort aimed to establish the theoretical framework and construct the necessary tools for initiating investigations into various possibilities and expected outcomes. Nonetheless, even at this point, it is crucial to assess whether we are heading in the right direction. This involves conducting comparisons, albeit not in a systematic manner and without any claim of exhaustiveness, with observational data. A thorough and methodical comparison with observational data is an imperative step, and it will constitute the primary focus of our future endeavors in this research, along with further improvements to the models.

In this section we present a comparison of the properties of red clump stars in our single-age synthetic clusters, characterized by spreads in initial rotation and solar metallicity, with red clump stars from the Galactic field and a selection of Galactic star clusters that share solar metallicity and ages within the range where our models exhibit extended clumps. The galactic field sample comes from the catalogue of Willett et al. (in preparation), which contains asteroseismic parameters from the pipelines of Mosser and Appourchaux 2009 and Elsworth et al. 2020, as well as spectroscopically derived abundances from APOGEE DR17 (Abdurro'uf et al. 2022), and five-parameter astrometric solutions from Gaia DR3 (Gaia Collaboration et al. 2023). Masses for fields stars are obtained using asteroseismic parameters from *Kepler* using the scaling relation 7.9, while radii are obtained from luminosities and temperatures using the Stefan-Boltzmann equation 2.8. The data for the cluster NGC 6866 is taken from Brogaard et al. 2023 while those for NGC 6811 from Sandquist et al. 2016. For this comparison, we adopt distributions of $\Omega_{ini}/\Omega_{crit}$ taken from Royer et al. 2007. In their work, they provide distributions of Ω/Ω_{crit} for late B and early A-type main-sequence field stars in the early MS evolutionary phases, see Fig.5.24. It's worth noting that MS stars with spectral types ranging from B9 to A5 represent the progenitors of secondary clump stars within the mass range considered in this study. We proceed to compute synthetic clusters with ages $Log(t/yr) = 8.700, 8.850, 9.040, 9.200$, assuming the corresponding distribution of Ω/Ω_{crit} based on the mass of the stars in the red clump at a given age. As depicted in Figure 5.27, our synthetic clusters with single-age populations occupy the same regions as observed stars in both field and cluster environments, exhibiting a similar degree of dispersion. Notably, the synthetic clusters with the specified ages encompass the entire transition region between the primary and secondary red clumps (RC1/RC2) near a stellar mass of approximately 2.05 M$_\odot$. Within this mass range, stars belonging to both RC1 and RC2 are present, with the synthetic cluster corresponding to $Log(t) = 9.040$ accommodating 2RC stars with a minimum radius
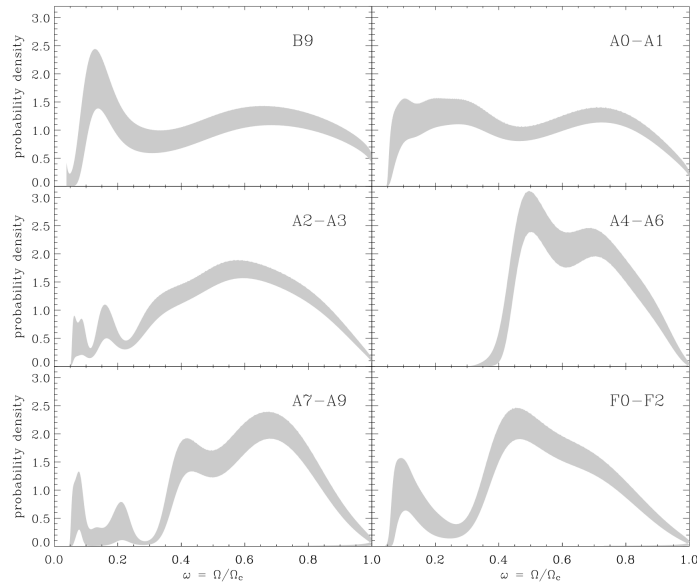
Figure 5.24: Distribution of angular velocity Ω/Ω_{crit} for late B and early A-type main-sequence field stars in the early MS evolutionary phases. Reprouced from Royer et al. 2007.

of approximately 8 $R_{\odot}$. This observation reinforces the notion that the age span explored in this study, assuming initial distributions of $\Omega_{ini}/\Omega_{crit}$ from Royer et al. 2007, results in dual or extended red clumps. The origin of these, in our models can be attributed solely to variations in initial rotation rates. Certainly, in natural scenarios, various factors like age or metallicity spreads can also contribute to the emergence of extended clumps. It is imperative to thoroughly investigate these possibilities and their interactions with the phenomenon of rotational mixing in the subsequent phases of this research.

In section 5.3, we emphasized the significance of the $[N/C]$ ratio in distinguishing the effects of rotation. Therefore, it is crucial to ascertain whether the predictions of our models align with the observed values of this parameter. However, it is worth noting that the quantity $[C/N]$ is recognized in the literature for displaying systematic discrepancies between models and observations. These discrepancies can arise from factors such as overly efficient or insufficient mixing, inaccurate assumptions regarding the initial abundances of C, N, and O, or systematic errors in the APOGEE measurements (as discussed in Vincenzo et al. 2021). It is not within the scope of this study to resolve these "zero-point problems" associated with $[C/N]$. Instead, we restrict ourselves to observing that our models yield $[C/N]$ values within the range of the observed values (refer to Figure 5.26), but we do not draw any absolute conclusion about the values at which the points of the synthetic clusters lies for example in the $M - [C/N]$ plot of Fig.5.26. A more significant observation is that our synthetic clusters are consistent with the observed spread in $[C/N]$, which is not the case for instance for a synthetic cluster with a single value of initial rotation, see Fig.5.27d. This implies that, assuming the validity of our models, the

observed variation in $[C/N]$ among red clump stars in both field and cluster environments can be attributed to the effects of rotational mixing. We do not assert that rotational mixing is the exclusive explanation, as we have not yet thoroughly explored all potential degeneracies. Nevertheless, we suggest that it presents a plausible explanation.

5.5 Future Prospects

Most of the results presented in this work, especially those regarding extended clumps are in a certain sense exploratory, we showed that according to our models rotation-induced mixing can generate double or extended red clumps with specific characteristics, especially the gradient of $[C/N]$ between the two clumps could be a way to discriminate wether the two clumps are generated by a spread in rotation and to put contraints on our rotating models and on the age of the clusters.

However, we already mentioned that several causes other than rotation can contribute to the appearance of double or extended clumps, such as prolonged star formation, metallicity, spreads in He abundance and different efficiencies of convective core overshooting within the same population. In order to get a clear picture we need to carefully explore all these degeneracies and find possible ways in order to break them. This is certainly one of the most important directions of the future development of this work, and it involves the computation and combination of synthetic stellar populations with all the possible combinations of these factors that contribute to the formation of extended clumps.

Another very important aspect that must be carefully explored is the influence of rotation-induced mixing of chemicals and of the other factors that affects secondary clump stars in a similar way on asteroseismic properties. How rotational mixing can affect asteroseismic properties of secondary-clump stars is another possible way of discriminating between the effects of rotation-induced mixing of chemicals and the other factors influencing them in a similar way. Even though we did not have the possibility to expand further on this for now, we can make some observations based on the results we obtained up to now. Examining the μ profiles of our models in Fig. 5.9, we can observe that, as previously noted, during the QCHeB phase, the only discernible signature resulting from the rotational mixing of chemical species is a slight variation in the core size and a modest increase in the μ level within the envelope. The details of the μ profile that could potentially carry indications of specific mixing processes, as seen, for instance, in the TAMS model, are obliterated by the deep penetration of the convective envelope during the red giant phase. Consequently, significant signatures of rotation-induced chemical mixing are not expected. In order to study these signatures we should focus on earlier evolutionary stages where a significant imprint of rotational mixing of chemicals is expected to be visible, see for instance Miglio et al. [2008].

One effect that may be observable within a single-age cluster featuring a spread in initial rotation is related to the mass of the stars. As elaborated in Section 5, the presence of rotation extends the main sequence (MS) duration for a fixed mass, owing to the augmented availability of hydrogen due to near-core mixing induced by rotation. Consequently, within a single-age cluster, a spread in masses may exist at a particular evolutionary stage, which could potentially be detected using asteroseismic methods as those described in Appendix 7.3. However, it should be noted that in our tests, the observed mass differences at the red clump fall within approximately 10%, which is on the order of the accuracy associated with global asteroseismic mass determinations just mentioned. For instance, the scaling relations such as 7.9 for solar-like oscillations in low and intermediate-mass stars typically provides an accuracy of approximately 5%. Nevertheless, more precise methods for mass determinations such as fitting individual oscillation modes (in contrast to solely relying on average quantities like $\Delta\nu$ and ν_{max}), as demonstrated in Montalbán et al. 2021, along with measurements of a variation in surface $[N/C]$, could potentially distinguish between stars that have undergone varying levels of rotational mixing due to differences in their initial rotation rates.

In Fig.5.28, we present the propagation diagrams (refer to Appendix 7.2) for two red clump models with a mass difference on the order of those observed in a single-age synthetic cluster exhibiting a spread in initial rotation rates. In Fig.5.29, we provide propagation diagrams for another pair of red clump models possessing the same mass but differing in initial rotation rates. Propagation diagrams are graphical representations illustrating the two characteristic frequencies that govern the propagation of pulsation modes within stellar interiors: the Lamb frequency S_l and the Brunt-Väisälä frequency N. These diagrams display these frequencies as a function of either radius or mass coordinate, serving to visualize where oscillation modes can propagate and what their character may be, whether pressure modes, gravity modes, or mixed modes. For a brief introduction to these concepts, please refer to Appendix 7.2. It is evident from figures 5.28 and 5.29 that, as expected from the previous considerations, rotational mixing, unlike the mass difference, has almost no impact on the shapes of S_l and N. As a result we do not expect a significant impact on the oscillation frequencies due to chemical gradients induced by rotational mixing in red clump stars, but just an impact due to the different masses determined by the efficiency of mixing during the MS.

Our models are non-rotating models with an additional mixing calibrated to reproduce rotational mixing of chemical elements, so they are not able to reproduce the evolution of the rotation profile, which instead is possible with GENEC models (however, it is currently only possible for GENEC to follow the He burning phase only for masses larger than 2.5 M$_\odot$), but at the current models fail to reproduce the core-rotation rates of red clump stars suggesting the presence of a very efficient unknown angular momentum transport process.

With that being noted, forthcoming models should possess the capability to replicate not only the observed surface rotation, determined through spectroscopic methods but also the internal rotation profiles, which can be derived from the impact of rotation on oscillation modes probing the stellar interior. Indeed, asteroseismic observations of red giant stars led to the determination of internal rotation of these stars, as demonstrated by studies such as Beck et al. 2012, Deheuvels et al. 2015 and Deheuvels et al. 2020.
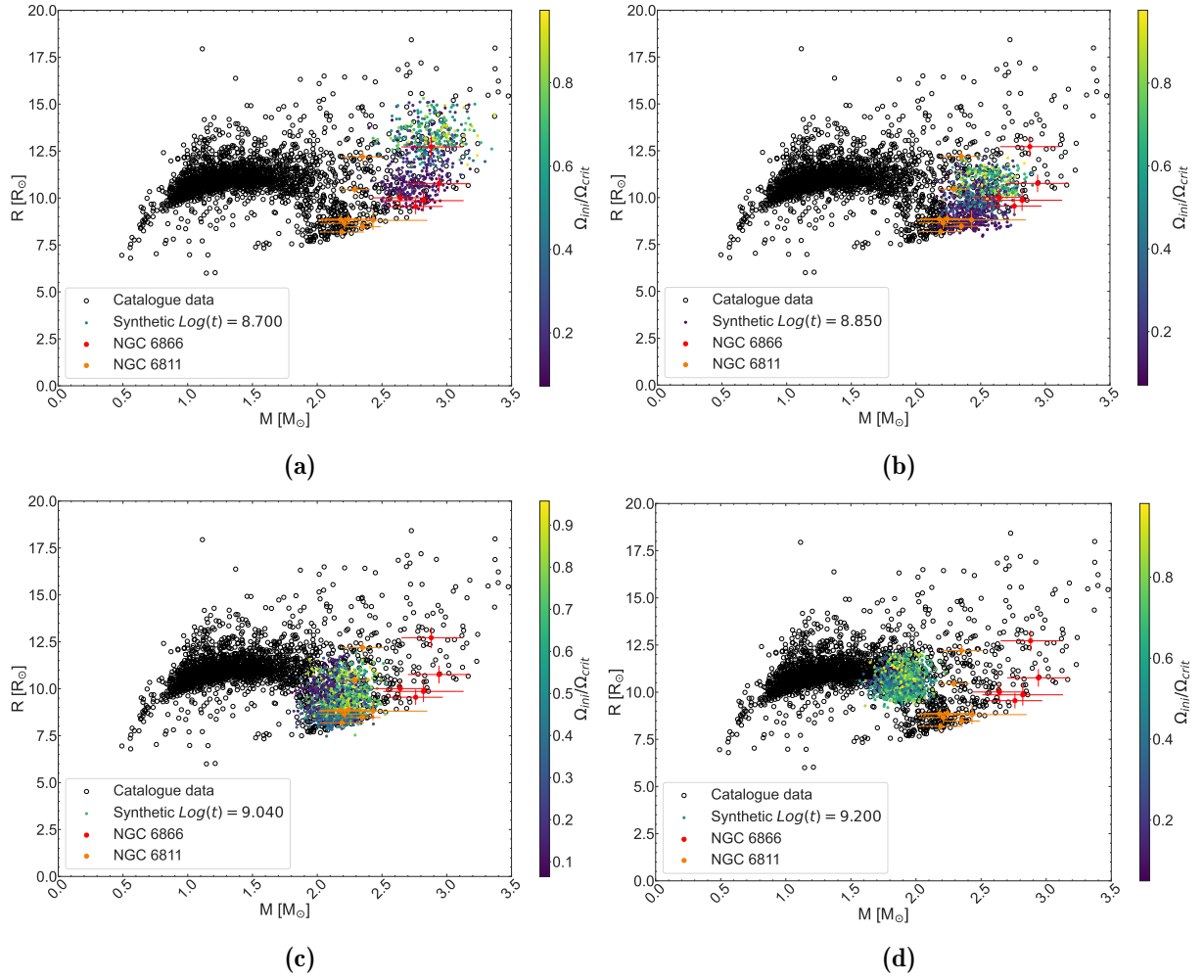
Figure 5.25: Mass and radius (Stefan-Boltzmann equation) measurements for clusters NGC 6866 (Brogaard et al. 2023) and NGC 6811 (Sandquist et al. 2016) as well as field stars with *Kepler* data from Willett et al. (in prep.) with superimposed single-age synthetic clusters having distributions of $\Omega_{ini}/\Omega_{crit}$ taken from Royer et al. 2007 according to the mass of the stars in the clump.
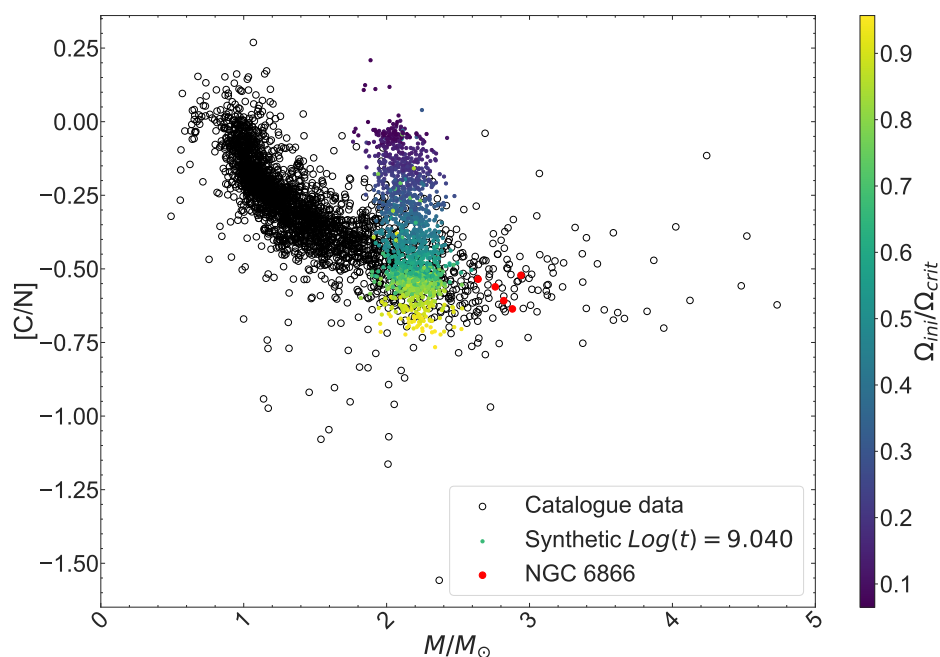
Figure 5.26: Mass M vs $[C/N]$ measurements for clusters NGC6866 (Brogaard et al. 2023) as well as field stars with *Kepler* data from Willett et al. (in prep.) with a superimposed synthetic cluster with $Log(t) = 9.040$ having distributions of $\Omega_{ini}/\Omega_{crit}$ taken from Royer et al. 2007 according to the mass of the stars in the clump. This plot serves the purpose of illustrating that the data points for the synthetic cluster fall within the range of observed values. Nonetheless, it is crucial to acknowledge that inherent systematic errors in $[C/N]$ introduce complexities, and as such, definitive physical conclusions should not be drawn solely from this plot.
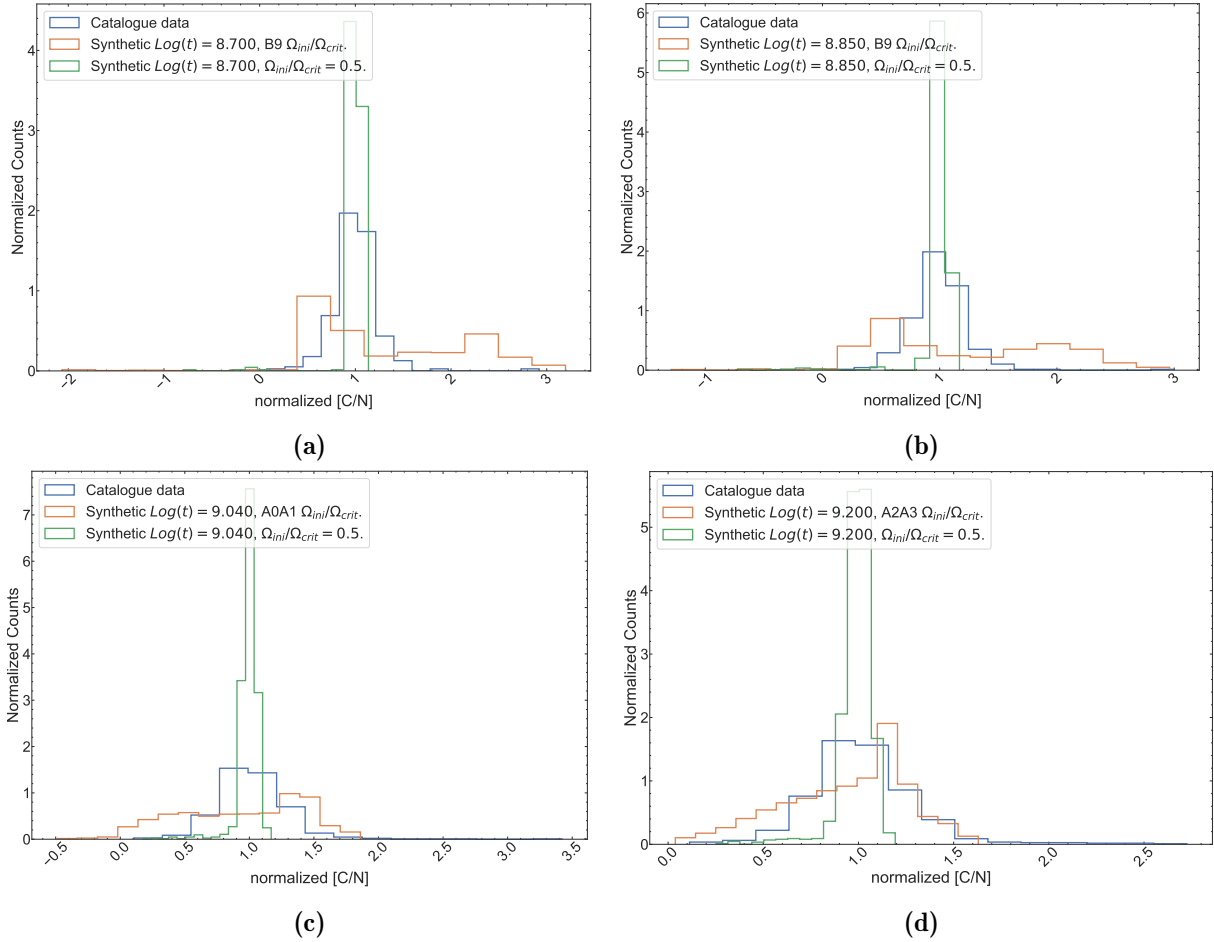
Figure 5.27: Histogram of $[C/N]$ normalized by its median value within the mass range of the red clump stars in the single-age synthetic cluster. Data for the field stars (with *Kepler* data) are taken from Willett et al. (in prep.). The superimposed single-age synthetic clusters have distributions of $\Omega_{ini}/\Omega_{crit}$ taken from Royer et al. 2007 according to the mass of the stars in the clump and a Dirac delta distibrution centered at $\Omega_{ini}/\Omega_{crit} = 0.5$.

(a)

(b)
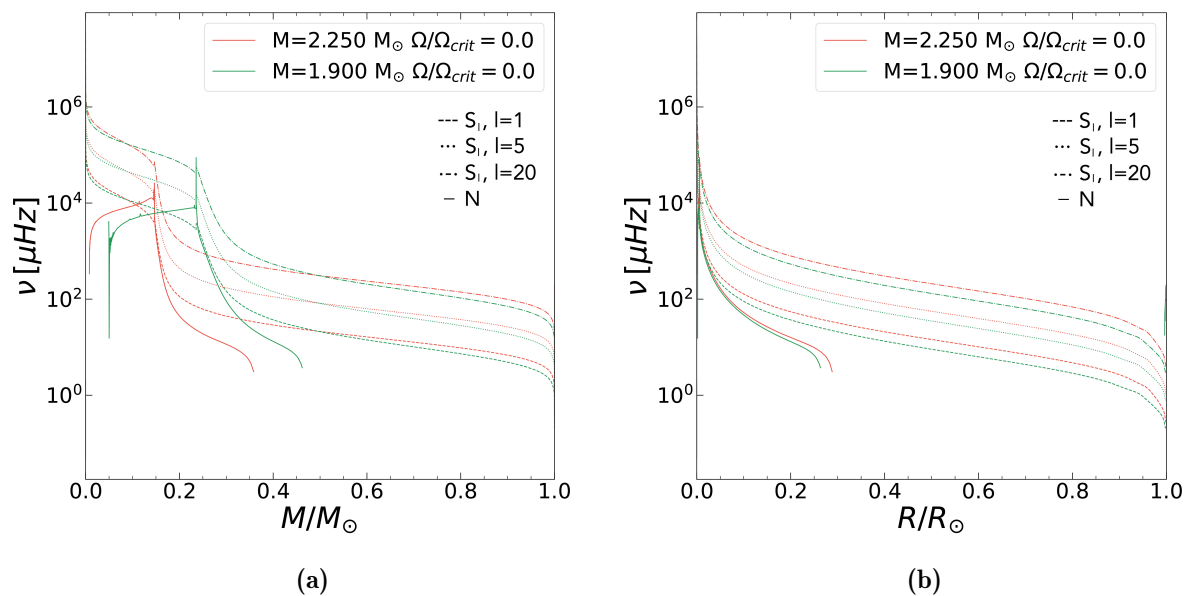
Figure 5.28: Propagation diagrams for two of our MESA models with masses of $M = 2.250$ M$_\odot$ and $M = 1.900$ M$_\odot$ and $\Omega_{ini}/\Omega_{crit} = 0.0$.

(a)

(b)
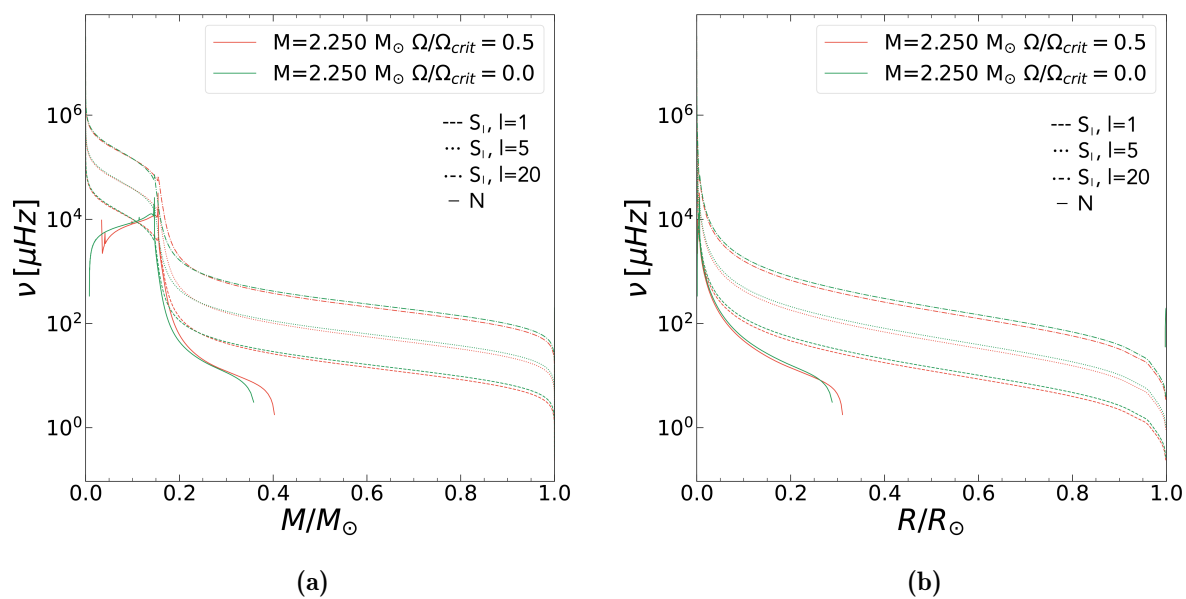
Figure 5.29: Propagation diagrams for two of our MESA models a mass of $M = 2.250$ M$_\odot$ and 0.0 and 0.5 $\Omega_{ini}/\Omega_{crit}$.

Chapter 6

Conclusions

The primary objective of this work was to explore the effects of rotation-induced mixing on secondary clump stars, both as individual stars and within single-age stellar populations. Using models of rotating stars and incorporating them into single-age synthetic stellar populations with varying distributions of initial rotation rates, we found that, assuming the validity of the rotational model, a spread of initial rotation rates can induce substantial variations in core mass at the conclusion of the main sequence. This is due to the mixing induced by rotation and results in the emergence of extended red clumps within single-age clusters. These extended clumps are observable in reality, although their origin remains an open question and may arise from a combination of factors, including differing efficiencies of rotational mixing due to variations in initial rotation rates.

Additionally, we proposed a simple method, leveraging the plot featured in Fig. 5.12, to predict the properties of these extended clumps. Thanks to this method, we recognized that our models predict an inversion in the properties of the extended clumps at a specific age. If this inversion in properties could be confirmed in actual clusters, it would enable precise age determinations.

The preliminary comparison conducted with field and cluster stars validates that our single-age synthetic clusters encompass stars from both the conventional red clump and the secondary clump. In our models, this diversity is achieved solely through a variance in initial rotation rates, determined by distributions of initial rotation derived from observations as presented by Royer et al. 2007. Furthermore, we ascertained that the spread in $[N/C]$ predicted by our synthetic clusters, featuring distributions of initial rotation rates derived from observations, aligns with the observed variability in field stars.

Chapter 7

Appendices

7.1   Expressions of E_Ω^* and E_μ

$$E_\Omega^* = 2\left[1 - \frac{\overline{\Omega^2}}{2\pi G\overline{\rho}} - \frac{\overline{\epsilon} + \overline{\epsilon}_{grav}}{\epsilon_m}\right]\frac{\tilde{g}}{g}$$

$$- \frac{\rho}{\rho_m}\left\{\frac{r}{3}\frac{d}{dr}\left[H_T\frac{d}{dr}\left(\frac{\Theta}{\delta}\right) - \frac{\chi_T}{\delta}\Theta + \Theta\left(1 - \frac{1}{\delta}\right)\right] - \frac{2H_T\Theta}{r\delta} + \frac{2}{3}\Theta\right\}$$

$$- \frac{(\overline{\epsilon} + \overline{\epsilon}_{grav})}{\epsilon_m}\left\{H_T\frac{d}{dr}\left(\frac{\Theta}{\delta}\right) + \frac{\Theta}{\delta}(f_\epsilon\epsilon_T - \chi_T) + \Theta\left(2 - f_\epsilon - \frac{1}{\delta}\right)\right\} - \Theta\frac{\overline{\Omega}^2}{2\pi G\overline{\rho}}. \tag{7.1}$$

$$E_\mu = \frac{\rho_m}{\overline{\rho}}\left\{\frac{r}{3}\frac{d}{dr}\left[H_T\frac{d}{dr}\left(\frac{\phi}{\delta}\Lambda\right) - \left(\chi_\mu + \frac{\phi}{\delta}\chi_T + \frac{\phi}{\delta}\right)\Lambda\right] - \frac{2H_T}{r}\frac{\phi}{\delta}\Lambda\right\}$$

$$+ \frac{(\overline{\epsilon} + \overline{\epsilon}_{grav})}{\epsilon_m}\left\{H_T\frac{d}{dr}\left(\frac{\phi\Lambda}{\delta}\right) + \Lambda\left(f_\epsilon\epsilon_\mu + f_\epsilon\frac{\phi}{\delta}\chi_T - \chi_\mu - \frac{\phi}{\delta}\chi_T - \frac{\phi}{\delta}\right)\Lambda\right\}. \tag{7.2}$$

We have presented these intricate expressions to provide a sense of some of the dependencies. However, our intention is not to comprehensively detail the dependencies of these terms. For an in-depth examination of these dependencies and their derivations, we direct readers to Maeder 2009.

7.2   Basic Concepts in Asteroseismology

Asteroseismology uses the frequencies of the normal modes of pulsating stars as seismic waves. The pulsation modes are waves in the stellar interior, just like the waves that musical instruments resonate in. There is a large variety of normal modes that stars can pulsate in. The simplest are radial modes: the star periodically expands and shrinks, and its spherical symmetry is preserved. Pulsation in nonradial modes causes deviations from spherical symmetry: the star changes its shape. There are two major restoring forces for stellar oscillations that attempt to bring the star back in its equilibrium configuration:

pressure and buoyancy (gravity). Because of this pulsation modes are also classified into p pressure (p) modes and gravity (g) modes. The eigenfrequencies of stellar models, that are dependent on their physical parameters and interior structures, are matched to the observed ones. The propagation of pulsation modes in the stellar interior is governed by two frequencies. One of these is the Lamb frequency S_l, which is the inverse of the time needed to travel one horizontal wavelength at local sound speed. The other frequency describes at what rate a bubble of gas oscillates vertically around its equilibrium position at any given position inside a star; it is called the Brunt-Vaisälä frequency N. These two quantities are defined as:

$$S_l^2 = \frac{l(l+1)c_s^2}{r^2} \qquad N^2 = g\left(\frac{1}{p_0\gamma_1}\frac{dp_0}{dr} - \frac{1}{\rho_0}\frac{d\rho_0}{dr}\right) \qquad (7.3)$$

where l is the spherical degree, c_s is the local velocity of sound, r is the radius, g is the local gravitational acceleration, p_0 and ρ_0 are local pressure and density in the unperturbed state, respectively, and $\gamma_1 = (\frac{\rho dp}{pd\rho})_{ad}$ is the first adiabatic exponent. The Lamb and Brunt-Vaisälä frequencies have the following implications: an oscillation with a frequency higher than both experiences pressure as the main restoring force in the corresponding part of the star. On the other hand, a vibration with a frequency lower than both S_l and N is restored mostly by buoyancy. In other words, if we have a stellar oscillation with an angular frequency ω, it is a p-mode wherever $\omega > S_l, N$, and it is a g-mode wherever $\omega < S_l, N$. In stellar interior regions where ω lies between the Lamb and Brunt-Vaisälä frequencies, the amplitude of the wave decreases exponentially with distance from the p and g-mode propagation regions; such parts in the stellar interior are called evanescent regions. If the evanescent region between a the p and g-mode propagation regions is small, the mode is capable of "tunnelling" through it, and the p and g-mode couple giving rise to a *mixed mode*. In order to aid the visualization of this discussion we use propagation diagrams, where S_l and N are plotted against the radial coordinate or mass coordinate, an example of propagation diagram is shown in Fig. 7.1. Stellar pulsations induce surface displacements and temperature fluctuations, giving rise to observable variations. These variations cause alterations in luminosity, radial velocity, and spectral line profiles. Pulsating stars offer a dual avenue for examination, allowing for photometric and spectroscopic investigations through time-series observations.

Time-series data are subjected to frequency analysis, a process that involves the extraction of constituent signals from the observed data. Frequently, this entails harmonic analysis, wherein the time-series data is transformed into the frequency-amplitude domain. One common method for this transformation is the application of the Discrete Fourier Transformation (DFT), represented mathematically as:
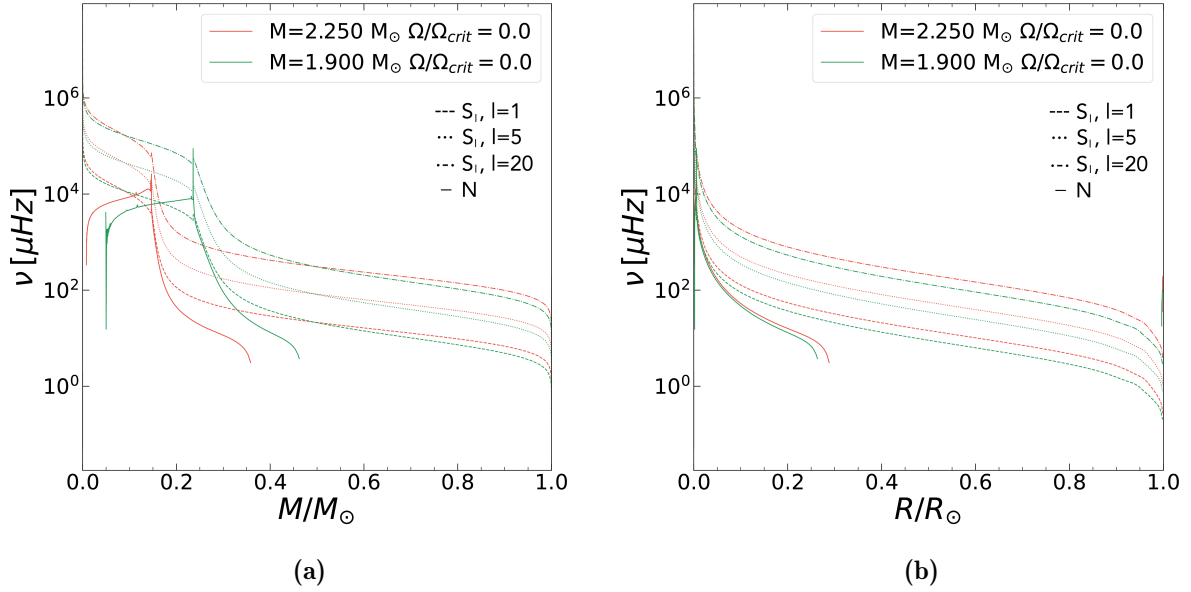
Figure 7.1: Propagation diagrams for two of our MESA models with masses of $M = 2.250$ M$_\odot$ and $M = 1.900$ M$_\odot$ and $\Omega_{ini}/\Omega_{crit} = 0.0$.

$$F_N(f) = \sum_{k=1}^{N} x(t_k) e^{i2\pi f t_k},$$

Here, $F_N(f)$ signifies the transformed data in the frequency domain, while $x(t_k)$ represents the time-series measurements at discrete time intervals t_k.

7.2.1 Driving Mechanisms

Stars maintain hydrostatic equilibrium, with gravitational forces on their constituent mass elements balanced by gas pressure. Consequently, the initiation of self-excited pulsations necessitates a driving mechanism capable of overcoming inherent damping, leading to periodic oscillations. Four primary driving mechanisms have been posited.

The ϵ mechanism (Rosseland and Randers 1938) postulates variations in stellar nuclear reaction rates: compression of a nuclear burning region elevates temperature and energy production. This triggers expansion, causing a drop in pressure and energy generation, thus reversing the motion and giving rise to oscillations.

Significantly more successful in elucidating stellar oscillations is the $\kappa - \gamma$ mechanism (Baker and Kippenhahn 1962 and references therein). It comes into play within layers where opacity (κ) increases and/or the third adiabatic exponent, $\Gamma_3 = (\frac{\partial \ln T}{\partial \ln \rho})_{ad} + 1$, decreases with rising temperature. These layers, typically linked to partial ionization of specific chemical elements in the stellar interior, temporally store flux from inner regions.

Energy accumulated during compression is subsequently released as the layer attempts to reach equilibrium through expansion. Consequently, the star can expand beyond its equilibrium radius, and when material recedes, energy is again stored, perpetuating the cycle and giving rise to periodic stellar oscillations. This phenomenon is also referred to as the "Eddington Valve" and accounts for variability in most known classes of pulsating stars.

Another mechanism, convective blocking (or convective driving), closely resembling the "valve" behavior, ensues when the base of a convection zone obstructs interior flux, temporarily releasing stored energy during the subsequent expansion phase.

Lastly, the pulsations of the Sun and solar-like stars, which are intrinsically stable and not considered self-excited, result from stochastic excitation caused by turbulence in their surface convection zones. Vigorous convection in outer surface layers generates acoustic noise across a broad frequency range, exciting solar-like oscillation modes. Due to the multitude of convective elements on the surface, excitation is inherently random, leading to temporal variability in oscillation amplitudes. The term "solar-like oscillations" encompasses oscillations excited stochastically by convection, presumably encompassing all stars with outer convection zones, from the cooler boundaries of the classical instability strip to red giants. Given the physical underpinnings of these driving mechanisms, the existence of distinct instability domains in the Hertzsprung-Russell diagram naturally follows.

7.3   Asteroseismic Masses

To deduce stellar masses, we employ key seismic parameters that characterize the spectra of solar-like oscillations. These parameters include the average large frequency separation ($\Delta\nu$) and the frequency corresponding to the maximum observed oscillation power (ν_{max}). The large frequency separation is expected to scale as the square root of the star's mean density, expressed as:

$$\Delta\nu \simeq \sqrt{\frac{M/M_\odot}{(R/R_\odot)^3}}\Delta\nu_\odot \qquad (7.4)$$

Here, $\Delta\nu_\odot$ is approximately 135 μHz. The frequency of maximum power, denoted as ν_{max}, exhibits an approximate proportionality to the acoustic cut-off frequency (Kjeldsen and Bedding 1995). Therefore:

$$\nu_{max} \simeq \frac{M/M_\odot}{(R/R_\odot)^2\sqrt{T_{eff}/T_{eff,\odot}}}\nu_{max,\odot} \qquad (7.5)$$

Here, $\nu_{max,\odot}$ is approximately 3100 μHz, and $T_{eff,\odot}$ is approximately 5777 K.

These scaling relations serve as widely accepted tools for estimating the masses and radii of red giants. The approach for deriving mass estimates from equations (7.4) and (7.5) varies depending on the available observational constraints. When data on distance or luminosity are lacking, which is common for field stars, equations (7.4) and (7.5) can be solved to obtain estimates for both mass (M) and radius (R). This method has been employed in studies such as Kallinger et al. 2010 and Mosser 2010, leading to the following expressions:

$$\frac{M}{M_\odot} \simeq \left(\frac{\nu_{max}}{\nu_{max,\odot}} \right)^3 \left(\frac{\Delta\nu}{\Delta\nu_\odot} \right)^{-4} \left(\frac{T_{eff}}{T_{eff,\odot}} \right)^{3/2} \tag{7.6}$$

$$\frac{R}{R_\odot} \simeq \left(\frac{\nu_{max}}{\nu_{max,\odot}} \right) \left(\frac{\Delta\nu}{\Delta\nu_\odot} \right)^{-2} \left(\frac{T_{eff}}{T_{eff,\odot}} \right)^{1/2} \tag{7.7}$$

In cases involving clusters, additional constraints from independent methods, such as isochrone fitting or eclipsing binaries, provide information about distance and luminosity. This additional information enables mass estimation through either equation (7.4) or equation (7.5) alone. The following equations (7.8), (7.9), and (7.10), which have no explicit dependence on T_{eff}, offer avenues for estimating mass:

$$\frac{M}{M_\odot} \simeq \left(\frac{\Delta\nu}{\Delta\nu_\odot} \right)^2 \left(\frac{L}{L_\odot} \right)^{3/2} \left(\frac{T_{eff}}{T_{eff,\odot}} \right)^{-6} \tag{7.8}$$

$$\frac{M}{M_\odot} \simeq \left(\frac{\nu_{max}}{\nu_{max,\odot}} \right)^3 \left(\frac{L}{L_\odot} \right) \left(\frac{T_{eff}}{T_{eff,\odot}} \right)^{-7/2} \tag{7.9}$$

$$\frac{M}{M_\odot} \simeq \left(\frac{\nu_{max}}{\nu_{max,\odot}} \right)^{12/5} \left(\frac{\Delta\nu}{\Delta\nu_\odot} \right)^{-14/5} \left(\frac{L}{L\odot} \right)^{3/10} \tag{7.10}$$

see Miglio et al. 2012 for further details on this topic.

Bibliography

Abdurro'uf, K. Accetta, C. Aerts, V. Silva Aguirre, R. Ahumada, N. Ajgaonkar, N. Filiz Ak, S. Alam, C. Allende Prieto, A. Almeida, F. Anders, S. F. Anderson, B. H. Andrews, B. Anguiano, E. Aquino-Ortíz, A. Aragón-Salamanca, M. Argudo-Fernández, M. Ata, M. Aubert, V. Avila-Reese, C. Badenes, R. H. Barbá, K. Barger, J. K. Barrera-Ballesteros, R. L. Beaton, T. C. Beers, F. Belfiore, C. F. Bender, M. Bernardi, M. A. Bershady, F. Beutler, C. M. Bidin, J. C. Bird, D. Bizyaev, G. A. Blanc, M. R. Blanton, N. F. Boardman, A. S. Bolton, M. Boquien, J. Borissova, J. Bovy, W. N. Brandt, J. Brown, J. R. Brownstein, M. Brusa, J. Buchner, K. Bundy, J. N. Burchett, M. Bureau, A. Burgasser, T. K. Cabang, S. Campbell, M. Cappellari, J. K. Carlberg, F. C. Wanderley, R. Carrera, J. Cash, Y.-P. Chen, W.-H. Chen, B. Cherinka, C. Chiappini, P. D. Choi, S. D. Chojnowski, H. Chung, N. Clerc, R. E. Cohen, J. M. Comerford, J. Comparat, L. da Costa, K. Covey, J. D. Crane, I. Cruz-Gonzalez, C. Culhane, K. Cunha, Y. S. Dai, G. Damke, J. Darling, J. Davidson, James W., R. Davies, K. Dawson, N. De Lee, A. M. Diamond-Stanic, M. Cano-Díaz, H. D. Sánchez, J. Donor, C. Duckworth, T. Dwelly, D. J. Eisenstein, Y. P. Elsworth, E. Emsellem, M. Eracleous, S. Escoffier, X. Fan, E. Farr, S. Feng, J. G. Fernández-Trincado, D. Feuillet, A. Filipp, S. P. Fillingham, P. M. Frinchaboy, S. Fromenteau, L. Galbany, R. A. García, D. A. García-Hernández, J. Ge, D. Geisler, J. Gelfand, T. Géron, B. J. Gibson, J. Goddy, D. Godoy-Rivera, K. Grabowski, P. J. Green, M. Greener, C. J. Grier, E. Griffith, H. Guo, J. Guy, M. Hadjara, P. Harding, S. Hasselquist, C. R. Hayes, F. Hearty, J. Hernández, L. Hill, D. W. Hogg, J. A. Holtzman, D. Horta, B.-C. Hsieh, C.-H. Hsu, Y.-H. Hsu, D. Huber, M. Huertas-Company, B. Hutchinson, H. S. Hwang, H. J. Ibarra-Medel, J. I. Chitham, G. S. Ilha, J. Imig, W. Jaekle, T. Jayasinghe, X. Ji, J. A. Johnson, A. Jones, H. Jönsson, I. Katkov, D. Khalatyan, Arman, K. Kinemuchi, S. Kisku, J. H. Knapen, J.-P. Kneib, J. A. Kollmeier, M. Kong, M. Kounkel, K. Kreckel, D. Krishnarao, I. Lacerna, R. R. Lane, R. Langgin, R. Lavender, D. R. Law, D. Lazarz, H. W. Leung, H.-H. Leung, H. M. Lewis, C. Li, R. Li, J. Lian, F.-H. Liang, L. Lin, Y.-T. Lin, S. Lin, C. Lintott, D. Long, P. Longa-Peña, C. López-Cobá, S. Lu, B. F. Lundgren, Y. Luo, J. T. Mackereth, A. de la Macorra, S. Mahadevan, S. R. Majewski, A. Manchado, T. Mandeville, C. Maraston, B. Margalef-Bentabol, T. Masseron, K. L. Mas-

ters, S. Mathur, R. M. McDermid, M. Mckay, A. Merloni, M. Merrifield, S. Meszaros, A. Miglio, F. Di Mille, D. Minniti, R. Minsley, A. Monachesi, J. Moon, B. Mosser, J. Mulchaey, D. Muna, R. R. Muñoz, A. D. Myers, N. Myers, S. Nadathur, P. Nair, K. Nandra, J. Neumann, J. A. Newman, D. L. Nidever, F. Nikakhtar, C. Nitschelm, J. E. O'Connell, L. Garma-Oehmichen, G. Luan Souza de Oliveira, R. Olney, D. Oravetz, M. Ortigoza-Urdaneta, Y. Osorio, J. Otter, Z. J. Pace, N. Padilla, K. Pan, H.-A. Pan, T. Parikh, J. Parker, S. Peirani, K. Peña Ramírez, S. Penny, W. J. Percival, I. Perez-Fournon, M. Pinsonneault, F. Poidevin, V. J. Poovelil, A. M. Price-Whelan, A. Bárbara de Andrade Queiroz, M. J. Raddick, A. Ray, S. B. Rembold, N. Riddle, R. A. Riffel, R. Riffel, H.-W. Rix, A. C. Robin, A. Rodríguez-Puebla, A. Roman-Lopes, C. Román-Zúñiga, B. Rose, A. J. Ross, G. Rossi, K. H. R. Rubin, M. Salvato, S. F. Sánchez, J. R. Sánchez-Gallego, R. Sanderson, F. A. Santana Rojas, E. Sarceno, R. Sarmiento, C. Sayres, E. Sazonova, A. L. Schaefer, R. Schiavon, D. J. Schlegel, D. P. Schneider, M. Schultheis, A. Schwope, A. Serenelli, J. Serna, Z. Shao, G. Shapiro, A. Sharma, Y. Shen, M. Shetrone, Y. Shu, J. D. Simon, M. F. Skrutskie, R. Smethurst, V. Smith, J. Sobeck, T. Spoo, D. Sprague, D. V. Stark, K. G. Stassun, M. Steinmetz, D. Stello, A. Stone-Martinez, T. Storchi-Bergmann, G. S. Stringfellow, A. Stutz, Y.-C. Su, M. Taghizadeh-Popp, M. S. Talbot, J. Tayar, E. Telles, J. Teske, A. Thakar, C. Theissen, A. Tkachenko, D. Thomas, R. Tojeiro, H. Hernandez Toledo, N. W. Troup, J. R. Trump, J. Trussler, J. Turner, S. Tuttle, E. Unda-Sanzana, J. A. Vázquez-Mata, M. Valentini, O. Valenzuela, J. Vargas-González, M. Vargas-Magaña, P. V. Alfaro, S. Villanova, F. Vincenzo, D. Wake, J. T. Warfield, J. D. Washington, B. A. Weaver, A.-M. Weijmans, D. H. Weinberg, A. Weiss, K. B. Westfall, V. Wild, M. C. Wilde, J. C. Wilson, R. F. Wilson, M. Wilson, J. Wolf, W. M. Wood-Vasey, R. Yan, O. Zamora, G. Zasowski, K. Zhang, C. Zhao, Z. Zheng, Z. Zheng, and K. Zhu. The Seventeenth Data Release of the Sloan Digital Sky Surveys: Complete Release of MaNGA, MaStar, and APOGEE-2 Data. *ApJS*, 259(2):35, Apr. 2022. doi: 10.3847/1538-4365/ac4414.

M. Asplund, N. Grevesse, and A. J. Sauval. The Solar Chemical Composition. In I. Barnes, Thomas G. and F. N. Bash, editors, *Cosmic Abundances as Records of Stellar Evolution and Nucleosynthesis*, volume 336 of *Astronomical Society of the Pacific Conference Series*, page 25, Sept. 2005.

M. Asplund, N. Grevesse, A. J. Sauval, and P. Scott. The Chemical Composition of the Sun. *ARA&A*, 47(1):481–522, Sept. 2009. doi: 10.1146/annurev.astro.46.060407. 145222.

N. Baker and R. Kippenhahn. The Pulsations of Models of δ Cephei Stars. With 17 Figures in the Text. *ZAp*, 54:114, Jan. 1962.

P. G. Beck, J. Montalban, T. Kallinger, J. De Ridder, C. Aerts, R. A. García, S. Hekker, M.-A. Dupret, B. Mosser, P. Eggenberger, D. Stello, Y. Elsworth, S. Frandsen, F. Carrier, M. Hillen, M. Gruberbauer, J. Christensen-Dalsgaard, A. Miglio, M. Valentini, T. R. Bedding, H. Kjeldsen, F. R. Girouard, J. R. Hall, and K. A. Ibrahim. Fast core rotation in red-giant stars as revealed by gravity-dominated mixed modes. *Nature*, 481 (7379):55–57, Jan. 2012. doi: 10.1038/nature10612.

J. Bétrisey, P. Eggenberger, G. Buldgen, O. Benomar, and M. Bazot. Testing angular momentum transport processes with asteroseismology of solar-type main-sequence stars. *A&A*, 673:L11, May 2023. doi: 10.1051/0004-6361/202245764.

E. Böhm-Vitense. *Introduction to Stellar Astrophysics*. 1989.

D. Bossini, A. Miglio, M. Salaris, M. Vrard, S. Cassisi, B. Mosser, J. Montalbán, L. Girardi, A. Noels, A. Bressan, A. Pietrinferni, and J. Tayar. Kepler red-clump stars in the field and in open clusters: constraints on core mixing. *MNRAS*, 469(4):4718–4725, Aug. 2017. doi: 10.1093/mnras/stx1135.

K. Brogaard, T. Arentoft, A. Miglio, G. Casali, J. S. Thomsen, M. Tailo, J. Montalbán, V. Grisoni, E. Willett, A. Stokholm, F. Grundahl, D. Stello, and E. L. Sandquist. An asteroseismic age estimate of the open cluster NGC 6866 using Kepler and Gaia. *arXiv e-prints*, art. arXiv:2308.12731, Aug. 2023. doi: 10.48550/arXiv.2308.12731.

B. Chaboyer and J. P. Zahn. Effect of horizontal turbulent diffusion on transport by meridional circulation. *A&A*, 253:173–177, Jan. 1992.

J. Choi, A. Dotter, C. Conroy, M. Cantiello, B. Paxton, and B. D. Johnson. Mesa Isochrones and Stellar Tracks (MIST). I. Solar-scaled Models. *ApJ*, 823(2):102, June 2016. doi: 10.3847/0004-637X/823/2/102.

A. Claret and G. Torres. The Dependence of Convective Core Overshooting on Stellar Mass: A Semi-empirical Determination Using the Diffusive Approach with Two Different Element Mixtures. *ApJ*, 849(1):18, Nov. 2017. doi: 10.3847/1538-4357/aa8770.

J. P. Cox and R. T. Giuli. *Principles of stellar structure*. 1968.

K. Cunha, I. Hubeny, and T. Lanz. Neon abundances in b stars of the orion association: Solving the solar model problem? *The Astrophysical Journal*, 647(2):L143, aug 2006. doi: 10.1086/507301. URL https://dx.doi.org/10.1086/507301.

R. H. Cyburt, A. M. Amthor, R. Ferguson, Z. Meisel, K. Smith, S. Warren, A. Heger, R. D. Hoffman, T. Rauscher, A. Sakharuk, H. Schatz, F. K. Thielemann, and M. Wi-

escher. The JINA REACLIB Database: Its Recent Updates and Impact on Type-I X-ray Bursts. *ApJS*, 189:240–252, jul 2010. doi: 10.1088/0067-0049/189/1/240.

S. Deheuvels, J. Ballot, P. G. Beck, B. Mosser, R. Østensen, R. A. García, and M. J. Goupil. Seismic evidence for a weak radial differential rotation in intermediate-mass core helium burning stars. *A&A*, 580:A96, Aug. 2015. doi: 10.1051/0004-6361/201526449.

S. Deheuvels, J. Ballot, P. Eggenberger, F. Spada, A. Noll, and J. W. den Hartogh. Seismic evidence for near solid-body rotation in two Kepler subgiants and implications for angular momentum transport. *A&A*, 641:A117, Sept. 2020. doi: 10.1051/0004-6361/202038578.

F. Dresbach, D. Massari, B. Lanzoni, F. R. Ferraro, E. Dalessandro, M. Libralato, and S. Raso. Extended Main-Sequence Turnoff and Red Clump in intermediate-age star clusters: A study of NGC 419. *arXiv e-prints*, art. arXiv:2310.01499, Oct. 2023. doi: 10.48550/arXiv.2310.01499.

P. Eggenberger. Magnetic fields and transport processe. *Bulletin de la Societe Royale des Sciences de Liege*, 88:15–26, Dec. 2019.

P. Eggenberger, G. Meynet, A. Maeder, R. Hirschi, C. Charbonnel, S. Talon, and S. Ekström. The Geneva stellar evolution code. *Ap&SS*, 316(1-4):43–54, Aug. 2008. doi: 10.1007/s10509-007-9511-y.

P. Eggenberger, A. Miglio, J. Montalban, O. Moreira, A. Noels, G. Meynet, and A. Maeder. Effects of rotation on the evolution and asteroseismic properties of red giants. *A&A*, 509:A72, Jan. 2010. doi: 10.1051/0004-6361/200912897.

P. Eggenberger, J. Montalbán, and A. Miglio. Angular momentum transport in stellar interiors constrained by rotational splittings of mixed modes in red giants. *A&A*, 544: L4, Aug. 2012. doi: 10.1051/0004-6361/201219729.

P. Eggenberger, J. W. den Hartogh, G. Buldgen, G. Meynet, S. J. A. J. Salmon, and S. Deheuvels. Asteroseismology of evolved stars to constrain the internal transport of angular momentum. II. Test of a revised prescription for transport by the Tayler instability. *A&A*, 631:L6, Nov. 2019. doi: 10.1051/0004-6361/201936348.

Y. Elsworth, N. Themeßl, S. Hekker, and W. Chaplin. A Layered Approach to Robust Determination of Asteroseismic Parameters. *Research Notes of the American Astronomical Society*, 4(10):177, Oct. 2020. doi: 10.3847/2515-5172/abbf5a.

A. S. Endal and S. Sofia. The evolution of rotating stars. I. Method and exploratory calculations for a 7 M sun star. *ApJ*, 210:184–198, Nov. 1976. doi: 10.1086/154817.

B. Freytag, H. G. Ludwig, and M. Steffen. Hydrodynamical models of stellar convection. The role of overshoot in DA white dwarfs, A-type stars, and the Sun. *A&A*, 313: 497–516, Sept. 1996.

Gaia Collaboration, A. Vallenari, A. G. A. Brown, T. Prusti, J. H. J. de Bruijne, F. Arenou, C. Babusiaux, M. Biermann, O. L. Creevey, C. Ducourant, D. W. Evans, L. Eyer, R. Guerra, A. Hutton, C. Jordi, S. A. Klioner, U. L. Lammers, L. Lindegren, X. Luri, F. Mignard, C. Panem, D. Pourbaix, S. Randich, P. Sartoretti, C. Soubiran, P. Tanga, N. A. Walton, C. A. L. Bailer-Jones, U. Bastian, R. Drimmel, F. Jansen, D. Katz, M. G. Lattanzi, F. van Leeuwen, J. Bakker, C. Cacciari, J. Castañeda, F. De Angeli, C. Fabricius, M. Fouesneau, Y. Frémat, L. Galluccio, A. Guerrier, U. Heiter, E. Masana, R. Messineo, N. Mowlavi, C. Nicolas, K. Nienartowicz, F. Pailler, P. Panuzzo, F. Riclet, W. Roux, G. M. Seabroke, R. Sordo, F. Thévenin, G. Gracia-Abril, J. Portell, D. Teyssier, M. Altmann, R. Andrae, M. Audard, I. Bellas-Velidis, K. Benson, J. Berthier, R. Blomme, P. W. Burgess, D. Busonero, G. Busso, H. Cánovas, B. Carry, A. Cellino, N. Cheek, G. Clementini, Y. Damerdji, M. Davidson, P. de Teodoro, M. Nuñez Campos, L. Delchambre, A. Dell'Oro, P. Esquej, J. Fernández-Hernández, E. Fraile, D. Garabato, P. García-Lario, E. Gosset, R. Haigron, J. L. Halbwachs, N. C. Hambly, D. L. Harrison, J. Hernández, D. Hestroffer, S. T. Hodgkin, B. Holl, K. Janßen, G. Jevardat de Fombelle, S. Jordan, A. Krone-Martins, A. C. Lanzafame, W. Löffler, O. Marchal, P. M. Marrese, A. Moitinho, K. Muinonen, P. Osborne, E. Pancino, T. Pauwels, A. Recio-Blanco, C. Reylé, M. Riello, L. Rimoldini, T. Roegiers, J. Rybizki, L. M. Sarro, C. Siopis, M. Smith, A. Sozzetti, E. Utrilla, M. van Leeuwen, U. Abbas, P. Ábrahám, A. Abreu Aramburu, C. Aerts, J. J. Aguado, M. Ajaj, F. Aldea-Montero, G. Altavilla, M. A. Álvarez, J. Alves, F. Anders, R. I. Anderson, E. Anglada Varela, T. Antoja, D. Baines, S. G. Baker, L. Balaguer-Núñez, E. Balbinot, Z. Balog, C. Barache, D. Barbato, M. Barros, M. A. Barstow, S. Bartolomé, J. L. Bassilana, N. Bauchet, U. Becciani, M. Bellazzini, A. Berihuete, M. Bernet, S. Bertone, L. Bianchi, A. Binnenfeld, S. Blanco-Cuaresma, A. Blazere, T. Boch, A. Bombrun, D. Bossini, S. Bouquillon, A. Bragaglia, L. Bramante, E. Breedt, A. Bressan, N. Brouillet, E. Brugaletta, B. Bucciarelli, A. Burlacu, A. G. Butkevich, R. Buzzi, E. Caffau, R. Cancelliere, T. Cantat-Gaudin, R. Carballo, T. Carlucci, M. I. Carnerero, J. M. Carrasco, L. Casamiquela, M. Castellani, A. Castro-Ginard, L. Chaoul, P. Charlot, L. Chemin, V. Chiaramida, A. Chiavassa, N. Chornay, G. Comoretto, G. Contursi, W. J. Cooper, T. Cornez, S. Cowell, F. Crifo, M. Cropper, M. Crosta, C. Crowley, C. Dafonte, A. Dapergolas, M. David, P. David, P. de Laverny, F. De Luise, R. De March, J. De Ridder, R. de Souza, A. de Torres, E. F. del Peloso, E. del Pozo, M. Delbo, A. Delgado, J. B. Delisle, C. Demouchy, T. E. Dharmawardena, P. Di Matteo, S. Diakite, C. Diener, E. Distefano, C. Dolding, B. Edvardsson, H. Enke, C. Fabre, M. Fabrizio, S. Faigler,

G. Fedorets, P. Fernique, A. Fienga, F. Figueras, Y. Fournier, C. Fouron, F. Fragk-oudi, M. Gai, A. Garcia-Gutierrez, M. Garcia-Reinaldos, M. García-Torres, A. Garo-falo, A. Gavel, P. Gavras, E. Gerlach, R. Geyer, P. Giacobbe, G. Gilmore, S. Girona, G. Giuffrida, R. Gomel, A. Gomez, J. González-Núñez, I. González-Santamaría, J. J. González-Vidal, M. Granvik, P. Guillout, J. Guiraud, R. Gutiérrez-Sánchez, L. P. Guy, D. Hatzidimitriou, M. Hauser, M. Haywood, A. Helmer, A. Helmi, M. H. Sarmiento, S. L. Hidalgo, T. Hilger, N. Hładczuk, D. Hobbs, G. Holland, H. E. Huckle, K. Jardine, G. Jasniewicz, A. Jean-Antoine Piccolo, Ó. Jiménez-Arranz, A. Jorissen, J. Juaristi Campillo, F. Julbe, L. Karbevska, P. Kervella, S. Khanna, M. Kontizas, G. Kordopatis, A. J. Korn, Á. Kóspál, Z. Kostrzewa-Rutkowska, K. Kruszyńska, M. Kun, P. Laizeau, S. Lambert, A. F. Lanza, Y. Lasne, J. F. Le Campion, Y. Lebreton, T. Lebzelter, S. Leccia, N. Leclerc, I. Lecoeur-Taibi, S. Liao, E. L. Licata, H. E. P. Lindstrøm, T. A. Lister, E. Livanou, A. Lobel, A. Lorca, C. Loup, P. Madrero Pardo, A. Magdaleno Romeo, S. Managau, R. G. Mann, M. Manteiga, J. M. Marchant, M. Marconi, J. Mar-cos, M. M. S. Marcos Santos, D. Marín Pina, S. Marinoni, F. Marocco, D. J. Marshall, L. Martin Polo, J. M. Martín-Fleitas, G. Marton, N. Mary, A. Masip, D. Massari, A. Mastrobuono-Battisti, T. Mazeh, P. J. McMillan, S. Messina, D. Michalik, N. R. Millar, A. Mints, D. Molina, R. Molinaro, L. Molnár, G. Monari, M. Monguió, P. Mon-tegriffo, A. Montero, R. Mor, A. Mora, R. Morbidelli, T. Morel, D. Morris, T. Muraveva, C. P. Murphy, I. Musella, Z. Nagy, L. Noval, F. Ocaña, A. Ogden, C. Ordenovic, J. O. Osinde, C. Pagani, I. Pagano, L. Palaversa, P. A. Palicio, L. Pallas-Quintela, A. Panahi, S. Payne-Wardenaar, X. Peñalosa Esteller, A. Penttilä, B. Pichon, A. M. Piersimoni, F. X. Pineau, E. Plachy, G. Plum, E. Poggio, A. Prša, L. Pulone, E. Racero, S. Ragaini, M. Rainer, C. M. Raiteri, N. Rambaux, P. Ramos, M. Ramos-Lerate, P. Re Fiorentin, S. Regibo, P. J. Richards, C. Rios Diaz, V. Ripepi, A. Riva, H. W. Rix, G. Rixon, N. Robichon, A. C. Robin, C. Robin, M. Roelens, H. R. O. Rogues, L. Rohrbasser, M. Romero-Gómez, N. Rowell, F. Royer, D. Ruz Mieres, K. A. Rybicki, G. Sadowski, A. Sáez Núñez, A. Sagristà Sellés, J. Sahlmann, E. Salguero, N. Samaras, V. Sanchez Gimenez, N. Sanna, R. Santoveña, M. Sarasso, M. Schultheis, E. Sciacca, M. Segol, J. C. Segovia, D. Ségransan, D. Semeux, S. Shahaf, H. I. Siddiqui, A. Siebert, L. Sil-tala, A. Silvelo, E. Slezak, I. Slezak, R. L. Smart, O. N. Snaith, E. Solano, F. Solitro, D. Souami, J. Souchay, A. Spagna, L. Spina, F. Spoto, I. A. Steele, H. Steidelmüller, C. A. Stephenson, M. Süveges, J. Surdej, L. Szabados, E. Szegedi-Elek, F. Taris, M. B. Taylor, R. Teixeira, L. Tolomei, N. Tonello, F. Torra, J. Torra, G. Torralba Elipe, M. Trabucchi, A. T. Tsounis, C. Turon, A. Ulla, N. Unger, M. V. Vaillant, E. van Dillen, W. van Reeven, O. Vanel, A. Vecchiato, Y. Viala, D. Vicente, S. Voutsinas, M. Weiler, T. Wevers, Ł. Wyrzykowski, A. Yoldas, P. Yvard, H. Zhao, J. Zorec, S. Zucker, and T. Zwitter. Gaia Data Release 3. Summary of the content and survey properties. *A&A*,

674:A1, June 2023. doi: 10.1051/0004-6361/202243940.

C. Georgy, S. Ekström, A. Granada, G. Meynet, N. Mowlavi, P. Eggenberger, and A. Maeder. Populations of rotating stars - i. models from 1.7 to 15 z = 0.014, 0.006, and 0.002 with rit between 0 and 1. *A&A*, 553:A24, 2013. doi: 10.1051/0004-6361/201220558. URL https://doi.org/10.1051/0004-6361/201220558.

C. Georgy, A. Granada, S. Ekström, G. Meynet, R. I. Anderson, A. Wyttenbach, P. Eggenberger, and A. Maeder. Populations of rotating stars. III. SYCLIST, the new Geneva population synthesis code. *A&A*, 566:A21, June 2014a. doi: 10.1051/0004-6361/201423881.

C. Georgy, A. Granada, S. Ekström, G. Meynet, R. I. Anderson, A. Wyttenbach, P. Eggenberger, and A. Maeder. Populations of rotating stars. III. SYCLIST, the new Geneva population synthesis code. *A&A*, 566:A21, June 2014b. doi: 10.1051/0004-6361/201423881.

L. Girardi. A secondary clump of red giant stars: why and where. *MNRAS*, 308(3):818–832, Sept. 1999. doi: 10.1046/j.1365-8711.1999.02746.x.

L. Girardi, M. A. T. Groenewegen, A. Weiss, and M. Salaris. Fine structure of the red giant clump from HIPPARCOS data, and distance determinations based on its mean magnitude. *MNRAS*, 301(1):149–160, Nov. 1998. doi: 10.1046/j.1365-8711.1998.02011.x.

L. Girardi, J. C. Mermilliod, and G. Carraro. On the peculiar red clump morphology in the open clusters NGC 752 and NGC 7789. *A&A*, 354:892–898, Feb. 2000. doi: 10.48550/arXiv.astro-ph/0001068.

L. Girardi, S. Rubele, and L. Kerber. Discovery of two distinct red clumps in NGC 419: a rare snapshot of a cluster at the onset of degeneracy. *MNRAS*, 394(1):L74–L78, Mar. 2009. doi: 10.1111/j.1745-3933.2008.00614.x.

L. Girardi, S. Rubele, and L. Kerber. Star clusters with dual red clumps. In R. de Grijs and J. R. D. Lépine, editors, *Star Clusters: Basic Galactic Building Blocks Throughout Time and Space*, volume 266, pages 320–325, Jan. 2010. doi: 10.1017/S1743921309991207.

L. Gratton. Circolazione interna e instabilità nelle binarie strette. *Mem. Soc. Astron. Italiana*, 17:5, Jan. 1945.

A. Heger, N. Langer, and S. E. Woosley. Presupernova Evolution of Rotating Massive Stars. I. Numerical Method and Evolution of the Internal Stellar Structure. *ApJ*, 528(1):368–396, Jan. 2000. doi: 10.1086/308158.

F. Herwig. The evolution of AGB stars with convective overshoot. *A&A*, 360:952–968, Aug. 2000. doi: 10.48550/arXiv.astro-ph/0007139.

F. Herwig, T. Bloecker, D. Schoenberner, and M. El Eid. Stellar evolution of low and intermediate-mass stars. IV. Hydrodynamically-based overshoot and nucleosynthesis in AGB stars. *A&A*, 324:L81–L84, Aug. 1997. doi: 10.48550/arXiv.astro-ph/9706122.

T. Kallinger, W. W. Weiss, C. Barban, F. Baudin, C. Cameron, F. Carrier, J. De Ridder, M. J. Goupil, M. Gruberbauer, A. Hatzes, S. Hekker, R. Samadi, and M. Deleuil. Oscillating red giants in the CoRoT exofield: asteroseismic mass and radius determination. *A&A*, 509:A77, Jan. 2010. doi: 10.1051/0004-6361/200811437.

S. Kamann, N. Bastian, T. O. Husser, S. Martocchia, C. Usher, M. den Brok, S. Dreizler, A. Kelz, D. Krajnović, J. Richard, M. Steinmetz, and P. M. Weilbacher. Cluster kinematics and stellar rotation in NGC 419 with MUSE and adaptive optics. *MNRAS*, 480 (2):1689–1695, Oct. 2018. doi: 10.1093/mnras/sty1958.

S. Khan, O. J. Hall, A. Miglio, G. R. Davies, B. Mosser, L. Girardi, and J. Montalbán. The Red-giant Branch Bump Revisited: Constraints on Envelope Overshooting in a Wide Range of Masses and Metallicities. *ApJ*, 859(2):156, June 2018. doi: 10.3847/1538-4357/aabf90.

R. Kippenhahn and H. C. Thomas. A Simple Method for the Solution of the Stellar Structure Equations Including Rotation and Tidal Forces. In A. Slettebak, editor, *IAU Colloq. 4: Stellar Rotation*, page 20, Jan. 1970.

H. Kjeldsen and T. R. Bedding. Amplitudes of stellar oscillations: the implications for asteroseismology. *A&A*, 293:87–106, Jan. 1995. doi: 10.48550/arXiv.astro-ph/9403015.

K. S. Krishna Swamy. Profiles of Strong Lines in K-Dwarfs. *ApJ*, 145:174, July 1966. doi: 10.1086/148752.

A. Maeder. Stellar evolution with rotation. II. A new approach for shear mixing. *A&A*, 321:134–144, May 1997.

A. Maeder. *Physics, Formation and Evolution of Rotating Stars*. 2009. doi: 10.1007/978-3-540-76949-1.

A. Maeder and J.-P. Zahn. Stellar evolution with rotation. III. Meridional circulation with MU -gradients and non-stationarity. *A&A*, 334:1000–1006, June 1998.

S. Mathis and J. P. Zahn. Transport and mixing in the radiation zones of rotating stars. I. Hydrodynamical processes. *A&A*, 425:229–242, Oct. 2004. doi: 10.1051/0004-6361:20040278.

G. Meynet and A. Maeder. Stellar evolution with rotation. I. The computational method and the inhibiting effect of the μ-gradient. *A&A*, 321:465–476, May 1997.

G. Meynet and A. Maeder. Stellar evolution with rotation. VIII. Models at Z = 10^{-5} and CNO yields for early galactic evolution. *A&A*, 390:561–583, Aug. 2002. doi: 10.1051/0004-6361:20020755.

A. Miglio, J. Montalbán, A. Noels, and P. Eggenberger. Probing the properties of convective cores through g modes: high-order g modes in SPB and γ Doradus stars. *MNRAS*, 386(3):1487–1502, May 2008. doi: 10.1111/j.1365-2966.2008.13112.x.

A. Miglio, K. Brogaard, D. Stello, W. J. Chaplin, F. D'Antona, J. Montalbán, S. Basu, A. Bressan, F. Grundahl, M. Pinsonneault, A. M. Serenelli, Y. Elsworth, S. Hekker, T. Kallinger, B. Mosser, P. Ventura, A. Bonanno, A. Noels, V. Silva Aguirre, R. Szabo, J. Li, S. McCauliff, C. K. Middour, and H. Kjeldsen. Asteroseismology of old open clusters with Kepler: direct estimate of the integrated red giant branch mass-loss in NGC 6791 and 6819. *Monthly Notices of the Royal Astronomical Society*, 419(3):2077–2088, 01 2012. ISSN 0035-8711. doi: 10.1111/j.1365-2966.2011.19859.x. URL `https://doi.org/10.1111/j.1365-2966.2011.19859.x`.

J. Montalbán, J. T. Mackereth, A. Miglio, F. Vincenzo, C. Chiappini, G. Buldgen, B. Mosser, A. Noels, R. Scuflaire, M. Vrard, E. Willett, G. R. Davies, O. J. Hall, M. B. Nielsen, S. Khan, B. M. Rendle, W. E. van Rossem, J. W. Ferguson, and W. J. Chaplin. Chronologically dating the early assembly of the Milky Way. *Nature Astronomy*, 5:640–647, Jan. 2021. doi: 10.1038/s41550-021-01347-7.

B. Mosser. An alternative to mode fitting. *Astronomische Nachrichten*, 331:944, Dec. 2010. doi: 10.1002/asna.201011432.

B. Mosser and T. Appourchaux. On detecting the large separation in the autocorrelation of stellar oscillation times series. *A&A*, 508(2):877–887, Dec. 2009. doi: 10.1051/0004-6361/200912944.

F. D. Moyano, P. Eggenberger, S. J. A. J. Salmon, J. S. G. Mombarg, and S. Ekström. Angular momentum transport by magnetic fields in main sequence stars with Gamma Doradus pulsators. *arXiv e-prints*, art. arXiv:2304.00674, Apr. 2023. doi: 10.48550/arXiv.2304.00674.

E. J. Öpik. Rotational currents. *MNRAS*, 111:278, Jan. 1951. doi: 10.1093/mnras/111.3.278.

B. Paxton, L. Bildsten, A. Dotter, F. Herwig, P. Lesaffre, and F. Timmes. Modules for Experiments in Stellar Astrophysics (MESA). *ApJS*, 192(1):3, Jan. 2011. doi: 10.1088/0067-0049/192/1/3.

B. Paxton, M. Cantiello, P. Arras, L. Bildsten, E. F. Brown, A. Dotter, C. Mankovich, M. H. Montgomery, D. Stello, F. X. Timmes, and R. Townsend. Modules for Experiments in Stellar Astrophysics (MESA): Planets, Oscillations, Rotation, and Massive Stars. *ApJS*, 208(1):4, Sept. 2013. doi: 10.1088/0067-0049/208/1/4.

B. Paxton, P. Marchant, J. Schwab, E. B. Bauer, L. Bildsten, M. Cantiello, L. Dessart, R. Farmer, H. Hu, N. Langer, R. H. D. Townsend, D. M. Townsley, and F. X. Timmes. Modules for Experiments in Stellar Astrophysics (MESA): Binaries, Pulsations, and Explosions. *ApJS*, 220(1):15, Sept. 2015. doi: 10.1088/0067-0049/220/1/15.

B. Paxton, J. Schwab, E. B. Bauer, L. Bildsten, S. Blinnikov, P. Duffell, R. Farmer, J. A. Goldberg, P. Marchant, E. Sorokina, A. Thoul, R. H. D. Townsend, and F. X. Timmes. Modules for Experiments in Stellar Astrophysics (MESA): Convective Boundaries, Element Diffusion, and Massive Star Explosions. *ApJS*, 234(2):34, Feb. 2018. doi: 10.3847/1538-4365/aaa5a8.

B. Paxton, R. Smolec, J. Schwab, A. Gautschy, L. Bildsten, M. Cantiello, A. Dotter, R. Farmer, J. A. Goldberg, A. S. Jermyn, S. M. Kanbur, P. Marchant, A. Thoul, R. H. D. Townsend, W. M. Wolf, M. Zhang, and F. X. Timmes. Modules for Experiments in Stellar Astrophysics (MESA): Pulsating Variable Stars, Rotation, Convective Boundaries, and Energy Conservation. *ApJS*, 243(1):10, July 2019. doi: 10.3847/1538-4365/ab2241.

M. H. Pinsonneault, S. D. Kawaler, S. Sofia, and P. Demarque. Evolutionary Models of the Rotating Sun. *ApJ*, 338:424, Mar. 1989. doi: 10.1086/167210.

S. Rosseland and G. Randers. On the Stability of Pulsating Stars. *Astrophysica Norvegica*, 3:71, Mar. 1938.

F. Royer, J. Zorec, and A. E. Gómez. Rotational velocities of A-type stars. III. Velocity distributions. *A&A*, 463(2):671–682, Feb. 2007. doi: 10.1051/0004-6361:20065224.

M. Salaris and S. Cassisi. *Evolution of Stars and Stellar Populations*. 2006.

E. L. Sandquist, J. Jessen-Hansen, M. D. Shetrone, K. Brogaard, S. Meibom, M. Leitner, D. Stello, H. Bruntt, V. Antoci, J. A. Orosz, F. Grundahl, and S. Frandsen. The Age and Distance of the Kepler Open Cluster NGC 6811 from an Eclipsing Binary, Turnoff Star Pulsation, and Giant Asteroseismology. *ApJ*, 831(1):11, Nov. 2016. doi: 10.3847/0004-637X/831/1/11.

E. L. Sandquist, D. Stello, T. Arentoft, K. Brogaard, F. Grundahl, A. Vanderburg, A. Hedlund, R. DeWitt, T. R. Ackerman, M. Aguilar, A. J. Buckner, C. Juarez, A. J. Ortiz, D. Richarte, D. I. Rivera, and L. Schlapfer. Variability in the Massive Open Cluster NGC 1817 from K2: A Rich Population of Asteroseismic Red Clump, Eclipsing Binary, and Main-sequence Pulsating Stars. *AJ*, 159(3):96, Mar. 2020. doi: 10.3847/1538-3881/ab68df.

M. Schönberg and S. Chandrasekhar. On the Evolution of the Main-Sequence Stars. *ApJ*, 96:161, Sept. 1942. doi: 10.1086/144444.

E. A. Spiegel and J. P. Zahn. The solar tachocline. *A&A*, 265:106–114, Nov. 1992.

M. P. L. Suijs, N. Langer, A. J. Poelarends, S. C. Yoon, A. Heger, and F. Herwig. White dwarf spins from low-mass stellar evolution models. *A&A*, 481(3):L87–L90, Apr. 2008. doi: 10.1051/0004-6361:200809411.

R. H. D. Townsend and S. A. Teitler. GYRE: an open-source stellar oscillation code based on a new Magnus Multiple Shooting scheme. *MNRAS*, 435(4):3406–3418, Nov. 2013. doi: 10.1093/mnras/stt1533.

F. Vincenzo, D. H. Weinberg, J. Montalbán, A. Miglio, S. Khan, E. J. Griffith, S. Hasselquist, J. W. Johnson, J. A. Johnson, C. Nitschelm, and M. H. Pinsonneault. CNO dredge-up in a sample of APOGEE/Kepler red giants: Tests of stellar models and Galactic evolutionary trends of N/O and C/N. *arXiv e-prints*, art. arXiv:2106.03912, June 2021. doi: 10.48550/arXiv.2106.03912.

H. von Zeipel. The radiative equilibrium of a rotating system of gaseous masses. *MNRAS*, 84:665–683, June 1924. doi: 10.1093/mnras/84.9.665.

X. Wu, C. Li, R. de Grijs, and L. Deng. First Observational Signature of Rotational Deceleration in a Massive, Intermediate-age Star Cluster in the Magellanic Clouds. *ApJ*, 826(1):L14, July 2016. doi: 10.3847/2041-8205/826/1/L14.

J. P. Zahn. Circulation and turbulence in rotating stars. *A&A*, 265:115–132, Nov. 1992.